



## **POLITECNICO DI BARI**

### **Department of Electrical and Information Engineering**

Bachelor Degree Program in Electronic and Telecommunications Engineering

---

B.Sc. Dissertation on  
Microwaves and Antennas

## **ANALYSIS OF MULTIPACTION EFFECT IN S-BAND COMPONENTS FOR PARTICLE ACCELERATORS**

Supervisors:

Prof. Ing. Francesco Prudenzano  
Ing. Giovanni Rutigliani

Assistant Supervisors:

Dr. Ing. Antonella Maria Loconsole  
Ing. Francesco Anelli

Graduating Student:  
Francesco Caterina

---

Academic Year 2021/2022



**LIBERATORIA ALLA CONSULTAZIONE DELLA TESI DI LAUREA DI CUI ALL'ART.4  
DEL REGOLAMENTO DI ATENEO PER LA CONSULTAZIONE DELLE TESI DI  
LAUREA (D.R. n. 479 del 14/11/2016).**

Il sottoscritto Caterina Francesco, matricola 564974, Corso di Laurea Ingegneria Elettronica e delle Telecomunicazioni, autore della presente tesi di Laurea dal titolo "ANALYSIS OF MULTIPACTION EFFECT IN S-BAND COMPONENTS FOR PARTICLE ACCELERATORS"

Parola chiave: Multipaction; Particle Accelerators; RF Power Distribution Systems; Riblet short slot coupler; Directional Couplers; Particle-In-Cell.

Abstract: This work has been developed within a cooperation between the Microwave and Optical Engineering MOE group – Department of Electrical and Information Engineering of Politecnico di Bari and the enterprise LinearBeam (Ruvo). It is an in-depth analysis of the multipaction effect, in the context of waveguide-based components for particle accelerators. This effect consists in an electronic avalanche inside a RF component which normally operates under vacuum conditions. If present, multipaction can not only physically damage the device by giving birth to arcing and corona discharges, but can also be responsible of other phenomena which should be avoided in RF systems. After a brief overview of particle accelerator systems, a specific focus on the structure and components used in their RF power distribution system is provided. Then the theoretical framework extensively employed in literature for the understanding of the multipaction effect is briefly illustrated. In addition, techniques used for its evaluation by means of Particle-In-Cell simulations have been employed in this work for the detection of multipaction thresholds. In particular, Particle-In-Cell simulations have been performed to investigate a waveguide-based directional coupler, namely a Riblet short slot coupler, at our disposal for the measurements. The results obtained with PIC simulations have shown the limits of operation of this device, which should not be exceeded in order to avoid the aforementioned effects if one wants to keep the device under its safety operational limits.

Autorizza       Non autorizza

la consultazione della presente tesi, fatto divieto a chiunque di riprodurre in tutto o in parte quanto in essa contenuto.

Bari, 01/04/2023

Firma

*Francesco Coteina*

*To Giuseppe and Tonia, for their support throughout this journey*



# Abstract

---

This work has been developed within a cooperation between the Microwave and Optical Engineering MOE group – Department of Electrical and Information Engineering of Politecnico di Bari and the enterprise LinearBeam (Ruvo). It is an in-depth analysis of the multipaction effect, in the context of waveguide-based components for particle accelerators. This effect consists in an electronic avalanche inside a RF component which normally operates under vacuum conditions. If present, multipaction can not only physically damage the device by giving birth to arcing and corona discharges, but can also be responsible of other phenomena which should be avoided in RF systems.

After a brief overview of particle accelerator systems, a specific focus on the structure and components used in their RF power distribution system is provided. Then the theoretical framework extensively employed in literature for the understanding of the multipaction effect is briefly illustrated. In addition, techniques used for its evaluation by means of Particle-In-Cell simulations have been employed in this work for the detection of multipaction thresholds. In particular, Particle-In-Cell simulations have been performed to investigate a waveguide-based directional coupler, namely a Riblet short slot coupler, at our disposal for the measurements. The results obtained with PIC simulations have shown the limits of operation of this device, which should not be exceeded in order to avoid the aforementioned effects if one wants to keep the device under its safety operational limits.

# Table of Contents

---

<b>Introduction .....</b>	<b>1</b>
<b>1 RF Power Distribution Systems for Linear Accelerators .....</b>	<b>3</b>
1.1 General particle accelerator classification .....	3
1.2 General structure and principle of operations of a linear particle accelerator.....	5
1.3 Waveguides .....	10
1.4 Phase shifters .....	18
1.5 Circulators, isolators and high-power loads .....	20
1.6 Ceramic windows .....	23
1.7 Directional couplers .....	25
1.7.1 The Riblet short slot coupler.....	28
1.8 Example of a RF power distribution system in a generic S-band LINAC.....	34
<b>2 Physical modelling of multipaction effect .....</b>	<b>36</b>
2.1 Multipaction effect .....	36
2.1.1 Qualitative description.....	38
2.1.2 Multipaction simulation in software. Secondary emission: Vaughan's and Furman-Pivi's models....	42
2.2 Multipaction analysis in parallel plates waveguides .....	52
2.2.1 Multipaction analysis of a parallel plates waveguide using the ECSS multipactor tool.....	56
2.2.2 Parallel plates waveguide multipaction analysis by using CST Particle Studio.....	65

<b>3 Riblet short-slot coupler analysis.....</b>	<b>74</b>
3.1 VNA calibration and S-parameters measurements .....	75
3.2 Modelling and simulation of the Riblet short slot coupler in CST MWS.....	85
3.3 Multipaction analysis in CST Particle Studio of the Riblet short slot coupler modelled in CST MWS .....	98
 <b>Conclusions .....</b>	 <b>107</b>
 <b>Bibliography .....</b>	 <b>109</b>

# Introduction

---

This work has been developed within a cooperation between the Microwave and Optical Engineering MOE group – Department of Electrical and Information Engineering of Politecnico di Bari and the enterprise LinearBeam (Ruvo).

LinearBeam is currently building a linear accelerator (LINAC) for hadron therapy, a new promising cancer treatment, which unlike classical radiotherapy (which employs high-energy photons, in the X-ray band) employs hadron (subatomic charged particles, in this case protons). Hadron therapy permits greater accuracy in targeting cancerous lesions, thanks to the Bragg peak, a physical phenomenon that can be employed in order to deliver a higher dose of radiation at a specific depth, where the tumor is localized, while sparing the surrounding healthy tissues.

As widely known, particle accelerators (and thus LINAC) employ radiofrequency electromagnetic fields in order to accelerate charged particles to high energies. In order to distribute the RF electromagnetic power to the resonant cavities which constitute the accelerant system of the LINAC, a RF power distribution network must be employed. This subsystem works under high RF power, and if not properly dimensioned by using the right components RF breakdown can happen inside those devices, leading to a wide variety of issues in the entire system.

In this work a particular effect which can lead to RF breakdown in vacuum-filled waveguide-based components is studied, namely the multipaction effect. Multipaction is practically an electronic avalanche which can happen in waveguide-based components under vacuum conditions when certain conditions arise.

Not only multipaction can lead to arcing, corona discharges and thus RF breakdown, but also to a wide variety of issues which must be avoided in order for the RF power system to correctly operate.

In chapter 1 a general introduction to particle accelerators and the components used in their RF power distribution network is provided. In particular the general theory of waveguides, phase shifters, circulators, ceramic windows, and directional couplers has been revised. Then a particular type of directional coupler will be studied, the Riblet short slot coupler, which is often employed in RF power distribution systems as power divider. This device will be studied in depth in chapter 3.

Chapter 2 will instead focus on the details of the multipaction effect, illustrating the physical phenomenon itself, providing a basic review of its theory and exploring its connection to the secondary emission phenomenon, which consist in the emission of secondary electrons from metallic walls when those are hit by incident primary electrons with a certain energy and direction.

The two main models for the physical modelling of secondary emission will be described, namely the Vaughan's and the Furman-Pivi models. Those two can be employed along with Particle-In-Cell algorithms to simulate in software the multipaction effect.

Chapter 2 concludes with the analysis of multipaction effect in parallel plates waveguides, by employing two different software packages, namely CST Particle Studio and the ECSS multipactor tool, the latter provided by the European Space Agency (ESA) for the detection of multipaction in simple structures. The results obtained with the two different software have been compared, showing a certain degree of agreement between the two.

In chapter 3 finally the analysis performed on the Riblet short slot coupler, object of the experimental phase of this work, are presented. Initially the physical device has been characterized by employing a VNA for the measurements of its scattering parameters.

Then a model of this device has been developed in CST MWS, and the s-parameters resulting from the electromagnetic analysis of the model have been compared with the ones of the physical device, showing agreement between the two. Finally, a multipaction analysis employing CST PS has been performed, obtaining the threshold of the input power that must not be surpassed if one wants to avoid multipaction, and thus possibly RF breakdown.

# 1 RF power distribution systems for linear accelerators

---

In this chapter the most important waveguide components used for power distribution in RF particle accelerators will be illustrated, with a special focus on hybrid couplers, which will be the main topic of this work, both from an electromagnetic analysis point of view, with its modelling in CST and the determination of its simulated S-parameters, but also for its multipaction analysis in chapter 3. A brief introduction to the structure and working principle of linear accelerators will be provided, in order to understand the context under which the analyzed RF device operates.

A mention, at the end of this chapter, will be presented for a typical RF power distribution network which could be employed in a standard S-Band LINAC.

## 1.1 General particle accelerator classification

A particle accelerator is a complex system designed with the goal of accelerating charged particles (electrons, protons, ions, etc.) at high energies by means of electromagnetic fields, in order to generate at its output a particle beam.

While older designs used electrostatics fields in order to accelerate particles, modern ones use high frequencies, high power electromagnetic fields, so RF devices are vastly employed in the construction of modern particle accelerators. Indeed, particle accelerator research along with radars and telecommunication systems development is one of the fields which brought interest in RF design in post-World War II period.

Modern particle accelerators can be subdivided in three main categories:

- The cyclotron, which basically consists of a cylindrical vacuum chamber where are placed two D-shaped electrodes, separated by a gap. A strong static magnetic field provided by a permanent magnet or a coil permeates the chamber, and between the plates an electric potential is applied. Every time a charged particle passes between the two gaps is accelerated by the electric field which exist in the gap itself, and doing so it gains energy; meanwhile the magnetic field  $B$  provides a centripetal acceleration to the particle, due to the Lorentz force, which is responsible for the classic spiral-shaped trajectory of the charged particle; this makes possible the containment of its motion inside the cylindrical chamber. In order to correctly accelerate the particles, the electric field between the plates must be reversed at every half-cycle, that is every time the particle passes between a different gap. In order to achieve synchronism between the particle trajectory and the electric field between the plates, the frequency of operation of the RF power source responsible for the electric field must be fixed to the value:

$$f = \frac{qB}{2\pi m} \quad (1.1)$$

with  $q$  the charge of the particle,  $m$  its mass and  $B$  the magnetic field.

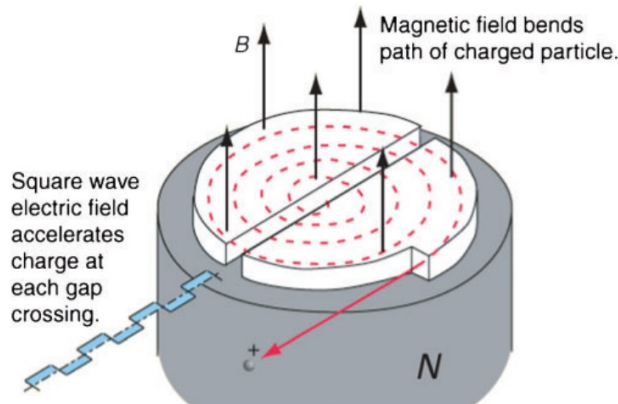


Fig. 1.1 Schematic representation of a cyclotron [29].

The classical cyclotron is highly limited by relativistic effects; it is possible to reach speeds in the order of just a few percentages of the speed of light. To overcome this obstacle improved design of the cyclotron have been developed, with the most popular one being the synchrotron.

- The synchrotron basically is an evolution of the cyclotron. In this device also the magnetic field is synchronized with the particle trajectory, so it is not constant anymore like in the cyclotron. This implies that large electromagnets must be employed in a synchrotron in order to generate the time-varying magnetic field (in larger design superconducting elements are used in order to reach high values of B).  
By adjusting the magnetic field, synchronizing it with the particle motion, it is possible to achieve a fixed closed-loop trajectory, which does not change at every cycle. This makes possible to accelerate the particles almost indefinitely (in reality, until relativistic limits are reached). The Large Hadron Collider (LHC) at CERN in Geneva, which constitute the largest particle accelerator on the planet, is a synchrotron and it unfolds over a circumference of 27 km, approximately; this gives an idea on the dimensions that such systems could reach. This large extension let the particle reach energies in the order of TeV (teraelectronvolt).
- Lastly, but not in order of importance, there are linear particle accelerators, also called LINACs, which provide particle acceleration by accelerating particles in a straight trajectory. This work is mainly focused on RF systems for linear accelerators, so a more in-depth overview of those systems will now be discussed.

## 1.2 General structure and principle of operations of a linear particle accelerator

A linear particle accelerator, from now on LINAC, is a system that accelerate particles in a linear, straight trajectory.

There are two types of LINACs, and their distinction is based on the working principle: we can have standing wave (SW) or travelling wave (TW) LINACs. The former is usually employed for accelerating protons and other heavy particles, even though it could also be used to accelerate electrons; the latter instead is mainly used for accelerating electrons and lighter particles to speeds close to the speed of light. This is possible since the electron is a light particle, with a mass three order of magnitude smaller than the one of the proton; so at energies of circa 1 MeV electrons have already reached speeds near the speed of light [25]. In the medical field linear accelerator are mainly used for two purposes:

- Generate ionizing radiation (X-rays) by accelerating electrons and making them collide with a metallic target made of tungsten, gold, platinum or other materials with a high atomic number. This leads to x-ray generation by the mechanism of bremsstrahlung (radiation by deceleration): basically electrons by impacting with the metal target experience coulombian forces due to the interaction with the atomic nuclei of the metal, leading to a change in trajectory of the electron and basically deceleration; the energy lost by deceleration is emitted as electromagnetic radiation, that means photons, which will have very high energies (in the x-ray spectrum) if the energy of the impacting electron is high and the coulombian force is so high that the electron lose most of its energy (this is the reason why high atomic number metals must be used as target). This is the basic principle by which radiotherapy machines works [25].
- Another novel use of LINACs in the medical field is the generation of a proton beam (but also other heavier particles as carbon ions could be used) in order to treat cancers and tumors, with the possibility of targeting only the cancerous lesion and saving the surrounding healthy tissue. This takes the name of particle therapy (PT) or hadron therapy in the case of protons (which in particle physics are classified as hadrons).

For radiotherapy (that is x-ray production) both standing wave and travelling wave LINACs could be used; for particle or hadron therapy instead a standing wave LINAC is the only available option. The LINAC present at the facility under which this work has been carried on, being an accelerator dedicated to hadron therapy, is a standing wave LINAC.

Besides from the type of accelerated particles, TW and SW LINAC have a different structure and a different working principle. So this brief description will be focused on the standing wave typology, leaving from the picture the travelling wave configuration.

A standing wave LINAC is often composed of a certain number of resonant cavities kept under vacuum, which are used to accelerate the charged particles by means of an electromagnetic field. Often if a high number of resonant cavities is required (in order to reach higher energies) they are grouped together in modules, with each module constituted of a minor number of resonant cavities and each cavity having as input the particles at the output of the previous one.

In the same way more modules can be mounted in a cascading configuration; the next module will have as input particles with higher energies than the previous one, so it could require a redesign or a fine-tuning in its characteristics.

By exciting a single cavity with a high-power RF signal having the same frequency of the resonant peak of the cavity, a standing wave will be created inside the structure; by optimizing its design in order to achieve the optimal configuration of the electromagnetic field, this standing wave can be used to accelerate the charged particles.

In order to achieve acceleration, it must be ensured that the electromagnetic field is at its peak and have the right polarity (phase) when the electron is passing at the center of the cavity [25]. This must be true for all the cascading cavities; in order to achieve this result, it is mandatory that the RF fields in each cavity are synchronized somehow.

This could easily be obtained if all the cavities are powered by the same source, electromagnetically coupling them all together. In this case the electromagnetic configuration inside the entire structure can be explained by the theory of normal modes of oscillation, in the same way N pendulums coupled together by a spring exhibits N different modes of oscillations, with each one having its own resonant frequency [25].

For large systems however, where it is required a high number of cavities in order to reach higher energies, it becomes necessary to employ more RF sources, with each source powering a certain number of cavities (for example a single klystron could be used to power two modules, each one constituted by three cavities). This makes necessary to synchronize in some way the various RF sources, in order to achieve perfect timings between each cavity.

The one described above is the accelerant system of the LINAC; but a linear accelerator is a very complex structure, and the accelerant system itself is just a block of a complex plant.

Precisely, in a LINAC the following subsystems could be individuated:

- The accelerant system, constituted by a certain number of cavities, whose basic working has just been described.
- The particle source, which emits the particles that will be accelerated; in case of electrons the mechanism of thermionic emission or photoemission could be exploited in order to generate them, while for protons or heavy ions an ion source must be employed [25].
- The vacuum system, which keeps the resonant cavities under high vacuum, that is a necessary condition in order to achieve good accelerations. Indeed, the accelerated particle inside the cavity should be able to move freely, without collision with gas molecules; moreover the high electric field inside cavities could ionize gas molecules, giving rise to a corona discharge, which could damage the walls of the cavity and it is absolutely to avoid [25].  
Usually a pressure level in the order of at least  $10^{-6} \div 10^{-8}$  Torr must be kept inside the cavities, employing a vacuum pump and assuring a good vacuum conductance between each section of the LINAC, avoiding vacuum-leaks which could damage the entire system [25].
- The RF source, which generates the high-power high-frequency signal used to drive the cavities; for low-energy LINACS under 10MeV magnetrons can be employed as RF sources. For higher energies the use of klystron as power sources becomes necessary, as they're able to provide more power and generally more stability [25].
- The RF power distribution system, that distributes the RF power from the RF sources to each cavity. Besides from waveguides, used to transport the electromagnetic power, other types of microwave devices are used in this system: this include hybrid couplers, phase shifters, RF ceramic windows, circulators and high-power RF loads.  
The main topic of this work is the multipaction effect in components of the RF power distribution system, specifically in hybrid couplers employed as power dividers, so in this chapter the focus will be on illustrating the various waveguide-based components used in the RF power distribution system of the LINAC; in the final paragraph a brief illustration of a basic version of a possible power distribution system in a linear accelerator will be provided.

- The water-cooling system. Indeed under steady state operation the LINAC develop a large amount of heat, which leads to thermal expansion of the resonant cavities, which in turn leads to a shift in their resonant frequencies. Even though LINACS can be provided with an automatic frequency control (a feedback system to sync the frequency of the power signal generated by the source with the resonant frequencies of the cavities), the thermal expansion can still lead to shift in the working frequency of the LINAC, with possible unexpected behavior. This makes necessary the use of a water-cooling system, which dissipate the heat developed by the accelerator under normal working conditions [25].
- A computerized control system, which provides the automation necessary to control and integrate all the previously mentioned subsystem, enabling the human operator to control the LINAC operations and its output beam; this system should also monitor the state of the machine by analyzing the signals coming from the various sensors present on the machine, whose output is acquired via a data acquisition system and transmitted to the computer system using a robust transmission protocol.

As previously mentioned, a LINAC is a very complex system whose complexity and size increase with the beam energy required at its output by the specific application for which the system is employed.

From now on the focus will be on the RF power distribution system, analyzing the basic waveguide components employed in it and showing in the final paragraph of this chapter a possible basic RF power distribution network which could be used in a LINAC, giving an insight on how all those components work together.

## 1.3 Waveguides

In high power RF applications it is not feasible transporting electromagnetic power in cable structures, mainly because of high losses due to skin effect; moreover in some applications like particle accelerators it is strictly required that power is transported by waveguiding structures.

For example, a resonant cavity (the standing-wave structure used to accelerate particles) requires an excitation with a high-power RF signal, which could only be provided by a waveguiding system.

Waveguides are simply constituted by hollow metallic tubes, that comes in different shapes (circular, rectangular, elliptical section, etcetera) and sizes. In those systems an electromagnetic RF field can propagate inside the structure, under certain conditions.

The goal of this brief chapter is not to do an extensive review of waveguiding systems, widely known in literature, but to summarize some important results to keep in mind that can be useful in this work.

As known from waveguiding system theory, a generic electromagnetic field inside the waveguide (at a certain distance from the excitation, such as that all the evanescent modes can be neglected) can be expressed as a linear combination of a certain number of modes.

If  $x, y, z$  is the reference frame of the waveguiding system and  $z$  is taken as the direction of propagation of the electromagnetic field inside the structure, each mode will have its own peculiar configuration in a given transversal section.

Three different modes are usually possible in a generic waveguiding system:

- TEM (Transverse Electro-Magnetic) mode, where both the electric and the magnetic field are always transverse to the direction of propagation  $z$ ; that means that the  $E$  and  $H$  vectors always lie in the transversal plane (parallel to the  $xy$  plane). There is no  $E_z, H_z$  component.

This mode is only possible in structures composed of at least two separate different conductors, like in the coaxial cable or in parallel plates waveguide; the latest will be used in chapter 2 for a basic analysis of the multipaction effect.

The TEM mode, unlike TE and TM modes, does not have a cutoff frequency; it can (theoretically) propagate at any frequency in the system. In practice however structures like coaxial cable have always an upper limit in frequency, due to increases in losses as the frequency increase.

- TE (Transverse Electric) mode. In this mode the electric field is always transverse to the direction of propagation (z), so the electric field will always lie in the xy plane. However, the same is not true for the magnetic field H, which will have its own non-zero  $H_z$  component.

The solution for the electromagnetic field inside a structure that support a TE mode is obtained by solving the Helmholtz equation for the  $h_z$  modal function, and by imposing the boundary conditions of the structure to the problem. In case of TE mode, supposing that the walls are constituted by a PEC conductor, the problem to solve becomes [2]:

$$\left\{ \begin{array}{l} \nabla^2 h_z + k_c^2 m,n h_z = 0 \\ \frac{\partial h_z}{\partial \hat{n}} = 0 \end{array} \right. \quad (1.1a)$$

$$\left\{ \begin{array}{l} \nabla^2 h_z + k_c^2 m,n h_z = 0 \\ \frac{\partial h_z}{\partial \hat{n}} = 0 \end{array} \right. \quad (1.1b)$$

Where  $k_c$  is the eigenvalue of the problem, and its value and expression depend on the shape of the geometrical section of the device itself.

Eq. 1.1b gives the boundary condition (Neumann boundary condition) that must be satisfied on the surface of the waveguide for the modal solution  $h_z$ . The direction  $\hat{n}$  is the normal to the surface of the metallic walls.

By solving this PDE with its boundary condition, we get the modal solution  $h_z$ , from which the physical component  $H_z$  of the magnetic field can be found. All the other components ( $E_x, E_y, H_x, H_y$ ) can be found in function of the modal solution applying relations derived directly from Maxwell's equations (slightly modified in order to solve this specific problem). The entire development of this theory is reported in [2]. The propagation constant  $\beta$  along the direction of propagation of the mode under analysis is given by:

$$\beta = \sqrt{k^2 - k_c^2} \quad (1.3)$$

Where  $k$  is the propagation constant of an electromagnetic plane wave propagating inside the material which fills the waveguide:

$$k = \omega \sqrt{\mu \epsilon} \quad (1.4)$$

With  $\mu, \epsilon$  respectively the magnetic permeability and dielectric permittivity of the material inside the waveguide.

For vacuum-filled waveguides those will correspond to the magnetic permeability and dielectric permittivity of free space, which will give us in this case:

$$k = \omega/c \quad (1.5)$$

For rectangular waveguides, by imposing the Neumann boundary condition, the eigenvalue of the TE problem assumes the expression:

$$k_{c,mn}^2 = \left(\frac{m\pi}{a}\right)^2 + \left(\frac{n\pi}{b}\right)^2 \quad (1.6)$$

Where a, b are the dimensions of the rectangular section of the waveguide ( $a>b$ ), and m, n are integer indexes that individuates a specific TE mode; those discrete indexes arise from the boundary conditions at the walls, in the same way for which the frequencies of oscillation of a string bounded at its ends are distributed in discrete way; here we have two integer numbers just because the boundary conditions are applied in two direction, x and y.

Is it now obvious that the propagation constant could become imaginary, giving rise to an evanescent, non-propagative mode in the waveguide itself, if  $k^2 < k_{c,mn}^2$ . In this case the mode is said to be in cutoff, since it is not propagating in the waveguide. In order to have propagation, it must be  $k^2 > k_{c,mn}^2$ , that is, for rectangular waveguides:

$$\omega^2 \mu \epsilon > \left(\frac{m\pi}{a}\right)^2 + \left(\frac{n\pi}{b}\right)^2 \quad (1.7)$$

Which leads us to, for rectangular waveguides:

$$f > \frac{1}{2\pi} \sqrt{\frac{\left(\frac{m\pi}{a}\right)^2 + \left(\frac{n\pi}{b}\right)^2}{\mu \epsilon}} \quad (1.8)$$

That is, in order to have a propagating mode, the frequency of the excitation signal must be greater than a certain frequency; this frequency is called the cutoff frequency of the waveguide for that particular TE mode.

$$f_{c_{TEmn}} = \frac{1}{2\pi} \sqrt{\frac{\left(\frac{m\pi}{a}\right)^2 + \left(\frac{n\pi}{b}\right)^2}{\mu\epsilon}} = \frac{c}{2\pi} \sqrt{\left(\frac{m\pi}{a}\right)^2 + \left(\frac{n\pi}{b}\right)^2} \quad (1.9)$$

So, it can be said that a waveguide acts as a high pass filter for a certain m, n mode: only frequencies above the cutoff frequency of that particular mode will give rise to a propagating mode.

For TE modes, the one with the lowest cutoff frequency is the TE<sub>10</sub>. This implies that below the frequency:

$$f_{c_{TE10}} = \frac{c}{2a} \quad (1.10)$$

there cannot be any TE mode. It can be shown that TM modes have higher cutoff than any TE mode; only TM<sub>11</sub> mode can exist.

So this limit fix the lower frequency for which propagation can exists in a rectangular waveguide of dimension a, b with a>b.

- TM (Transverse Magnetic) modes, instead, can be thought as the dual of TE modes: the magnetic field is transverse to the direction of propagation z, so H can only lie in planes parallel to the xy plane. There is no magnetic field component along the z axis,  $H_z = 0$ . The electric field instead is present, and its modal function  $e_z$  can be computed by solving the Helmholtz equation and applying this time the Dirichlet boundary condition, which gives [2]:

$$\begin{cases} \nabla^2 e_z + k_c^2 m, n e_z = 0 & (1.10a) \\ e_z = 0 & (1.10b) \end{cases} \quad (1.11)$$

The same considerations and formulas discussed for TE modes, are valid for the TM case. The only difference is that for TM we cannot have the TM<sub>10</sub> mode, since it cannot physically exist.

The considerations above are valid for all the waveguides whose section does not change along the direction of propagation; so they are valid for the rectangular, circular, elliptical section case, etcetera. What changes is the eigenvalue of the problem,  $k_c^2$ , which assume a different expression based on the shape of the section of the waveguide itself, due to the different kind of boundary conditions that each shape provides.

For structures constituted of two or more conductors, both TE/TM and TEM mode are possible. For example, a coaxial cable can support both TEM and TE/TM modes. However, structures whose walls constitute a simply connected domain (which is, the walls are constituted by a unique conductor) cannot support TEM modes; only TE and TM modes are permitted.

Now, TEM modes do not have a cutoff frequency; they can propagate as well as DC current (think about how in a coaxial cable also signal of very low frequency can be applied).

This means that structures like coaxial cables and parallel plates waveguides can be used to transport also low frequency signals.

However, for rectangular waveguides there are no TEM modes, and the lowest possible frequency which can excite the fundamental mode  $TE_{10}$  is the cutoff frequency of the  $TE_{10}$  mode:

$$f_{c_{TE_{10}}} = \frac{c}{2a} \quad (1.12)$$

For example, the waveguide standard WR284 has dimensions  $a=72.14\text{mm}$ , and  $b=35.56\text{mm}$ . Its lower cutoff frequency will be given by:

$$f_{c_{TE_{10}}} = \frac{c}{2a} \approx \frac{299792000 \text{ m/s}}{2 * 72.14 * 10^{-3} \text{ m}} \approx 2.078 \text{ GHz} \quad (1.13)$$

That means that below 2.078GHz there are no propagative modes inside a WR284 waveguide.

Usually, propagation in waveguides is kept monomodal, that is only a mode is allowed to propagate, the fundamental mode  $TE_{10}$ .

In order to do so the signal that is used for the excitation of the waveguide must have a frequency that is above the cutoff frequency of the  $TE_{10}$  mode, but below

the cutoff frequency of the next mode, which is TE<sub>20</sub> for standard waveguides; this mode, applying (1.8) have a cutoff frequency given by:

$$f_{c_{TE20}} = \frac{c}{2\pi} \frac{2\pi}{a} = \frac{c}{a} \simeq \frac{299792000 \frac{m}{s}}{72.14 * 10^{-3} m} \simeq 4.156 GHz \quad (1.14)$$

All those considerations are made in vacuum obviously (vacuum-filled waveguides), where the phase velocity of the guided mode correspond to the speed of light c.

So, in order to keep a monomodal propagation inside a WR284 waveguide, the excitation signal should have frequencies inside the range 2.078GHz-4.156GHz. In practice, the working frequencies range of WR284 waveguides is taken much more restricted than the one previously calculated: the recommended frequency range for WR284 waveguides is from 2.60GHz to 3.95GHz.

This ensures monomodal propagation, without excitation of any higher order or evanescent modes.

The WR284 standard has been taken as an example in illustrating cutoff frequencies because it is the standard dimension of the ports of the component which will be analyzed in chapter 3, for its electromagnetic and multipaction analysis.

Besides standard regular waveguides, indeed, there is a wide range of components like phase shifters, hybrid couplers, power dividers, etcetera that make use of waveguide technology, basing their own working principle on basic standard waveguide theory. Those components will be briefly illustrated in the following paragraphs, with a special focus on hybrid couplers, specifically the Riblet short slot coupler, which will be analyzed in detail in its electromagnetic and multipaction analysis in chapter 3.

Besides from particle accelerators, waveguide components are widely used in radars, satellites, and other RF systems dealing with high frequency, high power electromagnetic signals.

The working frequency range of WR284 standard is in the so-called S-band, which covers the electromagnetic spectrum in the range 2GHz-4GHz.

The hadron accelerator under construction at the facility in which this work has been carried on work at a frequency of 2.99792GHz, so basically in the S-band of the electromagnetic spectrum. The chosen frequency of work of the system resembles the numeric value of the speed of light: indeed, this value is appropriately chosen in particle physics so that all the others physical quantities whose

formulas contain the speed of light in some ways, scale up quite easily, making calculations way easier.

Besides from regular, “straight” waveguides, there are so called “bends” which are curved waveguides used when it is necessary to guide the RF power in other directions. For rectangular waveguides two different geometries are available, namely E-plane bends and H-plane bends. In the former the lateral walls are left unchanged, while top and bottom walls are curved (which means the side of length “a” is curved); in the latter instead top and bottom walls are left unchanged, while lateral walls are curved (which means the side of length “b” is curved). An example of bends is given in the image below, showing the difference between E-plane and H-plane topology.



Fig. 1.2 E-plane (bottom) vs H-plane bends (top) [30]

Another interesting and useful structure is the corrugated flexible waveguide which, as the name implies, provides a certain degree of mechanical flexibility in the RF power distribution system. An example of flexible corrugated waveguide is provided below.

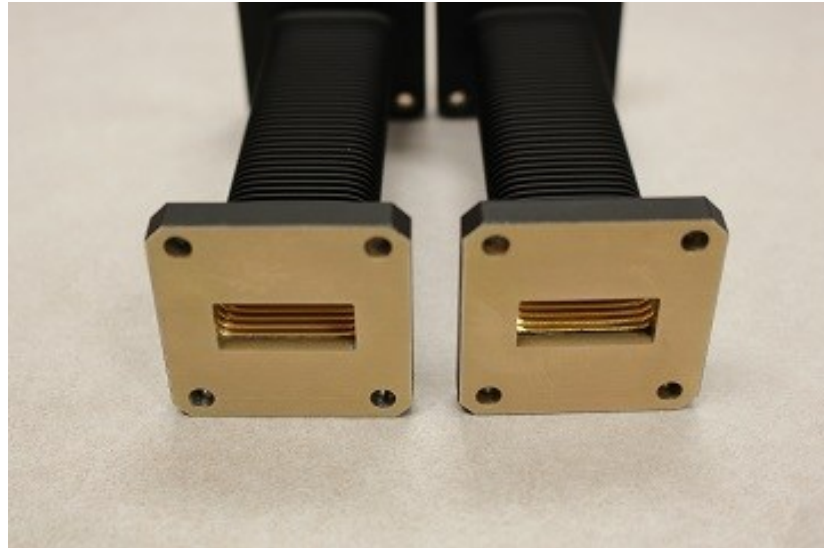


Fig. 1.3 Corrugated flexible rectangular waveguides [26]

In the following paragraphs other waveguide-based devices for RF power distribution in particle accelerators will be illustrated.

Resonant cavities will be excluded from this treatise, since they're part of the acceleration system and not of the RF power distribution network; moreover, resonant cavities constitute standing-wave devices, while waveguides are "travelling wave" devices. This work will be focused mainly on the latest, leaving in-depth analysis of standing-wave devices for future works.

## 1.4 Phase shifters

Phase shifters are usually two ports, reciprocal devices which are used to control the phase of the guided electromagnetic field.

Being reciprocal, it means that the amount of phase shift introduced in the wave travelling from one port to the other is equal to the one experienced by the wave travelling in the opposite direction; in term of S parameters that means  $S_{12} = S_{21}$ . It is also possible to build non-reciprocal phase shifters using ferrite elements [1][2], but the main focus here will be on reciprocal ones.

Generally, phase shifters in waveguide technology works by changing in some ways the effective length of the waveguide in which the electromagnetic field is propagating; this is usually achieved in reciprocal phase shifters by inserting a dielectric or conductive movable element inside the waveguide, like a piston or a plunger made of ceramic materials in case of dielectrics phase-shifting elements, or brass, copper, aluminum in case of conductive ones.

The amount of phase shift provided is a function of how much the phase shifting element penetrates inside the waveguide; so usually a mechanism like a screw is provided in order to adjust the position of the plunger inside the waveguide. This mechanical system could be regulated manually or it can be motorized, giving a certain degree of automation in the latter case (for example the phase shift at a certain port in a big RF power distribution system could be regulated programmatically or using an electronic control panel).

Phase shifters are widely used not only in particle accelerators, but also in phased array antennas (where from a single power source they are capable of providing the right amount of phase shift to each single element of the array, making possible to adjust the directivity pattern of the antenna), in radars, and basically every system where a certain control on the phase of the electromagnetic field is required.

In particle accelerators instead they are used mainly for providing control over the phase of the excitation signal for the resonant cavities.

In case of a linear accelerator (LINAC) for example there are very strict requirements on the phase relation between the excitation signals that feeds the various cavities of the system; this control is provided by phase shifters, which must be finely tuned in order to meet those requirements on the phase relationship between the various power signals that feeds each single cavity.

A good phase shifter must provide approximately the same phase shift over its entire bandwidth, which means basically a flat response, in order to avoid phase distortion; moreover, its insertion loss must be the same for all the possible phase shifts (that is, for all the positions of the plunge) in order to provide to the output the same amount of power even if the phase is changed.

In order to meet those requirements more sophisticated phase shifters have been designed; a widely known configuration for example is given in [27], where the properties of a directional coupler are used in order to provide a phase shift. Precisely this setup consists of a narrow wall hybrid coupler with its coupled and through ports both closed each one on a variable load constituted of movable periodic RF chokes; it can be shown indeed, with basic scattering matrix operations, that by closing a hybrid coupler with two variable loads on the coupled and the through ports a phase shift is achievable between the other two free ports (input and isolation, which cannot be considered isolated anymore since ports 2 and 4 are not closed on matched loads).

Phase shifters build with this setup can also sustain higher peak powers than the ones who just consists of a plunge inside the waveguide.

In the following figure is reported a representation of the described setup.

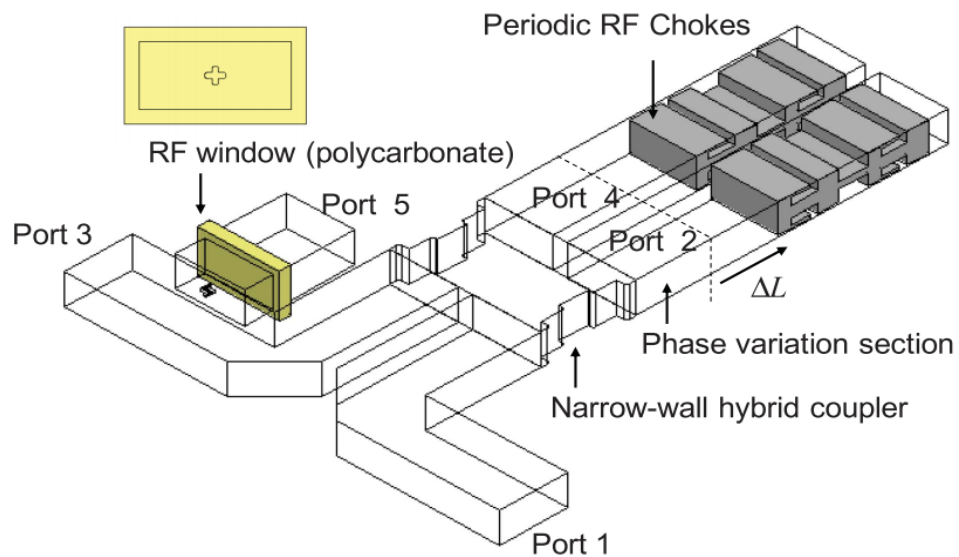


Fig. 1.4 Waveguide-based phase shifter realized with a narrow wall hybrid coupler with its through (2) and coupled (4) ports closed on variable loads [27]

## 1.5 Circulators, isolators and high-power loads

Circulators are three ports non-reciprocal devices described by the following scattering matrix [1][2]:

$$[S] = \begin{bmatrix} 0 & 0 & 1 \\ 1 & 0 & 0 \\ 0 & 1 & 0 \end{bmatrix} \quad (1.15)$$

In their basic form they are constituted by a Y symmetrical junction with an axially magnetized ferrite placed at its center. The ferrite element, which is an anisotropic material, provides the non-reciprocity in this device, thanks to the Faraday rotation effect [1][2].

Besides from being non-reciprocal, its ports are matched (that is  $S_{11} = S_{22} = S_{33} = 0$ , there are no reflections on one port when the other two are closed on their reference impedance).

It can be shown that any three-port network which is lossless, adapted and non-reciprocal is a circulator [2].

Obviously physically realizable circulators have some losses, which characterize the quality of the circulator itself, but keep their ports adapted and their scattering matrix non-reciprocal.

From its scattering matrix it can be seen that the circulator has the following behavior:

- any power signal at input at port 1 will exit from port 2, with no output at port 3
- any power signal at input at port 2 will exit from port 3, with no output at port 1
- any power signal at input at port 3 will exit from port 1, with no output at port 2

Basically, input power at one port will exit only from the next adjacent port individuated by clockwise sense of rotation, while the remaining port is completely isolated. This behavior is cyclical, it repeats itself if input power is provided to the next port, and this is what gives the device its name, and also its schematic symbol, reported below.

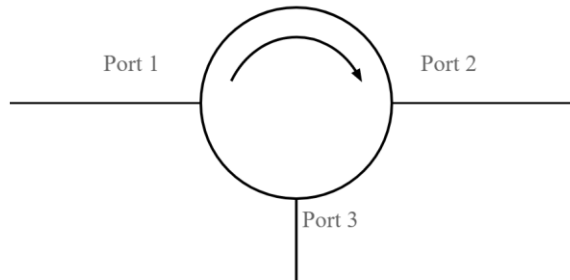


Fig. 1.5 Circulator schematic symbol [28]

Circulators can obviously have a counterclockwise sense of circulation of the power; in this case the scattering matrix will be the transposed matrix of the one previously showed. It just depends on how the ports are numbered, but the standard notation uses a clockwise sense of rotation.

Moreover, also circulators with four ports exist but their behavior is similar to the one just illustrated.

In RF power distribution for particle accelerators circulators are usually employed as isolators, which are two-ports non-reciprocal devices described by the following scattering matrix [1][2]:

$$[S] = \begin{bmatrix} 0 & 0 \\ 1 & 0 \end{bmatrix} \quad (1.16)$$

In isolators power can be transferred only from port 1 to port 2, but not in the opposite direction. If any power is applied to port 2 it will be dissipated by the ferrite inside the isolator, without reaching the other port [1][2].

Making an analogy it could be said that isolators act on RF power very much like diodes do on AC current.

The main problem with isolators is that the power coming from port 2 is dissipated from the ferrite inside it; for high-power applications like in RF power distribution systems this could not be suitable, since the ferrite could not be able to dissipate that amount of power.

So, in order to avoid this issue circulators are used instead of isolators for high-power applications; being a three-port device, the circulator must be configured in order to act as a two-port isolator by closing the port 3 on its reference impedance, and allowing the flow of power from port 1 to port 2 but not vice-versa. An example of this configuration is provided in the picture below.

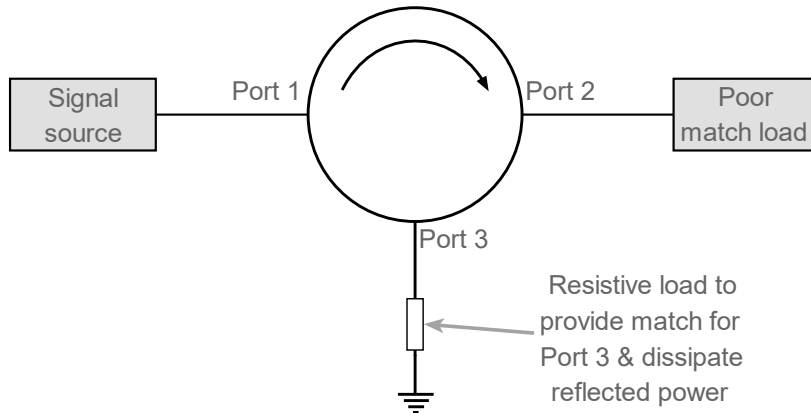


Fig. 1.6 Circulator configured as isolator [28]

In Fig. 1.5 the load at port 3 performs a dual task: it provides a match for port 3, making the resulting two-port device adapted, and it also dissipate any reflected power coming from port 2. In this way power can only flow from port 1 to port 2, and not vice-versa; moreover, any reflected power coming from port 2 is dissipated by the load connected at port 3.

This is employed in RF power distribution systems for LINAC in order to isolate the source of the high-power RF signal (usually a klystron or a magnetron) from the rest of the power distribution system. In this way if there is any reflection due to load mismatch between the klystron and the rest of the network the reflected power won't come back to the klystron, by risking damages to its systems or the tube itself; it will be instead dissipated by the load at port 3.

The load at port 3 must be able to dissipate very high amounts of power, given the high-power levels generated by the klystron; any reflected power could have the same order of magnitude of the power generated by the klystron.

So it becomes necessary to employ high-power loads capable of dissipating the heat generated by the RF power. An example of such loads are water-filled waveguide loads, where the water acts as a cooling element, absorbing the RF power (by dielectric loss, same principle of microwave oven).

In summary by employing circulators as isolators, combined with a high-power handling load, it becomes possible to protect the high-power RF source from any unwanted reflections, which could damage the source itself.

## 1.6 Ceramic windows

As previously mentioned, the accelerating cavities in a LINAC works in high-vacuum conditions, provided by a vacuum system.

Often it is not feasible to let also the RF power distribution system under vacuum, since the vacuum system can have a very high cost, both in term of economic resources and occupied space, and the RF power distribution system is way less critical than resonant cavities (even if RF breakdown inside it should always be avoided).

So a good compromise is often reached by making the resonant cavities work under high-vacuum, and the RF power distribution system as gas-filled waveguides. SF<sub>6</sub> (sulfur hexafluoride) is mostly used for this purpose, since it has a very high dielectric strength and can prevent arcing.

This means there is a part of the system that works under vacuum, and another one filled with SF<sub>6</sub>; but they also need to be electromagnetically coupled, in order for the power in the distribution system to reach the resonant cavities.

Ceramic windows just perform this job: they electromagnetically couple the RF power distribution system with the resonant cavities, while impeding the SF<sub>6</sub> (or whatever gas is used for the power system) to enter inside them.

Those devices are just constituted by a waveguide portion in which is inserted a ceramic element, usually Al<sub>2</sub>O<sub>3</sub>, an aluminum oxide known as alumina.

This material has a very high “transparency” to RF radiation, with very low losses, so it can let the electromagnetic power pass while impeding the gas to reach the vacuum section.

The vacuum-side in ceramic windows is usually coated with a thin layer of titanium nitride (TiN) in order to reduce secondary electron emission, which could lead to single surface multipaction, and consequentially to RF breakdown [25]. Indeed, ceramic windows are subjected to this phenomenon, described in chapter 2. Since the resonant cavities must be kept under high vacuum because their walls could be damaged by any gas inside them (since it could lead to a corona discharge), ceramic windows constitute a somehow critical part in the accelerator, and their breakdown (which would allow the gas to pass inside the cavities) even if rare must be avoided.

In the following pictures a “sane” ceramic window it is showed, followed by one in which RF breakdown due to single surface multipaction has happened. The cracks on the last one show how easily the gas could permeate the vacuum section if RF breakdown happen on the window.

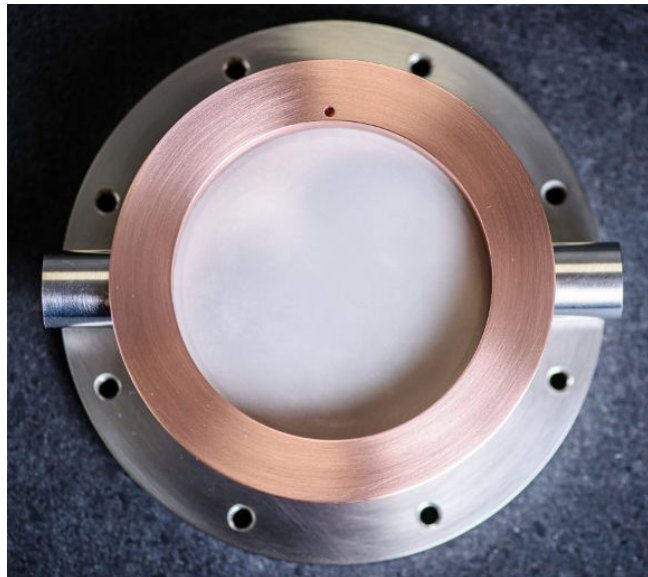


Fig.1.7 RF ceramic window [31].

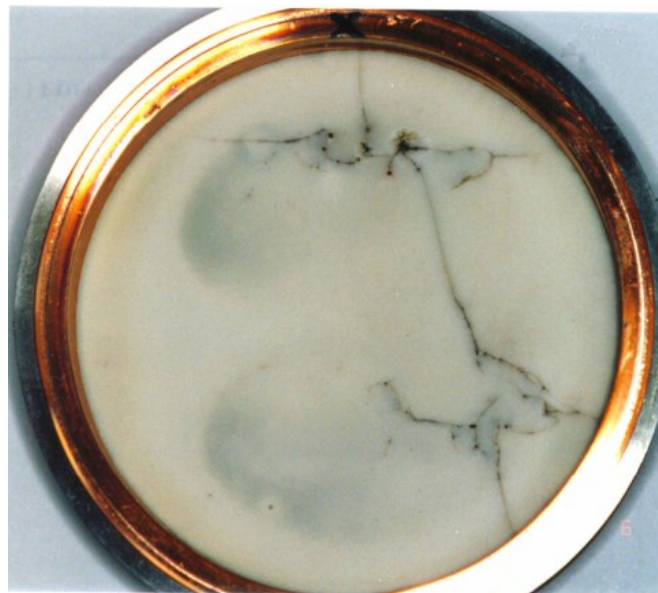


Fig. 1.8 Broken ceramic window, with cracks due to RF breakdown by single surface multipaction [14].

## 1.7 Directional couplers

Directional couplers are widely used in the RF power distribution system of particle accelerators; indeed in this context they're often employed as power dividers (even if they can have a wide range of applications).

The term “directional couplers” describe a wide family of devices; even considering only waveguide-based systems a lot of topologies are available for the design of hybrid couplers.

Here an introduction to the generic theory of directional couplers will be provided; then a specific one will be analyzed, namely the Riblet short slot hybrid coupler, which is the main subject of chapter 3, in which a detailed analysis will be provided for the design in CST of this device, in order to simulate the multipaction effect inside it and evaluate its multipaction threshold using the particle simulation software CST PS.

A directional coupler is a four-port matched, reciprocal and (ideally) lossless device which can be described by one of the following scattering matrices [1]:

$$[S] = \begin{bmatrix} 0 & \alpha & j\beta & 0 \\ \alpha & 0 & 0 & j\beta \\ j\beta & 0 & 0 & \alpha \\ 0 & j\beta & \alpha & 0 \end{bmatrix} \quad (1.17)$$

$$[S] = \begin{bmatrix} 0 & \alpha & \beta & 0 \\ \alpha & 0 & 0 & -\beta \\ \beta & 0 & 0 & \alpha \\ 0 & -\beta & \alpha & 0 \end{bmatrix} \quad (1.18)$$

where  $\alpha, \beta$  are real values and  $\alpha = \sqrt{1 - \beta^2}$  (since if port 1 is excited with  $P_1$  and  $P_2, P_3$  are the output powers at port 2 and 3 it should be  $P_2 + P_3 = P_1$ ).

The term  $\beta^2$  takes the name of coupling factor of the directional coupler.

The first case, 1.17, describes a symmetric coupler, in which whatever input port will be chosen the phase difference between the two output ports will always be  $90^\circ$ . For example, in a symmetrical coupler by taking as input port 1 and output ports 2 and 3, the phase difference between the signals at port 2 and 3 is  $90^\circ$ . The same is true if port 2, or 3 or 4 is chosen as input (and respectively changing the output ports accordingly to the S matrix).

An antisymmetric coupler instead provides no phase shifts between the output ports when the input is provided at port 1 or 3; instead a shift of  $180^\circ$  is present between them when the input is provided at port 2 or 4.

This behavior is the at the origin of the term “antisymmetric”, since the device has a different behavior based on the port chosen as input, and is widely exploited in telecommunication systems, since it implies that by applying two different signals at port 1 and 4 for example, the difference and the sum of the two signals appear at ports 2 and 3 respectively (presuming they’re closed on their reference impedance).

For symmetric couplers, if  $\alpha = \beta = 1/\sqrt{2}$  the device goes under the name of “hybrid coupler”, and it basically provides equal power division between the two output ports. In this case the scattering matrix becomes:

$$[S] = \frac{1}{\sqrt{2}} \begin{bmatrix} 0 & 1 & j & 0 \\ 1 & 0 & 0 & j \\ j & 0 & 0 & 1 \\ 0 & j & 1 & 0 \end{bmatrix} \quad (1.19)$$

The name hybrid coupler however it is sometimes used improperly to generically indicate symmetric couplers, even if they do not provide equal power division; indeed, in some kind of devices like the one in our analysis the power division ratio could be changed, and this implies that the coupler presents hybrid performances only in certain configurations; however the important characteristic that those devices must maintain is the  $90^\circ$  phase shift between the two output ports. The following picture shows the symbol commonly used for directional couplers.

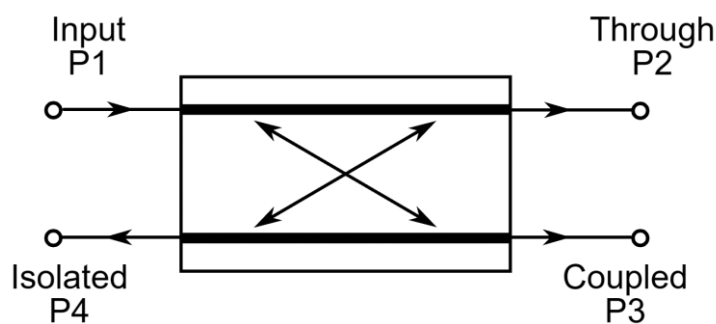


Fig. 1.9 Directional coupler electrical symbol

By taking port 1 as input, the through port (port 2) is the one from which the entire input power  $P_1$  would exit if the coupling factor  $\beta$  was zero. The coupled port (3) as the name suggest instead is the one where the coupled signal can be retrieved; the isolated port finally should be completely isolated (again as the name suggest) and in an ideal coupler its output should be null. In reality this is not true, a certain amount of power from port 1 will exit from the isolated port.

Properties of real-world, non-ideal directional couplers are defined by the following parameters, measured in dB [1]:

Coupling:

$$C = 10 \log \frac{P_1}{P_3} = -20 \log \beta \quad (1.20)$$

Directivity:

$$D = 10 \log \frac{P_3}{P_4} = 20 \log \frac{\beta}{|S_{14}|} \quad (1.21)$$

Isolation:

$$I = 10 \log \frac{P_1}{P_4} = -20 \log |S_{14}| \quad (1.22)$$

The coupling C indicates the amount of electromagnetic power that couples with port 3 (with respect to the input power at port 1).

The directivity D indicates how much power is “directed” toward the coupled port with respect to the isolated port. For ideal couplers this parameter should be infinite, since no power should be present at the output of the isolated port. In reality we can expect this value to be very high, but not infinite, since a little amount of power will always couple with the isolated port.

The isolation I express “how well” is isolated the isolated port with respect to the input. This also should be infinite in a theoretical coupler.

It can be shown that:

$$I = C + D \quad (1.23)$$

Directional couplers in particle accelerator are used for two different purposes: realize a power division, in order to distribute the power coming from a single klystron to the various resonant cavities, but also monitor the power that's flowing into certain portions of the RF power distribution system (in this context they really are employed as directional couplers; a very small percentage of the power that flow in the main circuit is spilled into the coupled port, whose output could be measured and opportunely elaborated in order to find the power flowing into the main branch).

The directional coupler which will be analyzed in the following chapters is used in the RF distribution system of the LINAC as a regulable power divider; so the focus will be mainly on this kind of use, even if essentially the devices works by the same principle. What changes is the power division ratio between the through and the coupled, based on the application of the coupler itself.  
We will now focus on this device, presenting the basic theory required for its design in chapter 3.

### 1.7.1 The Riblet short slot coupler

A representation of a partial cut-section view of the H-plane Riblet short slot coupler is provided below, followed by another picture in which the E-plane configuration is depicted too.

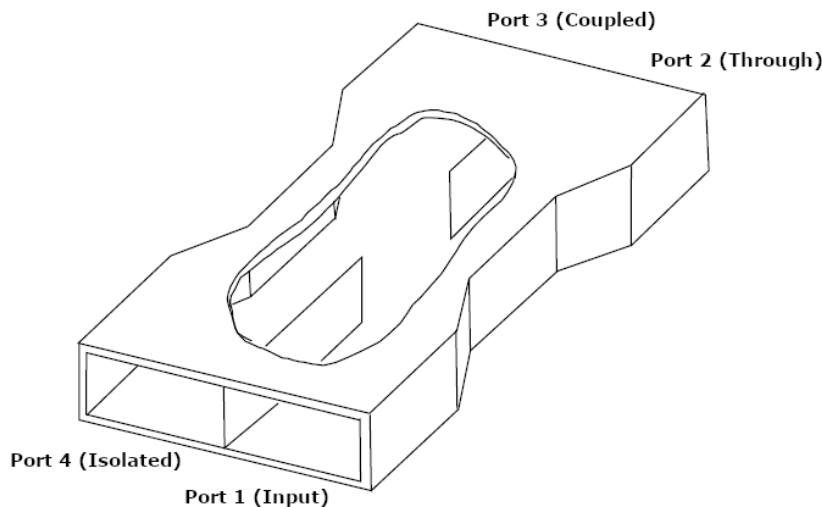


Fig. 1.10 Riblet short-slot coupler, cut-section view with numbered ports [36].

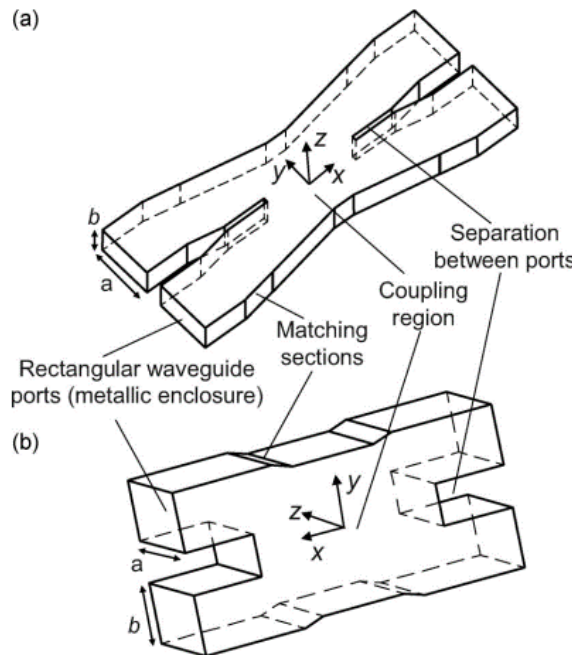


Fig. 1.11 The Riblet short-slot directional coupler; H-plane (a) versus E-plane (b) geometry [32]

The difference between the H-plane and E-plane configuration is the orientation of the rectangular waveguides that constitute the input and output ports; this implies a different configuration of the electromagnetic field in the two structures, but their working principle is the same. The version analyzed in this work is the H-plane version.

This waveguide-based coupler has been originally designed by Riblet in its H-plane geometry [33][35].

It basically consists of a rectangular section divided by a common wall interrupted at a certain point by a slot: this portion constitutes the coupling section, where the coupling between the incident (from port 1) and the coupled (port 3) electromagnetic fields happens.

Basically it can be thought as two different rectangular waveguides, coupled together, where in the center is present a slot of a certain length, which from now on will be identified as Lcs.

The length of the coupling section determines the properties of the coupler, specifically its coupling factor and the isolation.

This device exhibits symmetry both for the x and y direction (referring to picture 1.6a), so it can be analyzed using the even-odd mode technique by placing respectively a PMC (Perfect Magnetic Conductor) and a PEC (Perfect Electric Conductor) wall in place of the zx symmetry plane [32].

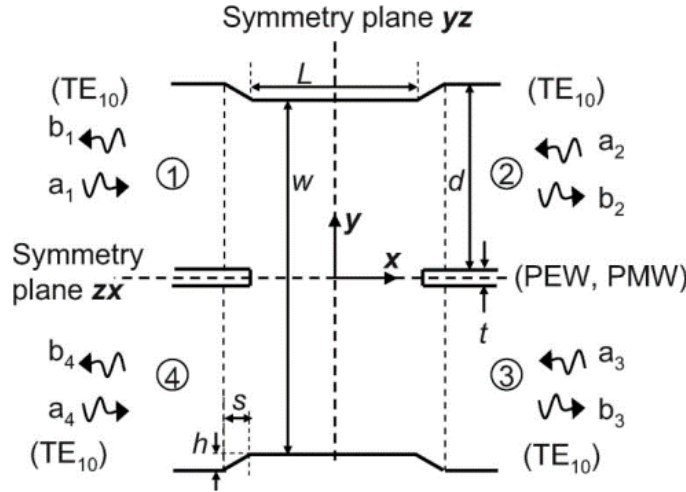


Fig. 1.12 Even/odd mode analysis of the Riblet short-slot coupler [32]

In this way the overall behavior of the device is studied by subdividing it into the study of two half portions; it can be found that [32]:

$$S_{11} = \frac{1}{2}(S_{11}^e + S_{11}^o) \quad S_{21} = \frac{1}{2}(S_{21}^e + S_{21}^o) \quad (1.24)$$

$$S_{41} = \frac{1}{2}(S_{11}^e - S_{11}^o) \quad S_{31} = \frac{1}{2}(S_{21}^e - S_{21}^o) \quad (1.25)$$

If the device is lossless, reciprocal and its ports matched,  $S_{11}$  should be zero, so the reflected voltages both in the even and the odd mode should be zero [32][33]:

$$S_{11}^e = S_{11}^o = 0 \quad (1.26)$$

This implies  $S_{41} = 0$  too; so if the device is matched it also exhibits isolation. Instead, the scattering coefficients of the transmitted voltages from port 1 to port 2 of the even and odd modes are given respectively by:

$$S_{21}^e = e^{j\varphi_e}, S_{21}^o = e^{j\varphi_o} \quad (1.27)$$

Where  $\varphi_e, \varphi_o$  are respectively the phases of the transmitted waves of the even mode and the odd mode, the first obtained when the symmetry plane zx is replaced with a PMC, the second when it is replaced with a PEC.

This analysis leads to the scattering matrix of the device, which can be showed it is given by [32]:

$$[S] = e^{j\frac{\varphi_e + \varphi_o}{2}} \begin{bmatrix} 0 & \cos\delta_{eo} & j \sin\delta_{eo} & 0 \\ \cos\delta_{eo} & 0 & 0 & j \sin\delta_{eo} \\ j \sin\delta_{eo} & 0 & 0 & \cos\delta_{eo} \\ 0 & j \sin\delta_{eo} & \cos\delta_{eo} & 0 \end{bmatrix} \quad (1.28)$$

With:

$$\delta_{eo} = \frac{\varphi_e - \varphi_o}{2} \quad (1.29)$$

We can compare the obtained scattering matrix for this device with the one of a generic coupler [32]:

$$[S] = e^{j\varphi_{31}} \begin{bmatrix} 0 & c_i e^{j\Delta_{23}} & c_d & 0 \\ c_i e^{j\Delta_{23}} & 0 & 0 & c_d \\ c_d & 0 & 0 & c_i e^{j\Delta_{23}} \\ 0 & c_d & c_i e^{j\Delta_{23}} & 0 \end{bmatrix} \quad (1.30)$$

$$c_d = \sqrt{1 - c_i^2} \quad \Delta_{23} = \varphi_{21} - \varphi_{31} = (2n + 1) \frac{\pi}{2} \quad (1.31)$$

This implies that the power division ratio between ports 2 and 3 is given by [32]:

$$r = \frac{|S_{31}|}{|S_{21}|} = \frac{\left| j e^{j \frac{\varphi_e + \varphi_o}{2}} \sin \delta_{eo} \right|}{\left| e^{j \frac{\varphi_e + \varphi_o}{2}} \cos \delta_{eo} \right|} = |\tan \delta_{eo}| = \left| \tan \frac{\varphi_e - \varphi_o}{2} \right| \quad (1.32)$$

This means that the power division ratio between ports 2 and 3 is governed by the phase difference between the transmitted waves (from port 1 to port 2) of the even and odd analysis. This characteristic can be exploited in order to achieve any desired power division ratio. Indeed the half phase shift  $\delta_{eo}$  between the even and odd modes is controlled by the length of the coupling section. By adjusting the length of the coupling section, L<sub>CS</sub>, it can be achieved any desired power division ratio.

Before going on with the analysis, it must be mentioned that the Riblet short slot coupler bases its whole theory on the fact that in the rectangular waveguides that constitutes the port only the TE<sub>10</sub> mode is excited (supposing monomodal propagation, as it is always the case when a waveguide is operating in the prescribed frequency range).

In the coupling section however, given its larger width than the one of the rectangular waveguides that constitutes the ports, also the TE<sub>20</sub> can be excited if the width of the coupling section is correctly dimensioned; so there will be coupling of electromagnetic power of the two modes, TE<sub>10</sub> and TE<sub>20</sub> [27] [32] [33][34].

It must however be avoided the propagation of the TE<sub>30</sub>, which is undesired for the proper functioning of the device; moreover, the wave impedances Z<sub>TEmn</sub> of the TE<sub>10</sub> and TE<sub>20</sub> modes should be equal, in order to maximize the coupling between the two modes [27]. Those requirements fix the width of the coupling section, which must be dimensioned at the central frequency at which the device will work.

Now, it can be shown that in the even analysis (zx plane replaced with PMC) the dominant mode in the coupling section is the TE<sub>10</sub>, while in the odd analysis (zx plane replaced with PEC) the dominant mode is the TE<sub>20</sub>.

This leads to the calculation of the propagation constants β<sub>TE10</sub> and β<sub>TE20</sub>, from which φ<sub>e</sub> and φ<sub>o</sub> can be derived, and finally by using 1.29 and 1.32 the power division ratio can be obtained [32]:

$$\beta_e = \beta_{TE10} = \sqrt{k^2 - k_{cTE10}^2} = \sqrt{\omega^2 \mu \epsilon - \left(\frac{\pi}{W_{CS}}\right)^2} \quad (1.33)$$

$$\beta_o = \beta_{TE20} = \sqrt{k^2 - k_{cTE10}^2} = \sqrt{\omega^2 \mu \epsilon - \left(\frac{2\pi}{W_{CS}}\right)^2} \quad (1.34)$$

$$\delta_{eo} = \frac{\varphi_e - \varphi_o}{2} = -(\beta_e - \beta_o) \Bigg|_{f=f_0} \frac{L_{CS}}{2} = -\arctan(r) \quad (1.35)$$

So in practice in order to design a Riblet short slot coupler as first the width of the coupling section must be determined, such as that the TE<sub>10</sub> and TE<sub>20</sub> both propagates in the structure while TE<sub>30</sub> and higher order modes are in cutoff condition; then the propagation constants of the even (TE<sub>10</sub>) and odd (TE<sub>20</sub>) modes at the center frequency f<sub>c</sub> can be determined by 1.33 and 1.34, and finally by fixing the desired power division ratio r the length of the coupling section L<sub>CS</sub> can be determined by inverting 1.35.

Now it becomes obvious how by keeping W<sub>CS</sub> fixed and changing the length L<sub>CS</sub> various short slot couplers that works at the same frequency but exhibits different power division ratios can be designed.

While changing the physical length of the device can be a first step to obtain a different power division ratio, the same result could be achieved by changing the so called “effective length” of the coupler section, by means of a capacitive dome, a metallic cylinder or a plunger inserted at the center of the coupling section [34]; by varying the penetration depth of the cylinder, the effective length of the coupler section changes and so does the power division ratio r.

This is suggested by Riblet in [33], and even if often is used just for a fine tuning of the power division ratio it implies the possibility to use a Riblet short slot coupler loaded with a capacitive element as a power divider with a variable power division ratio, controlled by the penetration of the capacitive element inside the coupling section.

These results have been reported from [32] and [33] since we'll make use of them in chapter 3, for the design in CST of the physical device under analysis, which is a Riblet short slot coupler with a customizable power division ratio by means of a cylinder inserted inside the coupling section.

## 1.8 Example of a RF power distribution system in a generic S-band LINAC

To conclude this chapter, a basic RF power distribution system for a generic S-band LINAC using the waveguide-based components illustrated until here is presented in the following page.

The RF power is usually generated by a Klystron. Magnetrons can be used for systems which need way less power, but for high-power systems klystrons are the way to go.

Then a circulator with its port 3 closed on a high-power RF load is employed as isolator, in order to isolate the klystron by any unwanted reflections coming from the rest of the system; indeed, any power coming from port 1 will go directly to port 2 (ideally without any power being lost into port 3), and any reflected power coming from port 2 will go to port 3 (and the load will absorb it). In this way the klystron can provide power to the system without risking any damages.

After the circulator a directional coupler employed as power divider (for example a short slot coupler) divides the power coming from the klystron in two parts: one output of the coupler/divider will feed the first cavity (through a ceramic window), while the other goes into another directional coupler, which in turn performs another power splitting in order to feed the second and the third cavity. The fourth port of the directional coupler must be closed on its reference impedance, in order to have a matched port, so that the resulting three-port device will also be matched. If the load's value slightly variates from the reference impedance value it can cause reflections, which must be avoided.

Before going into the ceramic windows that feeds the second and third cavities, the RF power is passed to two phase shifters (one for each branch), that can be manually or automatically controlled in order to keep the required phase relationships between the fields inside the three cavities (the phase of the field inside the first one could be assumed as a reference for the other two).

The example illustrated hereby just considers three cavities, but obviously the design can be extended by inserting other directional couplers employed as power dividers in order to feed other cavities, or by inserting another module like this (which employes another klystron) in “series” after the first one; the klystron of the second module however must be somehow “linked” to the first one in order to keep the required phase relationships between all the cavities.

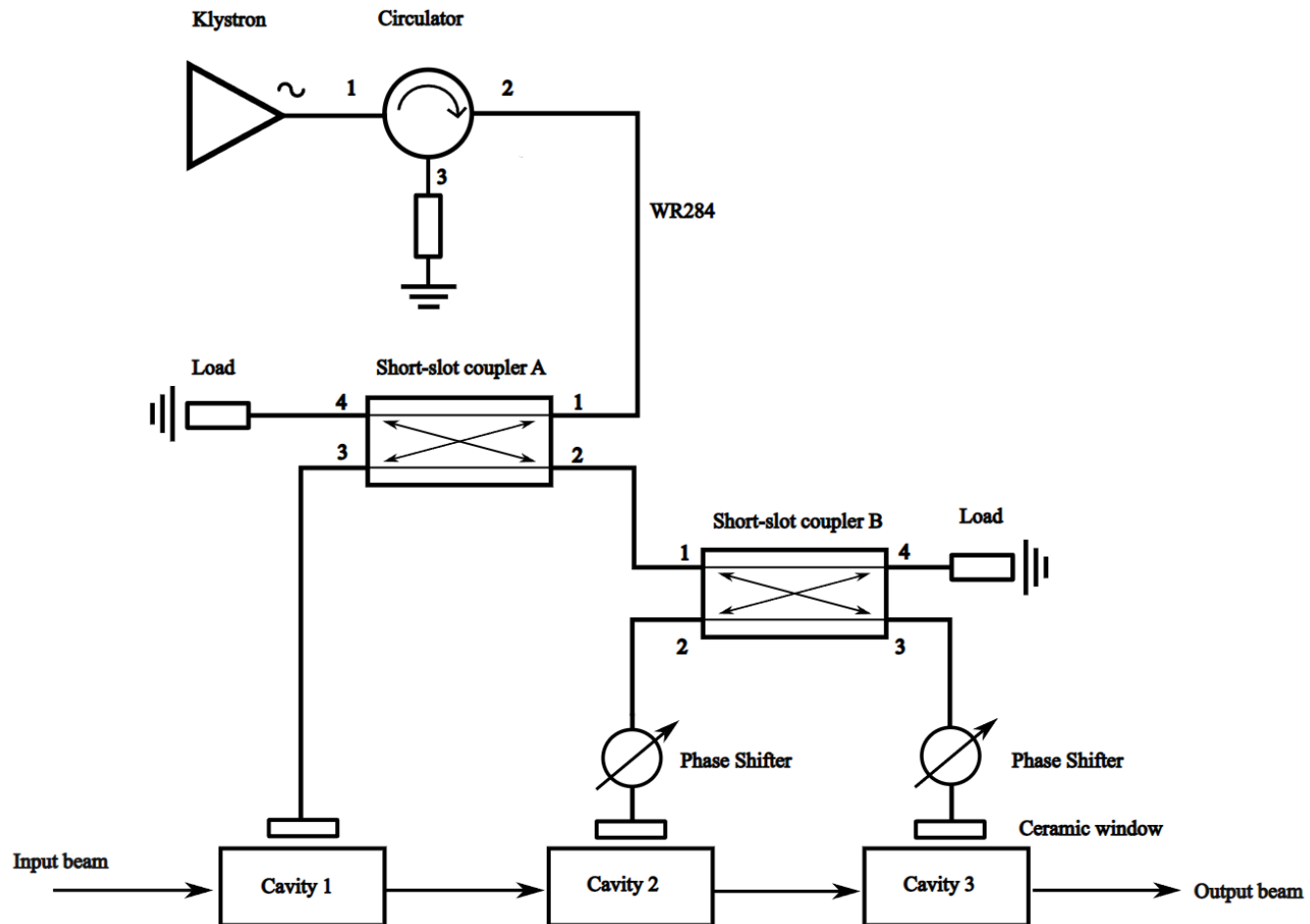


Fig. 1.13 Example of a RF power distribution system for a S-Band LINAC

## 2 Physical modelling of multipaction effect

---

In this chapter a qualitative explanation of the multipaction effect will be provided, describing the physical nature of this phenomenon and under which condition does it happens.

After that a brief illustration of the two most popular secondary emission models will be provided (Vaughan and Furman-Pivi secondary emission models), which are used by various open source and commercial software in order to simulate the multipaction effect (and other phenomena that involve secondary emission). Finally, a multipaction analysis for a parallel plates waveguide will be developed by using the software CST Particle Studio, supported by results provided by another tool, the ECSS multipactor tool provided by the European Space Agency.

### 2.1 Multipaction effect

Multipaction (sometimes also referred to as “multipactor”, especially in European countries) is a resonant phenomenon which takes place in vacuum-filled waveguides and other microwave components, previously analyzed in the first chapter (couplers, phase shifters, power dividers, etc.) when critical power levels are reached (and other conditions which will now be described are met).

Basically, it consists in an electronic avalanche caused by the release of so-called “secondary electrons” from the metallic walls of the device, due to the physical phenomenon of secondary emission. Its resonant nature is due to the fact that in order to have a growing number of electrons inside the device, the trajectories of the electrons must be in sync with the RF field inside the structure.

Multipaction is crucial in the operation of particle accelerators, as well as in RF devices used in satellites (both conditions where the microwave components usually operate under high-power, high-vacuum conditions, especially true for resonant cavities) because it limits the power levels at which the device itself can operate.

Multipaction can be indeed a precursor of RF breakdown; a growing number of electrons inside the device (which normally should not be there) can lead to an electric discharge inside it if the population of electrons reach a critical level, damaging the device itself and degrading its performances.

Moreover, even if it does not damage the device directly, multipaction can causes a wide variety of issues such as:

- an increase in noise in the device itself (due to the multiple electrons impacts with the device walls) [9];
- an increase of the temperature of the metallic walls [9][10];
- outgassing of the device walls [9][21], which could lead in turn to a corona discharge, resulting in the total disruption of the component [11]. Outgassing basically consists in the release of gaseous molecules originally trapped in the material that constitutes the walls. It can be supposed that this is another reason why OFHC copper (Oxygen Free High Conductivity copper) is used for the design of resonant cavities [25], in order to reduce outgassing.
- detuning of resonant frequencies if it is happening in a resonant cavity [3][9][10][21];
- a deterioration of the VSWR at the input ports of the device [9].

So even when it is not destructive it is often an unwanted phenomenon.

In this chapter the basics of this effect will be explained, first by providing a qualitative description and then briefly comparing the two main mathematical models used in modern literature for its simulation, which will lead us to understand how commercial software like Simulia CST Particle Studio, SPARK3D, and Ansys HFSS simulate it with computational physics techniques like Particle In Cell (PIC) [4], which will be used in this work to analyze the multipaction limit of the microwave component under study.

### 2.1.1 Qualitative description

Basically, multipaction consist in an electronic avalanche that can happen under certain conditions. In the following, a detailed description regarding what multipaction is and how it takes places is given, referring for the sake of simplicity to parallel plates or rectangular waveguides as examples, both widely studied in literature.

Generally, even when a waveguide operates as a vacuum-filled device, a small population of electrons can still exist inside it, for example due to cosmic rays hitting the device itself and causing the release of some electrons [3], due to the fact that the particles that constitutes cosmic rays have (obviously) energies very much higher than the work function of any metal; this cause of release of primary electrons is even more prominent in microwave components used in satellites, as in others low-space and deep-space systems, due to the lack in space of the Earth magnetic field, which largely (but not completely) shields the planet (and ourselves) from cosmic rays and high energy particles coming from the space. Another mechanism by which primary electrons could be emitted is the high field emission [12], which basically consist of emission of electrons from the device walls due to the high electromagnetic field present inside the structure. This could easily happen if the employed metal has a low value of the work-function.

So, for the first or the second phenomenon, a small population of primary electrons can always exist in the vacuum region of a waveguide-based device.

Those (primary) electrons randomly distributed inside the device will be accelerated by the RF field, due to the Lorentz force, and if they are energetic enough, hitting the metallic walls of the waveguide they can cause the release of secondary electrons from the metal walls by the mechanism of secondary emission. Secondary electrons which in turn will be accelerated by the RF field, reaching higher energies, and hitting the metallic walls themselves, causing the release of others secondary electrons. If uncontrolled, this could easily take to an exponential growth of electron population inside the waveguide, and giving rise to the unwanted effects previously mentioned.

Like briefly described in the introduction, multipaction is a resonant phenomenon: in order to take place the one-way transit time of the electron must be an odd number of half cycles of the RF signal in the structure, usually one half-cycle, that is  $T/2$  [5].

Imagine indeed that in a parallel plate waveguide a primary electron is “launched” initially from the plate A, with a certain initial speed  $v_0$ , when the RF signal has phase zero and the value of the electric field is zero (we suppose the electric field to grow toward a negative value as the phase increases).

As the electric field start to build up and becoming more and more negative, the primary electron will be accelerated toward the second plate B; when it reaches and hit the second plate, one or more secondary electron can be emitted (the emission itself depend on the energy of the primary electron at the impact, and by its angle of incidence with respect to the normal of the surface).

If the emission happens when the RF field has reached the end of the first half cycle (that is, the primary electron hits the surface of the plate B after  $T/2$  or an odd multiple of it), the electric field will now have its value reversed, and this will accelerate the original primary electron and the secondary emitted electron toward the surface A; when they will reach it, they can hit its walls and cause the release of other secondary electrons.

Supposing that from each impact a secondary electron is emitted, there will be now four electrons; those four will be accelerated again toward B, and the cycle will repeat, this time with more electrons, so more impacts, and it is easy to understand how this can give birth to an avalanche phenomenon and an exponential growth of the electron population inside the device, which is basically what multipaction really is.

It is easy to understand how the electrons whose trajectory is in resonance with the electric field will travel a big number of times the same path, being in sync with the RF field. Those paths are called the “multipaction trajectories” and they are characteristic of the multipaction effect. Fig. 2.1 illustrates an example of multipaction trajectories (also called resonant trajectories) of electrons in a circular waveguide under multipaction.

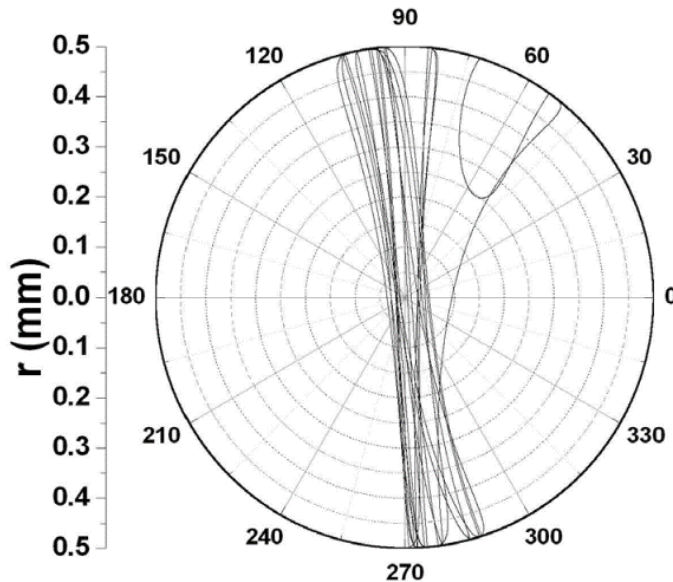


Fig. 2.1 Example of double surface multipaction: resonant trajectories simulated in a circular waveguide under TE11 mode [18]

As it emerges from the picture, resonant trajectories are very close one another. In term of degrees, it can be said that they differ by a maximum of  $15^\circ$  on the polar plot. The fact that trajectories are shifted by this amount and the absence of a unique trajectory here is due to the azimuthal component of the electric field in the structure [18], while the radial component is responsible for the acceleration of the electrons toward the center and between one surface and the other.

The fact that electrons are travelling almost the same path at every RF semi-cycle, every time leading to a certain number of emissions when they hit the walls, causes the formation of “sheets” or clouds of electrons, travelling back and forth between the two surfaces [6]. The size of those electron sheets is limited by space charge effects (mutual repulsion between the electrons that constitute the sheet) [6].

The multipaction illustrated until now goes under the name “double-surface multipaction”, because electrons bounce from one side to another of the walls; the same happens in other structures like parallel plates or rectangular waveguides.

There is however also another type of multipaction, called “single surface multipaction”, where electrons jump always on the same surface, and not on the “opposite” face, which is not needed in order to obtain multipaction in this case. Single surface multipaction is widely studied in structures like ceramic windows and resonant cavities. The fact that it happens in ceramic windows too means that also dielectrics can be affected by multipaction [8]. As shown in Fig. 2.2 single surface multipaction is due to the tangential component of the electric field (that is the component parallel to the surface).

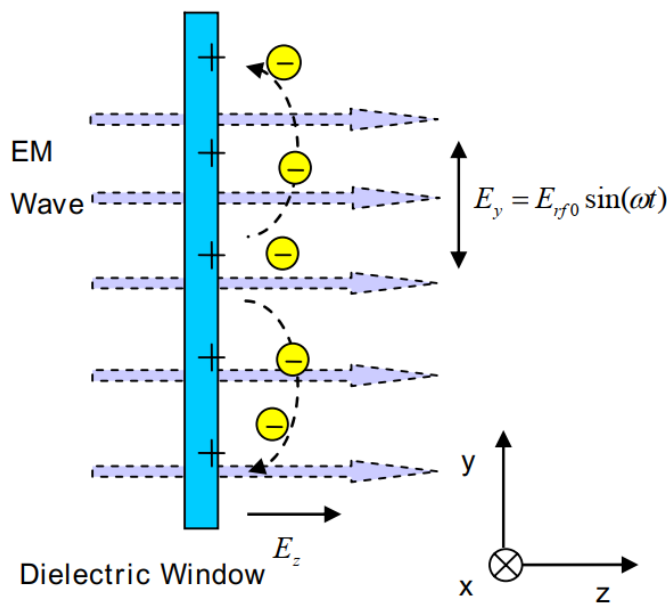


Fig. 2.2 Schematic of single-surface multipaction on a dielectric window [8]

This work will be mainly focused on double-surface multipaction effect, since it is more common in waveguide-based devices.

In this case, the triggering of the multipaction is dependent, besides from the material that constitutes the device, on other two conditions:

- The frequency-gap product ( $f \times d$ ), often provided in units of  $\text{GHz} \times \text{mm}$ , where  $f$  is the frequency of the RF signal and  $d$  is the distance between the two surfaces;
- The input power at which the device is operating. Indeed multipaction happens only after a certain critical power threshold has been surpassed. The main purpose of multipaction analysis is the determination of this threshold level, in order to always operate under it.

### 2.1.2 Multipaction simulation in software. Secondary emission: Vaughan's and Furman-Pivi's models.

The analytical derivation of the multipaction effect threshold in basic structures like parallel plates waveguides, rectangular waveguides or coaxial cable can be easily obtained due to the simple geometries of those structures.

However this is not feasible for every geometry. For example the detailed mathematical analysis of multipaction in simple parallel plates waveguide, as reported in [6] and [37] is possible just because approximative assumptions are made, like neglecting the effect of the magnetic field  $H$  (and consider only the electric field as the responsible for the Lorentz force) and because of the simple geometry. For more complex ones only software simulations can provide physically consistent results, and this task is usually achieved by a combination of the following two [11]:

- An algorithm that computes the electromagnetic field inside the structure, and the trajectory of each electron present in the free space. This is implemented by employing a PIC (Particle in Cell) approach, which together combines the computing of the electromagnetic field and the electron trajectories due to the field itself. PIC algorithms just compute the EM field using techniques like FDTD (Finite Difference Time Domain method), then they compute the Lorentz force applied on each electron, and finally apply a leap-frog or a Velocity-Verlet integration method [18] to integrate numerically the second order differential equation of motion in order to derive the trajectory knowing the initial conditions (initial position and velocity) and the Lorentz force. It must be considered that relativistic effects are left out of the picture here, since electrons do not reach very high energies in this context.
- A physical-mathematical model of the secondary emission phenomenon.

In fact, in order to model multipaction, we need to take into account the emission of secondary electrons; this, plus the resonance of the trajectories with the RF field inside the structure is the real cause of multipaction, leading to an exponential growth of electron population inside the device.

So, in order to simulate multipaction, we need to define a physical-mathematical model for the secondary emission. Two models are widely used in literature for this purpose:

- The Vaughan secondary emission model, originally described by its author in [15]
- The Furman-Pivi secondary emission model, originally described by its authors in [16]

Of the two models, the Vaughan one is simpler, being described by just ten parameters (four if standard values provided by Vaughan are used for less critical parameters [7]), while the Furman-Pivi is far more complex as it exploits 45 parameters (as reported in [7] where a comparison between the two different models is provided). Those differences between the two could be summarized by the following observations:

- Both the models describe the secondary emission phenomenon by using what they call a Secondary Electron Yield (SEY) curve, which is the average of secondary emitted electrons per incident electron on the emitting surface; SEY is often indicated in literature with  $\delta$ .
- In both models SEY is a function of the incident electron energy  $W$  and the incidence angle  $\theta$  (defined with respect to the normal to the surface). So it is sometimes described in literature as  $\delta(W, \theta)$ .
- In order to have multipaction (besides from the synchronism of the RF field period with the electron trajectory) if a primary electron strikes a surface with a certain energy  $W$  and incident angle  $\theta$  it must be  $\delta(W, \theta) > 1$ , that is more than one secondary should be emitted for each incident electron.

Leaving from the picture the incidence angle  $\theta$  (supposing normal incidence for example), the energy of the incident electron is decisive in assessing if there will be secondary emission or not. Obviously the SEY is an average parameter. For example a SEY of 0.9 means that for 100 incident electrons only 90 are re-emitted, while 10 will be absorbed from the surface itself; instead, a SEY of 1.2 means that on average on 100 incident electrons 120 will be re-emitted, of which for example 100 could be backscattered and the remaining 20 true secondary electrons (see below for information on this terminology).

- Vaughan model only provides a SEY curve, it does not provide the energy and angular distribution for the secondary emitted electrons [7].
- The Vaughan model is a purely empirical, heuristic model and it models the physical phenomenon by trying to fit the proposed formulas with experimental observation. Instead the Furman-Pivi uses a semi-empirical united to a statistical approach, employing a Monte-Carlo method to describe the secondary emissions.

The Vaughan model is simple. Omitting the discussion which lead to its derivation, which could be consulted in [15], the yield returned by this model has the following trend:

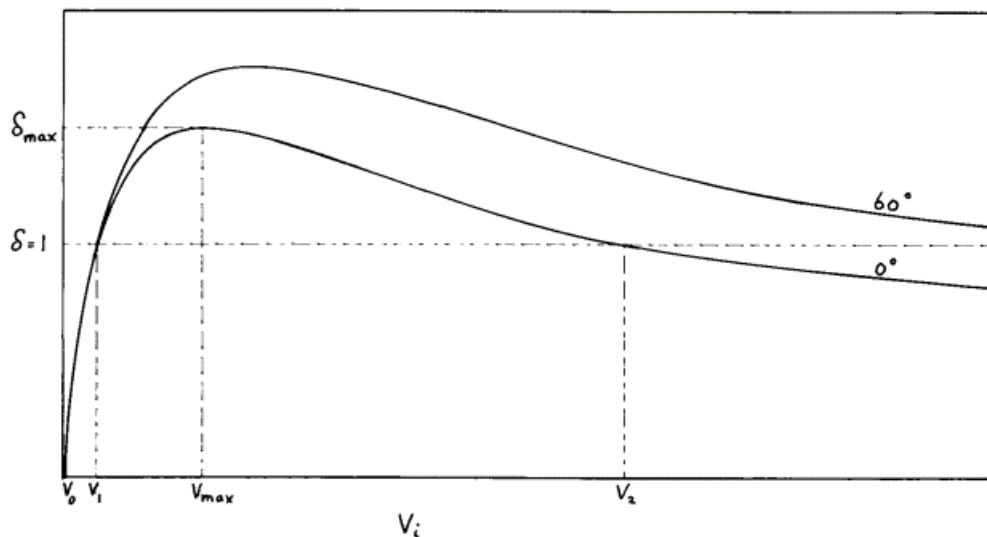


Fig. 2.3 SEY curve of the Vaughan model, for normal incidence ( $\theta=0$ ) and  $\theta=60^\circ$  [15]

On the x-axis is reported the energy of the incident electron (expressed here in Volt instead of eV), while on the y-axis the SEY in correspondence of that particular energy for a certain angle of incidence.

By observing the curve for normal incidence, it can be noticed the presence of a maximum secondary yield  $\delta_{max}$  at incident energy  $V_{max}$ , while at energies  $V_1$ ,  $V_2$  the SEY is unitary: there is not a net secondary emission at those energies.

$V_0$  instead is the threshold for the incident electron energy: below  $V_0$  it is  $\delta=0$ , there is not any emission at all. In Fig. 2.3  $V_0=0V$ , but this value can also be non-null. In this case the SEY curve does not start from the origin.

In the range  $V_1 < V_i < V_2$  the SEY is greater than unity, and this involves a net “gain” of electrons. So in order for the incident electron to produce secondary emission its energy should be in this range.

It is obvious now coming to the following understanding: multipaction can happen only if the two following conditions are meet:

- the transit time which electrons takes to complete a single trajectory is an odd number of times of the half period of the RF signal,  $T/2$ .
- the average SEY on all the surface must be greater than unity [10].

The second statement come from the fact that only if there is a net gain of electrons an exponential growth of the population can happen. The average of the SEY greater than unity over the entire surface means that in some points it could be less than unity, in other points way greater, and this all will depend on the energies and angle of incidence of the incident electrons, but the average on the entire surface is  $\delta>1$ . This could be a criterion for multipaction detection. Moreover, it can be shown that the average SEY on the surface is self-consistent with the SEY of that specific material.

It comes natural to the author to draw a comparison between multipaction and the laser emission phenomenon in laser systems. Both require a resonance condition, provided by a Fabry-Perot cavity in lasers and by the sync between the RF field and electron trajectory in multipaction; and both require a net gain of their own kind of particles (photons for a laser, electrons in the case of multipaction), provided by the mechanism of stimulated emission in laser systems and secondary emission in the case of multipaction.

As an off-topic this can lead us to ask if multipaction besides from being harmful for some devices in the analyzed context can be useful in the design of other kind of devices, for example a device used to generate an electron beam (an electron gun). Indeed, this was the contest in which at first multipaction has been discovered and described by Farnsworth in 1934 [5] [15].

Farnsworth discovered this effect and utilized it not only to successfully build what he called “multipactor tubes” (from which the name of the effect comes from [5]) which provided a mean of amplification of a signal without using the thermionic effect, but also to build the first functional image dissector tube, both described respectively in patents [23] and [24] (Farnsworth is the father of the first all-electronic television system; previous systems consisted of electromechanical parts too).

So even if multipactor is a damaging phenomenon in the context we are studying, it could also be exploited in some ways to build interesting devices.

Coming back to the main topic of discussion, in the Vaughan model in order to define the secondary emission properties of a material it is necessary to define:

- The threshold energy  $W_0$  after which the SEY start to increase. For  $W_i < W_0$ ,  $\delta=0$ ; as  $W_i$  grow above  $W_0$  the SEY will grow too.
- The values  $W_{max}$  and  $\delta_{max}$  that defines respectively the incident energy at which the SEY is maximum and the maximum value of the SEY.
- The values  $W_1, W_2$  that defines the energy range for which  $\delta>1$ .

Once defined those properties at normal incidence, derived from accurate measurements of the physical phenomenon for a certain material, the SEY curve at normal incidence is completely described by the Vaughan model.

To find the SEY at any incidence angle  $\theta$  the following formulas needs to be applied [15][41]:

$$\begin{aligned} W_{max}(\theta) &= W_{max}(0) \left( 1 - \frac{k_s \theta^2}{2\pi} \right) \\ \delta_{max}(\theta) &= \delta_{max}(0) \left( 1 - \frac{k_s \theta^2}{2\pi} \right) \end{aligned} \quad (2.1)$$

which let us to define a SEY curve for each incidence angle by using the Vaughan model (which as “input” requires  $W_{max}$  and  $\delta_{max}$ ).

Here  $-\pi < \theta < \pi$  is the incidence angle,  $W_{max}(0)$  and  $\delta_{max}(0)$  are the values previously defined at normal incidence for which the SEY curve is maximized, and  $k_s$  is the smoothness factor that defines the state of the surface. If no data are provided it is supposed  $k_s = 1$ , which implies a dull surface [15][41].

The Vaughan’s is a very old model, first described in 1989 in [15].

It has been subject of various improvements and minor adjustments, also from its original author, for example in the modern notation energies are expressed in eV instead of Volt.

Another adjustment is the inclusion in the model of the probability density function (PDF) of the secondary emitted electrons, which the author didn’t include in the original model.

In the software that will be used for multipaction simulations in this work, CST Particle Studio, the secondary electrons PDF is assumed to be a gamma distribution when the Vaughan secondary model is used; an example extracted from CST PS and elaborated with matplotlib is showed in the following graph.

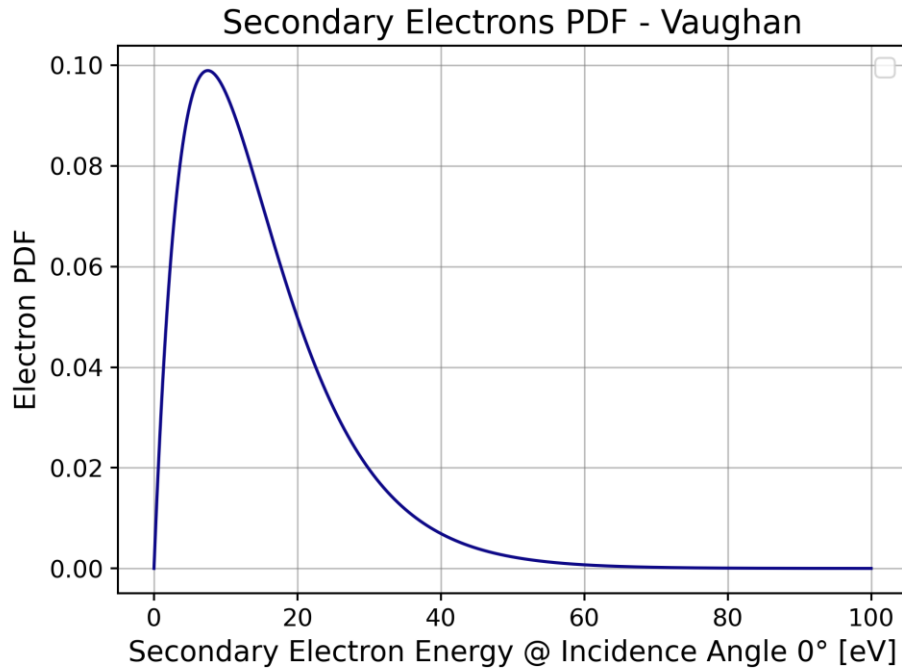


Fig. 2.4 PDF of the secondary emitted electrons in CST Particle Studio for the Vaughan model.

The gamma PDF energy of secondaries is defined in CST Particle Studio by assigning the value of energy (in eV) at which the PDF reach its maximum; the default value of this parameter in CST is 7.5eV.

Moreover, by defining the PDF of secondary emission energies, it is not necessary anymore to define the range  $W_1 \div W_2$  in which the SEY is greater than unity, it is automatically defined from the PDF plus the other parameters of the SEY.

As a full empirical model Vaughan's does not provide insight on the nature of secondary emitted electrons; instead, the Furman-Pivi's subdivide the contribution to the secondary electron yield into three categories, as reported in [7]:

- True secondary electrons, which follow a Maxwell-Boltzmann energy distribution;
- Backscattered electrons, which have the same energy of the incident electron.
- Redifused electrons, which have a uniform energy distribution between 0eV and the energy of the incident electron

The first category of electrons are the “true secondaries” which are really emitted by the surface consequentially to the primary electron hitting the surface; this constitutes the real secondary emission.

The backscattered electrons represent instead the incident electrons that does not penetrate in the metallic surface, and are elastically backscattered by it.

Finally, the redifused electrons are those incident electrons who penetrates a very short length inside the metal, and then are scattered from one or more atom inside the material, and consecutively re-emitted with a certain energy in a range that goes from 0eV to the original energy of the incident electron [16].

The total SEY in the Furman-Pivi model is computed as the sum of each single yield (true secondaries, backscattered, redifused).

Instead, the Vaughan model takes into account only true secondary electrons [41]. This makes the Furman-Pivi model more accurate than Vaughan's.

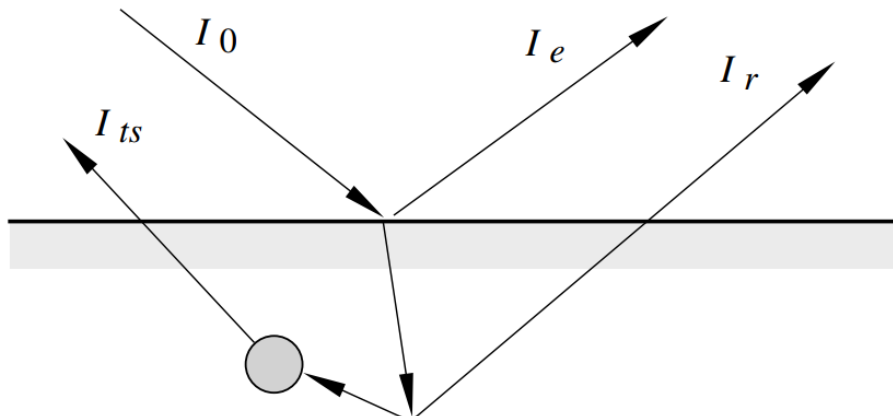


Fig. 2.5 Depiction of the three SEY components in Furman-Pivi model: True Secondaries, backscattered (Elastically scattered), Redifused [16]

In Fig. 2.5 an illustration of the three SEY components in the Furman-Pivi model is provided [16]. Incident electrons are modelled as an incident current  $I_0$ , true secondaries constitute the current  $I_{TS}$ , backscattered electrons make up the current  $I_E$  and finally redifused electrons are modelled by the current  $I_R$ . The total SEY is then defined as [16]:

$$\delta = \frac{I_{TS} + I_E + I_R}{I_0} = \delta_{TS} + \delta_E + \delta_R \quad (2.2)$$

With regard to the emission angle, while true secondary electrons are re-emitted with a  $\cos\theta$  angular distribution (which is a thing widely known in literature relatively to this phenomenon), backscattered and redifused electrons follow a more complicate angular distribution [16].

Another detail relatively to this model is that when there is emission of backscattered or redifused electrons there is not emission of true secondaries; conversely when two or more true secondaries are produced, we do not have any backscattered and redifused electrons [16].

Together the three contributes form the SEY curve, which is given usually as a function of incident electrons energies when they hit the surface with normal incidence ( $\theta = 0$ ). Below the SEY curve for copper is reported, from [16].

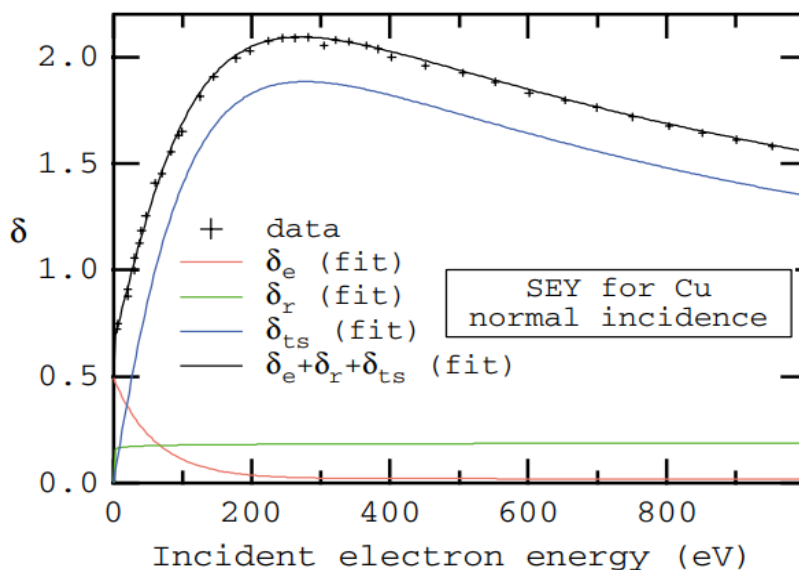


Fig. 2.6 SEY curve for copper, at normal incidence, as function of incident electron energy [16]

As shown in Fig. 2.6, experimental data (measured in [16] from a chemically cleaned sample of copper) are in accordance with the SEY curve derived from the Furman-Pivi model.

Every material has its own SEY curve, which can be modelled with great accuracy (in comparison with real-world data) using the Furman-Pivi model, at condition that the right parameters for setting it up are employed. Obviously Fig. 2.6 refers to normal incidence, but the model is able to give the SEY curve for each incident angle, as the Vaughan's do (though using very different formulas; the complexity of the Furman-Pivi does not allow its description in this brief work, but they can be consulted in [16] and [41]).

Besides from the type of material (as already seen in the Vaughan model) also surface imperfection contributes greatly to the SEY curve. So the state of the surface (roughness, oxidation, aging of the material, etc.) can contribute to some extent in variations in the secondary emission phenomenon, and this cannot be fully accounted for in software simulations. For example, it is difficult in the Vaughan model to adjust the surface smoothness factor  $k_s$  in order to reflect the real condition of a real-world physical surface.

So it is always to keep in mind that simulations of multipaction can give us an estimate of the threshold at which RF breakdown can happen, but physically the real threshold depends on a great variety of factors.

The Furman-Pivi model (which will be employed in the simulations that follows) is very complex, based on 45 parameters like already mentioned (some of them fixed by Furman and Pivi, others dependent on the material); it is not the goal of this thesis to go deeper into its details. However, knowing the basics on how secondary emission is modelled in software using this model will help us later setting properly the simulations.

Besides from the modelling of the physical phenomenon, in multipaction simulations the computational cost of the simulation itself needs to be taken into account. Tracking simultaneously the trajectory of each single electron can have a very high computational cost, leading to very high simulation times.

That is why the majority of software that simulate multipaction (or in some way deal with the secondary emission phenomenon) does not track each single electron; instead, they simulate a group of electrons as a macroparticle (MP) (sometimes called also “effective electrons”) which is a single discrete particle that has a charge equal to an integer multiple of the charge of the electron; in this way the computational cost is lower than the one needed to track each single electron.

This is the approach taken by commercial software like CST Particle Studio and Spark3D [4], but also open-source ones like PyECLLOUD, an open-source solution developed by CERN that models the secondary emission phenomenon by using the Furman-Pivi model (although it does not directly deal with multipaction) [22].

By employing this approach, every time a macroparticle hits a metallic surface it is simply rescaled (increasing its charge by a certain amount if secondary emission is present, or decreasing it if absorption predominates) in agreement with the total SEY corresponding to the incident angle and the energy of the impacting macroparticle [4] [22].

Even if this approach has the advantage of being less computationally intensive than tracking the trajectories of each electron, it does not fully take into account space charge effects (that is the mutual repulsion of electrons), which tend in the long run to disperse a large group of electrons as their number grows.

It can be shown however that space charge effects do not impact too much on the multipaction threshold determined by simulation; the initial stages of multipaction can be simulated without space charge effects, without significant deviation from physical reality [20].

It is only when simulation time grow that space charge effects start to become important, by limiting the exponential growth of electrons in the device; instead, simulating without space charge effects lead to an indefinitely exponential growth of the electron population.

As the main interest in this work is to estimate the multipaction threshold of the devices under study and we are not interested in the time evolution on the phenomenon, space charge effects will be excluded from the simulations, in order to have a reasonable running time (space charge effects largely contribute to the computational cost of the simulation). This is the approach taken from most commercial software focused on multipaction simulation indeed.

CST Particle Studio provides the inclusion of space charge effects just because it is a more general-purpose software which can be used to simulate various physical phenomena involving particles, not only multipaction [4]. Under the simulation settings it provides the option to enable/disable space charge effects; by default, they are enabled, so this setting should be disabled before launching the simulations if we want reasonable computing times.

All the PIC simulations performed in this work have been conducted with space-charge effects disabled.

## 2.2 Multipaction analysis in parallel plates waveguides

Multipaction in parallel plates waveguides has been widely studied in literature; in particular Hatch and Williams [37] provided a model for the prediction of multipaction threshold (expressed as voltage between the gap) in those structures, along with an in-depth study of multipaction of higher order modes.

Indeed as already stated in the previous section multipaction is a resonant phenomenon, and the electron transit time between one plate and the other must be an odd multiple of the half-cycle of the RF signal ( $T/2$ ) in order to have multipaction. This means:

$$t_{transit} = (2n - 1) \frac{T}{2} \quad (2.3)$$

Where  $n=1,2,3\dots$  is the so-called “order” of multipaction. The order not only influence the transit time of the electrons, but also the threshold voltage at which multipaction can happen.

Multipaction of higher order has a threshold voltage lower than the one of low order multipaction modes. So if higher order modes are present (that's not always the case) they are the one responsible for lowering the threshold at which a discharge can happen.

In order to study multipaction in a time where electromagnetic simulations were not available (so neither particle in cell), Hatch and Williams introduced a theory for the study of higher order multipaction modes and derived (fitting data available at the time with their theoretic derivation) what are today known as “Hatch and Williams multipaction susceptibility charts”, which provide a tool still used nowadays for the estimation of multipaction threshold in parallel plates waveguide structures (but also other types of geometries, by means of opportune scaling of some factors) without executing any PIC simulation.

In parallel plates waveguides the multipaction voltage threshold is a function of the  $f \times d$  product, where  $f$  is the frequency of the excitation signal and  $d$  is the distance between the plates. The Hatch and Williams susceptibility charts provide the multipaction threshold as a function of the  $f \times d$  product.

In Fig. 2.7 the original charts obtained by Hatch and Williams in [37] have been reported.

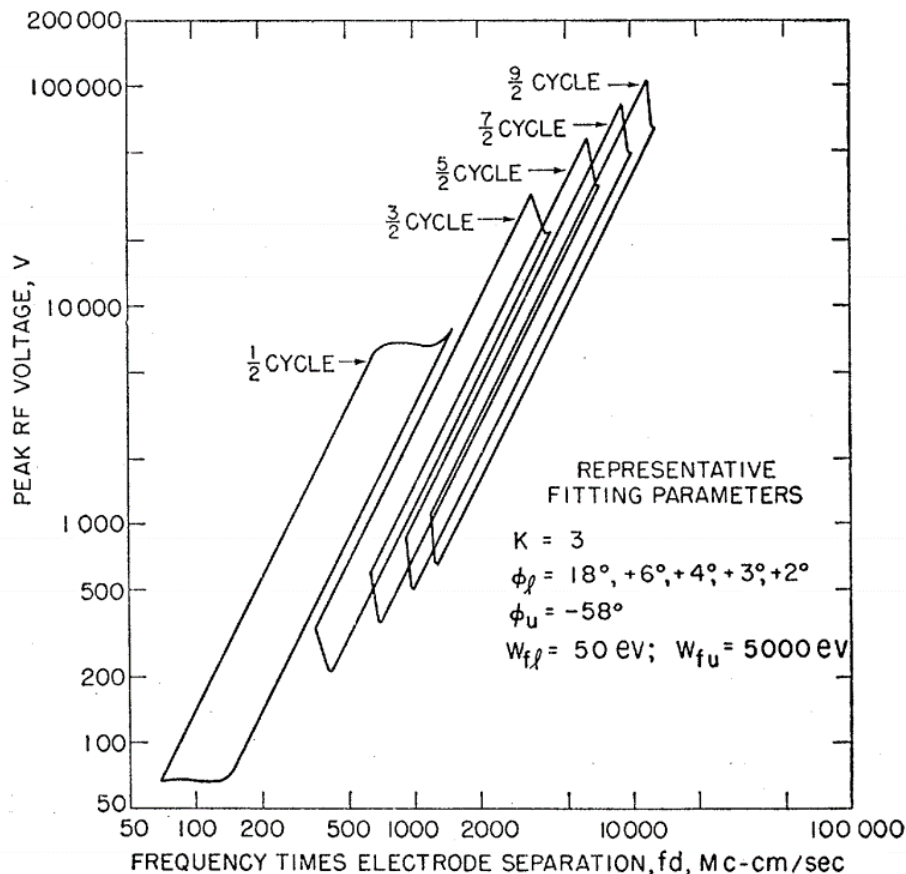


Fig. 2.7 Hatch and Williams multipaction susceptibility charts [37]

This chart provides the threshold voltage (on the y-axis) as a function of the so-called frequency-gap product (on the x-axis).

For each single mode a closed-loop curve is provided: the lower part of the curve describes the onset of multipaction, providing a lower limit to the threshold. This usually should not be surpassed if one wants to avoid multipaction.

The overall area inside each curve instead describes the region in which multipaction is more likely to happen.

The units of the  $f \times d$  product here are provided in MegaCycles $\times$ cm/sec, where MegaCycles per seconds correspond to the modern unit of MHz; nowadays it is more common to express the  $f \times d$  product in GHz $\times$ mm.

In order to use this chart one should simply find the  $f \times d$  value for the structure under analysis (once the working frequency is assigned), draw a vertical line, and see which multipaction modes are excited in the structure by that specific RF signal.

For example for a parallel plates waveguide with  $d=10\text{mm}$  excited by a RF signal of frequency  $f=0.5\text{GHz}$ , the  $f \times d$  product in modern units is  $5\text{GHz} \times \text{mm}$ .

By evaluating the conversion factor from  $\text{Mc} \times \text{cm/sec}$  to  $\text{GHz} \times \text{mm}$  we have:

$$1 \frac{\text{Mc}}{\text{sec}} * \text{cm} = 1\text{MHz} * \text{cm} = 10^{-3}\text{GHz} * 10\text{mm} = 0.01\text{GHz} * \text{mm} \quad (2.4)$$

So  $1\text{Mc} \times \text{cm/sec}$  correspond to  $0.01\text{GHz} \times \text{mm}$ ; which means that  $1\text{GHz} \times \text{mm}$  correspond to  $100\text{Mc} \times \text{cm/sec}$ :

$$1 \text{GHz} * \text{mm} = 100 \frac{\text{Mc}}{\text{sec}} * \text{cm} \quad (2.5)$$

In the case of  $f=0.5\text{GHz}$ ,  $d=10\text{mm}$ ,  $f \times d = 5\text{GHz} \times \text{mm}$ , this means that the frequency-gap product in older units used by Hatch and Williams is  $500\text{Mc} \times \text{cm/sec}$ . By drawing a vertical line in correspondence of this value, it is found that both the second and first order multipaction modes are excited in this case (respectively indicated as  $1/2$  cycle and  $3/2$  cycle curves; those are the transit times of electrons in the case, respectively, of first order and second order multipaction).

Another thing to notice from the Hatch and Williams chart is that each mode has its own cutoff frequency; under a certain value of the frequency-gap product the  $n$  mode cannot be excited. The first mode for example has a cutoff frequency (in term of  $f \times d$  product) of circa  $80\text{Mc} \times \text{cm/sec}$  as reported in [37], which corresponds to  $0.8\text{GHz} \times \text{mm}$ . Under this value, for the material used to plot the charts in figure (which is not explicitly reported in the paper), not even the multipaction mode of first order is excited, and this means that multipaction should not happen at all in this case.

A comprehensive susceptibility chart which reports not only the first order mode but also following ones does not seem to be present in modern literature, at least to the author's knowledge. So even if older units are used on this one, it still provides a good understanding on how various higher-order multipaction modes can be excited basing on the frequency-gap value.

Moreover the Hatch and Williams charts still provides an invaluable tool to approximatively predict the multipaction threshold for various structures and materials without executing any Particle-In-Cell simulation (which is often time consuming).

This is the approach taken by the ECSS (European Cooperation for Space Standardization) multipactor tool provided by ESA (European Space Agency), with information and the software itself available at [38][39][40].

Indeed multipaction can be a problem not only in devices for particle accelerators, but also in RF components for satellites and other space electronics equipment. So many space agencies, ESA included, do a lot of research on this topic.

In the following pages a brief explanation on the use of the ECSS multipactor tool will be provided, along with an example analysis of a parallel plate structure using this software.

Then the same analysis will be executed with CST Particle Studio (the software which will be used in chapter 3 for the analysis of the Riblet short slot coupler) by implementing a PIC simulation on a parallel plates structure with the same dimensions, and a comparison will be made between the two approaches, in order to validate the results obtained with CST PS with the one available in modern literature (which basically are based on the Hatch and William charts).

### 2.2.1 Multipaction analysis of a parallel plates waveguide using the ECSS multipactor tool

As previously stated, the ECSS multipactor tool is a software provided by ESA [38][39][40] used to estimate multipactor threshold without involving any PIC simulation. Its principle is based on the Hatch and William charts for different materials, which in the software have been slightly modified in order to report only the threshold at which multipaction is likely to happen (and not the entire closed-loop curves for each mode). The ECSS Multipactor Tool user manual [42] (along with the help integrated with the software itself) have been used in order to gain proficiency using this tool.

Below is reported the chart used by the software for aluminum.

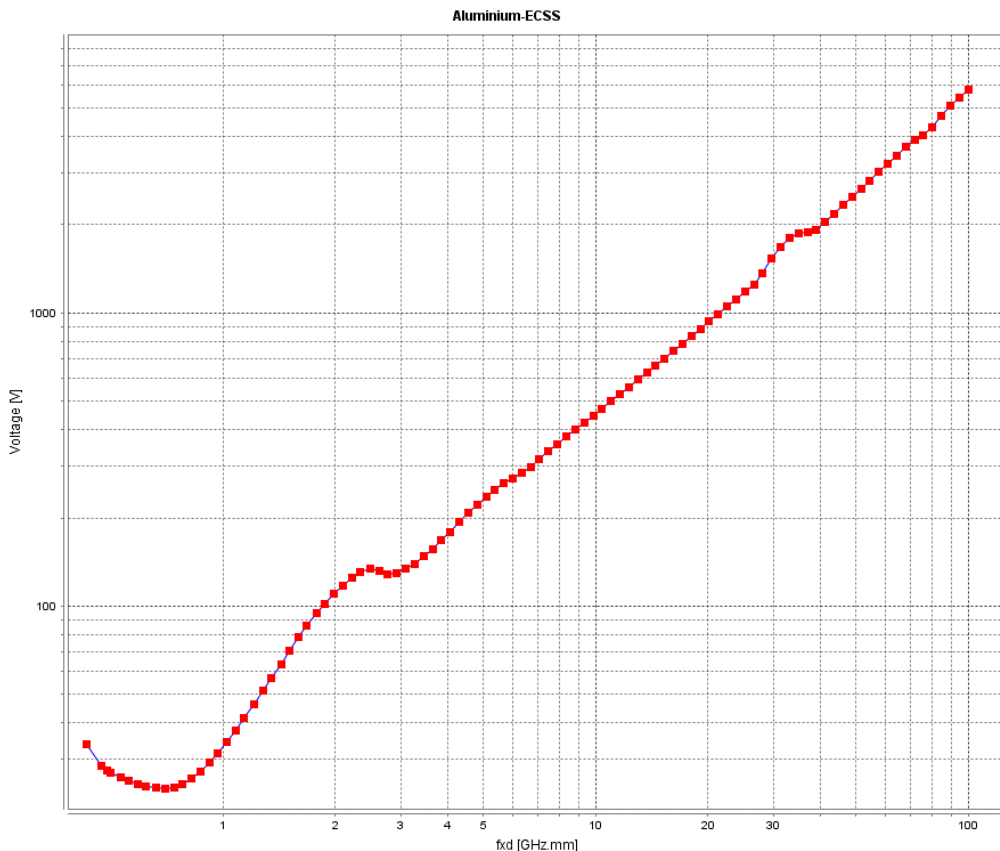


Fig. 2.8 Hatch and Williams chart for aluminum used by ECSS multipactor tool available at [38][39][40].

As in the original Hatch and Williams chart, on the x-axis is reported the frequency-gap product (this time in GHz×mm), and on the y-axis the peak voltage at which multipaction (and thus possibly breakdown) is likely to occur.

The ECSS multipactor tool provides different kind of analysis; in this work it has been used for “single-carrier signal analysis” as specified in the software itself. This kind of analysis let us to find multipaction limits in simple structures like parallel plates or rectangular waveguide when the input is a CW (continuous wave) signal.

In order to estimate the multipaction threshold in CW excitation using the ECSS Multipactor tool some parameters must be defined in the following window of the software:

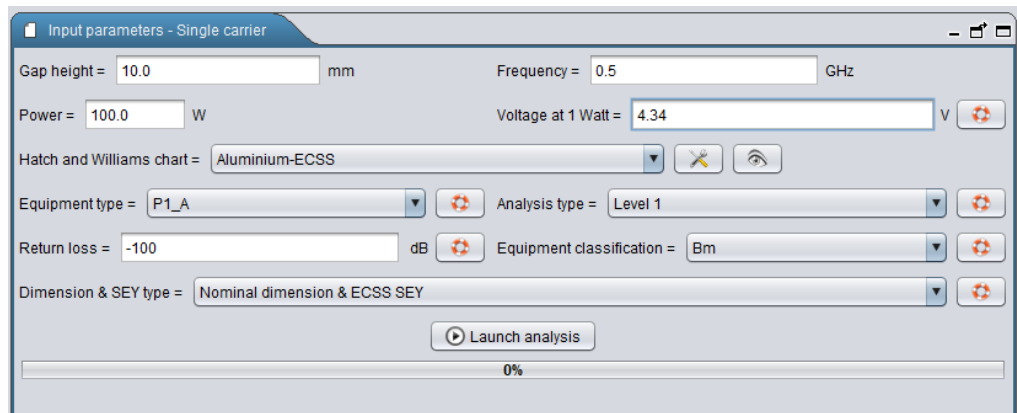


Fig. 2.9 ECSS multipactor tool configuration window [38][39][40].

The gap height, frequency and power parameter are pretty self-explanatory; the power in particular is defined as peak power, in Watt.

The “Hatch and Williams chart” let the user load a particular multipaction susceptibility chart for the kind of material under analysis; at the time of writing the ECSS charts for aluminum, copper, gold and silver are available.

As equipment type instead the “P1\_A” option has been selected, which as indicated in the help of the software it is specific for structure in which there is no presence of dielectrics or ferromagnetic materials in the gap. This is the case in our analysis, since it has been conducted for components under vacuum (which even though is an insulator, is not a dielectric since it does not exhibit polarization and other dielectric related phenomena).

The analysis type must be of “Level P1”, since this is the one indicated in the software help for “P1\_A” equipment type.

The return loss instead specifies the amount of power reflected back to the input port; for a microwave component in which all the ports are closed on matched loads the reflected power should be very small, and thus the return loss very high in absolute value.

For this analysis the return loss has been set to -100dB, a somehow unrealistic value which however let us to consider the power in the device as the power provided only by the input port, with the output port perfectly matched and without any reflection. A higher return loss (for example -10dB) would take into account the total power in the device (input and reflected), and this could be responsible for a lower value of the multipaction threshold, since also the reflected power becomes accountable for the motion of the electrons inside the gap. In this analysis it can be said that the reflected power has been completely set to zero, in order to analyze only the intrinsic limits of the waveguide and not the ones of a hypothetical circuit in which it could have been employed.

Finally, the “Voltage at 1 Watt” parameter is maybe the most important since it let us to analyze various different structures, with different geometries.

The voltage at 1W, from now on indicated as  $V_{1W}$ , is the peak voltage developed across the critical gap of the device (that is between the two plates in case of a parallel plate waveguide) when the input port is excited by a signal with a 1W of peak power.

The  $V_{1W}$  parameter is necessary in the ECSS computation since the value returned by the Hatch and Williams charts is expressed as a peak voltage, and must be somehow converted to peak power by taking into account the geometry of the device itself.

Indeed the manual of the ECSS multipactor tool explicitly says that the relation between the peak power of the electromagnetic wave exciting the structure and the peak voltage between the two plates is given by  $P = kV^2$  [42].

At P=1W the peak voltage between the plates will be  $V_{1W}$ , so:

$$P = kV_{1W}^2 = 1W \quad \rightarrow \quad k = \frac{1W}{V_{1W}^2} \quad (2.6)$$

Numerically the factor  $k$  coincides with the inverse of the square of  $V_{1W}$ . But  $V_{1W}$  is numerically given by the square root of  $Z_0$ ; this means that  $k = 1/Z_0$ , which returns  $P = V^2/Z_0$  as known from circuit theory. This means that the  $V_{1W}$  parameter is just another way to model the characteristic impedance of the device.

If the threshold voltage at which multipaction happens is known by the Hatch and Williams charts, the corresponding peak power threshold is given by:

$$P_{th} = kV_{th}^2 = \frac{1W}{V_{1W}^2} V_{th}^2 = \frac{V_{th}^2}{V_{1W}^2} * 1W \quad (2.7)$$

In this way the  $V_{1W}$  parameter makes possible the conversion between peak voltages and peak powers, generalizing this concept for all the kind of structures (not only parallel plates waveguide). Indeed by assuming a uniform electric field in some region of the device one could compute the  $V_{1W}$  parameter by means of electromagnetic simulations, execute the multipaction threshold analysis with the ECSS multipactor tool, and obtain the peak input power at which multipaction can happen in that particular region of the device. The ECSS multipactor tool uses the  $V_{1W}$  provided value in order to make an automatic conversion between peak voltages and peak input powers, so the value of the threshold will be automatically expressed as a peak power once the  $V_{1W}$  value has been assigned. So in order to estimate the multipaction threshold of a parallel plate waveguide with the ECSS tool, it is necessary to know the value of the  $V_{1W}$  for the structure under analysis. In Fig. 2.10 a schematic representation of a parallel plate waveguide is provided.

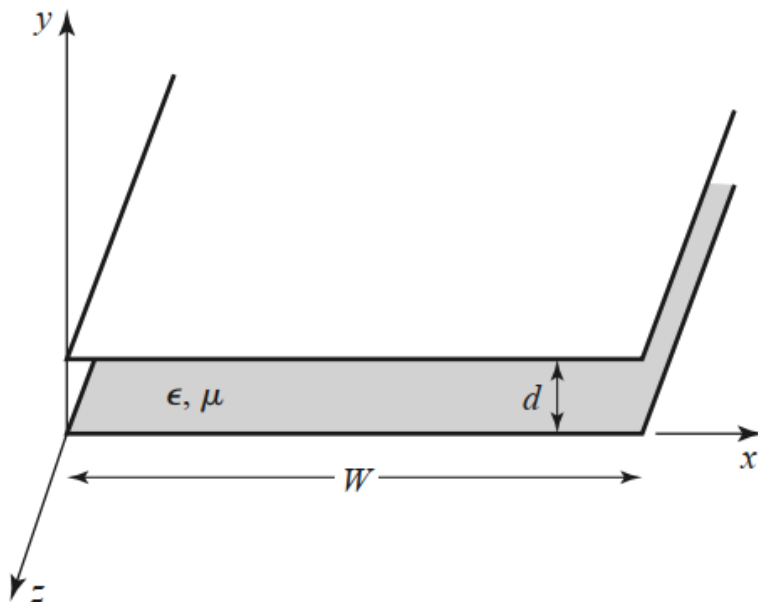


Fig. 2.10 Parallel plates waveguide representation [1].

It will be considered the case in which the only mode excited in the structure is the TEM mode, which means that the frequency of the signal which provides the excitation is lower than the cutoff frequency of the TE<sub>1</sub> mode of the structure:

$$f < f_{c_{TE1}} = \frac{c}{2d} \quad (2.8)$$

In this case, by neglecting fringing effects at the edges of the two plates, inside the gap the electric field is transversal to the two plates, while the magnetic field is parallel, as shown in the following picture by electric and magnetic field lines.

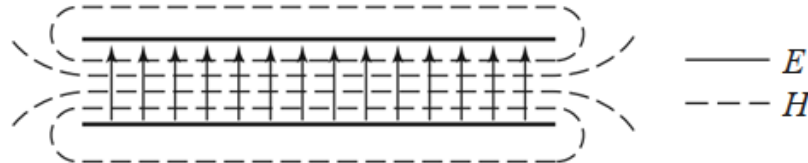


Fig. 2.11 E, H field lines in parallel plate waveguide [1]

In this case (TEM mode) the electric and magnetic field inside the gap assume the expressions [1]:

$$\begin{aligned} E &= -\frac{V_0}{d} e^{-jkz} \hat{u}_y \\ H &= \frac{V_0}{\eta d} e^{-jkz} \hat{u}_x \end{aligned} \quad (2.9)$$

where V<sub>0</sub> is the peak voltage between the plates; d their distance; k the propagation constant;  $\hat{u}_x$ ,  $\hat{u}_y$  the unit vectors and  $\eta$  the wave impedance of the material between the gap (in Ohm). For vacuum the wave impedance coincide to the impedance of free space, whose value is given by:

$$\eta = \sqrt{\mu_0/\epsilon_0} \approx 376,73 \Omega \quad (2.10)$$

which is often rounded to 377Ω.

Now the overall peak power in the cross-section  $W, d$  of the gap can be computed by integrating the Poynting vector over the surface of area  $W \times d$ . By applying 2.7 to the computation of the peak power:

$$\begin{aligned} P_{peak} &= Re \int_{x=0}^{x=W} \int_{y=0}^{y=d} (\vec{E} \times \vec{H}^*) \cdot \hat{\mathbf{u}}_z dy dx = \\ &= Re \int_0^W \int_0^d \left( \frac{V_0}{d} e^{-jkz} \frac{V_0^*}{\eta d} e^{+jkz} \right) dy dx = \\ &= Re \int_0^W \int_0^d \left( \frac{|V_0|^2}{\eta d^2} \right) dy dx = Re \left( \frac{|V_0|^2}{\eta d^2} W d \right) = \frac{W}{\eta d} |V_0|^2 \end{aligned} \quad (2.11)$$

2.12 gives the peak power across a generic section  $W, d$  of the parallel plates structure when it is excited by a peak voltage  $V_0$  (or conversely it can give the peak voltage  $V_0$  between the plates when the structure is excited with a signal providing 1W of peak power). The relation can also be expressed as:

$$P_{peak} = \frac{|V_0|^2}{\eta d / W} = \frac{|V_0|^2}{Z_0} \quad (2.12)$$

where  $Z_0 = \eta d / W$  is the wave impedance of the TEM mode inside the structure. Usually the average power is taken into consideration when computing the power which pass through a certain section of a microwave circuit; however the definition of  $V_{1W}$  as used by the ECSS multipactor tool requires the computation of the peak voltage between the plates when the input power has a peak value of 1W. In this case, from 2.12 and 2.13 the  $V_{1W}$  of a parallel plate waveguide of width  $W$  and distance between the plates  $d$  can be computed as:

$$V_{1W} = |V_0| \Bigg|_{P_{peak} = 1W} = \sqrt{P_{peak} Z_0} \Bigg|_{P_{peak} = 1W} = \sqrt{\frac{\eta d}{W}} \quad (2.13)$$

So the  $V_{1W}$  is simply given (numerically) by the square root of the characteristic impedance  $Z_0$ ; in case of parallel plates waveguide in which there is only TEM propagation  $V_{1W}$  is given by 2.14.

We can now perform an analysis on a parallel plate waveguide using the ECSS multipactor tool; the values obtained for the multipaction threshold will be then confronted in the next section with the ones obtained with a full particle-in-cell simulation executed by using the software CST Particle Studio on a structure with the same geometry and dimensions.

We decided to analyze a vacuum-filled parallel plate waveguide with dimensions  $W=200\text{mm}$ ,  $d=10\text{mm}$ . In this case the cutoff frequency of the  $\text{TE}_1$  mode is given by:

$$f_{c_{\text{TE}1}} = \frac{c}{2d} \approx \frac{3 * 10^8 \frac{\text{m}}{\text{s}}}{2 * 10 * 10^{-3}} = 15 \text{ GHz} \quad (2.14)$$

To excite only the TEM mode, an excitation signal with a frequency of less than 15GHz must be provided.

The  $V_{1W}$  parameter for this type of structure has the following value:

$$V_{1W} = \sqrt{\frac{\eta d}{W}} \approx \sqrt{\frac{377\Omega * 10\text{mm}}{200 \text{ mm}} * 1\text{W}} \approx 4,34\text{V} \quad (2.15)$$

The parameters of the structure under analysis are summarized in the Table 2.1

Tab. 2.2 Parallel plates waveguide under analysis in the ECSS Multipactor Tool (ESA).

Parameter	Value	Description
$W$	200 mm	Width of each plate [mm]
$d$	10 mm	Distance between the plates of the structure [mm]
$V_{1W}$	4,34 V	Voltage at 1W [V]
$f$	$0.5 - 0.7 - 1 - 2$ GHz	Frequencies of the excitation signals
<i>Material</i>	Aluminum (ECSS)	Material which constitutes the two plates

The structure under analysis has a fixed geometry, as reported in Tab. 2.1; three frequencies (0.5GHz, 1GHz, 2GHz) of the excitation signal has been tested, in order to test the software for different values of the frequency-gap product. Those frequencies have been chosen in order to not excite any TE or TM mode; only TEM modes are present in this analysis. Under those assumptions, the multipaction thresholds provided by the ECSS Multipactor Tool for each frequency are reported in Table 2.3.

Tab. 2.4 Multipaction thresholds estimated by the ECSS multipactor tool, using the Hatch and Williams curves, for a parallel plate waveguide made of aluminum plates with W=200mm, d=10mm

<b>Frequency <math>f \cdot d</math> [GHz]</b>	<b>Multipaction threshold [V]</b>	<b>Multipaction threshold [W]</b>	
		<b>Peak</b>	<b>Average (RMS)</b>
0,5 GHz	5 GHz × mm	232 V	2860 W
0,7 GHz	7 GHz × mm	314 V	5233 W
1 GHz	10 GHz × mm	453 V	10892 W
2 GHz	20 GHz × mm	925 V	45442 W

As the frequency-gap product increase, so does the threshold at which multipaction happen. The software provides the threshold in terms of peak power at the input; it has been also reported as RMS (average) power since the setup organized using the CST Particle Studio software with which we are going to execute the particle-in-cell analysis for the multipaction threshold detection express the same results as average (RMS) levels.

In Fig. 2.12 the chart generated by the ECSS multipactor tool is reported for the structure under analysis and for an excitation frequency of 1GHz. In particular, the green/red vertical line is positioned in correspondence of the frequency-gap product ( $f \cdot d = 10\text{GHz} \times \text{mm}$  in Fig. 2.12); the violet line is obtained from the Hatch and Williams chart for that particular value of the frequency-gap product, and it indicates the level at which multipaction breakdown is likely to happen. The black horizontal line constitutes the ECSS limit, which should not be surpassed in order for the device to be compliant with ECSS directive; finally the blue horizontal line represent the peak power level at input expressed as a peak voltage. The device is operating out of multipaction levels if the blue line is in the green zone, which means under the black line.

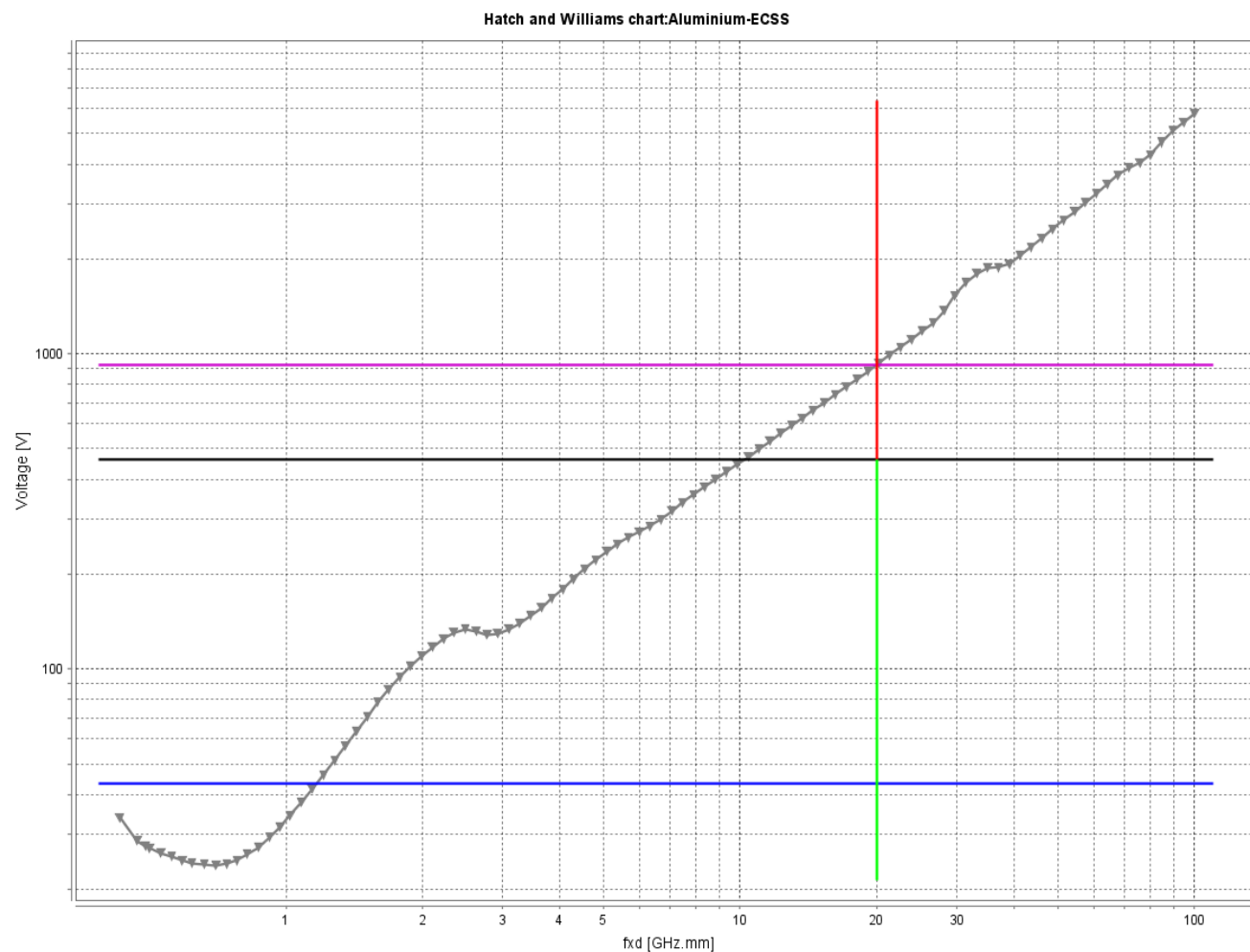


Fig. 2.12 Parallel plates multipaction threshold analysis with ECSS multipactor tool;  $f \times d = 10\text{GHz} \times \text{mm}$

### 2.2.2 Parallel plates waveguide multipaction analysis by using CST Particle Studio

In this section the analysis of the multipaction effect for parallel plates waveguide will be executed by simulating this phenomenon in CST Particle Studio, a software which implements amongst the other things a PIC solver (Particle In Cell) that let the user track the motion of each charged particle under the influence of an electromagnetic field.

The PIC simulations employed in this work have been executed by following the procedures presented in [4], [19] and [20]; those works provide an accurate description of the setup in CST-PS of a particle-in-cell simulation for the detection of multipaction threshold.

Indeed by employing the PIC algorithm and one of the available secondary emission models (Vaughan or Furman-Pivi; the last one has been chosen for this work) multipaction can be simulated and detected by using this software.

The goal is to extract the multipaction threshold (expressed as average power) for a parallel plate waveguide having the same geometry (and constituted by the same material) of the one analyzed in the previous subsection with the ECSS multipactor tool, and make a comparison between the results returned by both.

It is expected higher accuracy for the CST PS results (even though we have not at the time of writing a way of verify this with an experimental setup), since in this case a full PIC simulation is employed, while the ECSS multipactor tool just estimate the threshold by using available experimental data (Hatch and Williams charts).

In order to execute the simulation, a parallel plate waveguide structure with aluminum plates, width 200mm and distance between the plates of 10mm has been modeled in CST PS. The background material is vacuum, since multipaction analysis must be performed under vacuum conditions. As described in [20] (which provides a similar analysis) the lateral walls of the structure have been enclosed by magnetic boundaries conditions (blue), while all the others by electric boundaries (green). The two red sections instead represent the input ports.

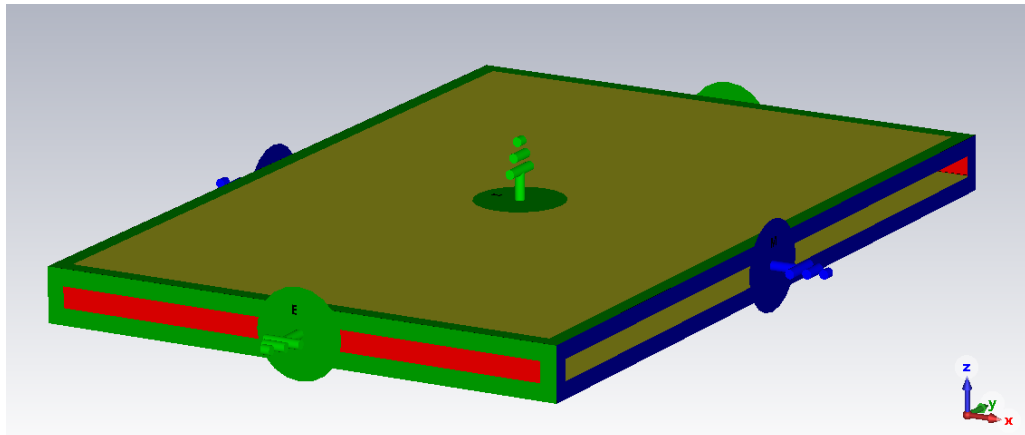


Fig. 2.13 Boundary conditions imposed on the structure

After that the setup of the Furman-Pivi secondary emission model has been executed for the material of which the structure is composed; specifically secondary emissions can be enabled in CST PS by double clicking on the material (aluminum in this case), selecting the “Particles” tab, selecting from “Property” the voice “Secondary Emission” and setting in the “Secondary Emission Model” voice the selected model for secondary emission, Vaughan or Furman-Pivi. All the other values have been left unchanged, since CST Particle Studio automatically loads all the parameters needed in order to describe the secondary emission model of choice for that specific material.

In this way when electrons will hit the upper or lower plate of the device, secondary electrons will be emitted accordingly with the secondary emission model.

Another step that must be executed in order to perform a multipaction analysis with CST PS is the creation of a new excitation signal: indeed the default signal (a gaussian pulse) which contains all the frequencies in the range of the bandwidth selected in the “Frequency” setting is not suitable for detecting the multipaction threshold for a CW excitation, since the power of the signal is distributed among the various harmonic components of its spectrum.

This would lead to a large number of multipacting modes, due to the fact that each harmonic component can be responsible for a different set of modes, making the analysis useless since it would be impossible in this case to determine which component of the spectrum is the one responsible for multipaction; if the multipaction analysis relative to a CW excitation is required (like in this case) the information cannot be extracted from a simulation performed by using a wide-band signal.

So a sinusoidal excitation signal must be provided [20], the duration of which determines the runtime of the simulation. For example for a sinusoidal excitation signal of 50ns, the PIC simulation will be executed for a 50ns time interval, tracking the trajectory of each effective electron in this time frame.

Obviously the duration of the signal must be way greater than the RF period, in order to provide a very large number of RF cycles, since multipaction can be undetectable if the whole simulation consist of a small number of them.

It must be noticed that the particle-in-cell is a time-domain simulation [4]; this makes it a computationally intensive task, since not only the time evolution of the electromagnetic field must be computed, but also the trajectory of each effective electron. The higher the simulation runtime (that is the duration of the excitation signal), the higher will be the time required in order to execute the simulation.

After the electromagnetic power input source has been defined for the structure, a particle source that generates the primary electrons must be defined too.

In PIC simulations indeed there are always two kinds of sources: at least one for the electromagnetic excitation at the input, and one for the emitted particles. Even though they model two sources of a different nature, it can be said that those two constitute the input of the PIC simulation.

In order to launch the primary electrons inside the inner volume of the structure, a “Particle Area Source” has been defined: this procedure in CST PS let the user define an area from which the particles will be launched, with a certain energy or speed distribution. In particular in this structure the bottom plate has been chosen as the emission area for primary electrons, to which a uniform energy distribution in the range 0÷4eV has been assigned as in [19].

The user can also control how many emission points on the surface will be present, and the type of emission model. For this work a gaussian pulse emission in time has been chosen, as suggested in [20].

In particular, each emission point (28 of them have been defined in Fig. 2.14) emits what CST PS call “bounce”, which basically is a single shoot of a certain number of electrons in time; the software let the user choose how many bounces must be fired, the time interval between each bounce and their duration, and also the time offset at which the first bounce is emitted (with respect to the time at which the PIC simulation is started) [41].

The parameter  $\sigma$ , which is the standard deviation of the gaussian distribution (although not a statistical parameter in this case it let the user define the characteristics of the gaussian pulse), is directly responsible for the number of electrons emitted by each bounce (even if this value is not directly controlled by the user).

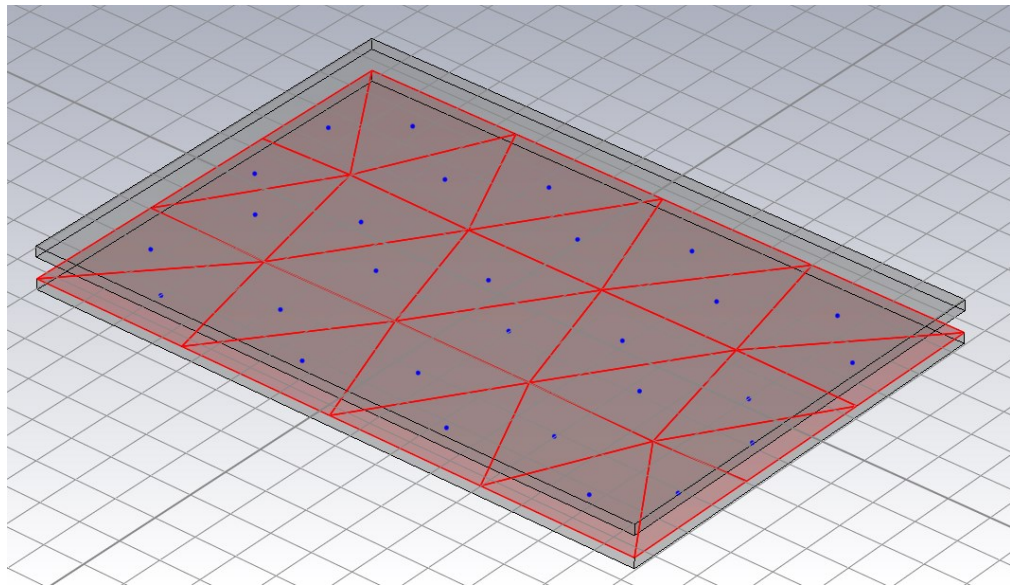


Fig. 2.14 Primary electrons emission points on the bottom surface.

In Fig. 2.14 it is shown the particle area source defined on the upper surface of the bottom plate of the structure; the blue dots are the emission points, while the red triangles represent the spatial subdomains in which the surface is divided. Indeed the gaussian emission can be also defined with respect to space rather than time [41]; in this work a gaussian emission in time has been chosen, since in literature is suggested that in order to perform a physically consistent multipaction simulation that takes into account every possible multipaction trajectory it is necessary to spread the emission of the primary electrons over different phases of the electromagnetic field inside the structure (that means over different times) [20].

In this simulation a single bounce has been emitted, with a half-duration of the gaussian pulse of 3.0 ns (this parameter is called in CST PS “cutoff length”; this means that the entire bounce has a duration of 6.0ns), an offset of 3.0ns (the peak of the gaussian pulse is after 3.0ns from the start of the simulation) and a standard deviation  $\sigma=1.0\text{ns}$ . This ensures that the electrons are uniformly distributed across different phases of the electromagnetic field as suggested in [20].

This last parameter ( $\sigma$ ) has been found in simulations to directly control the number of electrons launched by each emission point, even though it is not specified in the software's manual the specific relation between  $\sigma$  and the number of emitted particles.

The final step required to perform the simulation is the creation of a PIC position monitor which let the user track the particles in the device; in particular for this kind of simulation we are interested in the number of electrons inside the device, and this information is generated by the PIC position monitor.

If multipaction is present, at a certain time the electronic avalanche will become visible, with the number of electrons exponentially growing in time. This is the criterion used for multipaction detection in PIC simulations and it goes under the name of trend analysis [4]: basically it consists on the analysis of the curves “number of electrons vs time” for different levels of input power.

In order to detect multipaction with this method, a quantitative detection criterion could be chosen. For example for a specific power level the device could be considered multipaction-free when the number of electrons decay and reaches 10% of its initial value, while the presence of multipaction could be confirmed when it doubles [4].

A strict quantitative criterion however is not strictly required, since it is always visible if multipaction is present. The only thing one must ensure is that a curve that does not seem to go under multipaction across short simulation times start multipacting if a longer runtime is chosen.

This requirement of high simulation times in order to ensure that a decaying curve does not start growing exponentially after a certain time is in contrast with the increase of computation time if the duration of the simulation is prolonged; the approach used in this work in order to find a tradeoff between those two is the following:

- At first, execute simulations with a low runtime (even around 50ns if the excitation signal is in the order of 0.5-10GHz) and high levels of input power. In this way the power levels at which multipaction happens for sure can be excluded, and a successive simulation with lower levels of input power can be performed.

Simulations with high level of input power indeed are the most expansive (computationally speaking), since they generate a big number of secondary electrons, which somehow must be tracked by the PIC solver.

- After the exclusion of higher input powers from the set of candidate threshold levels, simulations progressively employing a higher runtime and a lower level of input powers can be performed until a level at which multipaction does not happen for sure is found (that means for example that the electron population in the device reaches a level below 10% of its initial value). The last power level for which multipaction happens before not happening at all will be the multipaction threshold of that device.

If the range in which the multipaction threshold is supposed to be found is mostly unknown or is however very large, some attempts must be made at first in order to determine an initial value of power levels at which the device must first be tested; this is the approach taken in chapter 3 for the derivation of the multipaction threshold level of the Riblet short slot coupler under analysis.

If however a first indication of the threshold level is already provided by a first analysis, as in the case of the parallel plates waveguide for which an approximate threshold has already be found in the previous subsection by using the ECSS multipactor tool, the threshold-seeking operations could start from there, and this approach will greatly reduce the number of simulations (and thus time) required in order to find the multipaction threshold.

In the next pages the plots “number of particles vs time” obtained by executing with CST PS the PIC simulations on the parallel plates waveguide under analysis have been reported. The job here has been simple, since as first higher-power level an initial value of less than 10% than the one provided by the ECSS multipactor tool has been used; indeed in all the four cases analyzed (for various frequencies, reported in Tab. 2.2) the structure under analysis showed in CST PS a multipaction threshold around -10% of the value determined with the ECSS multipactor tool, while power levels under -30% of this value showed no detectable multipaction. This is a good agreement between the two analyses, which shows how the CST PS software is suitable for the detection of the multipaction threshold in RF devices.

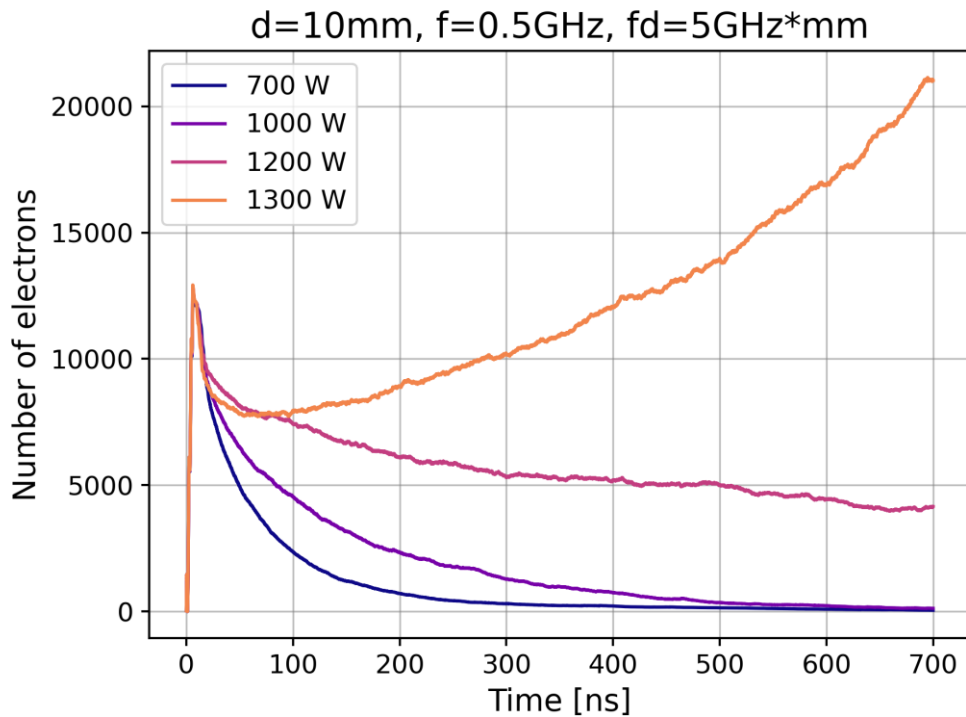


Fig. 2.15 Parallel plates multipaction analysis,  $d=10\text{mm}$ ,  $f=0.5\text{GHz}$ . Multipaction at 1300W RMS

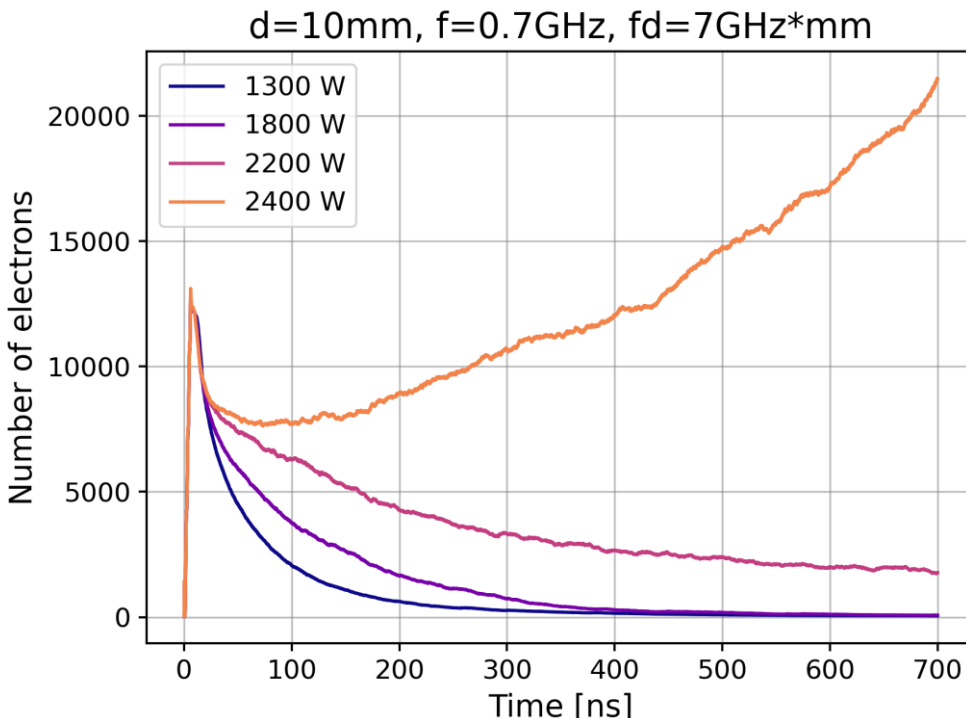


Fig. 2.16 Parallel plates multipaction analysis,  $d=10\text{mm}$ ,  $f=0.7\text{GHz}$ . Multipaction at 2400W RMS

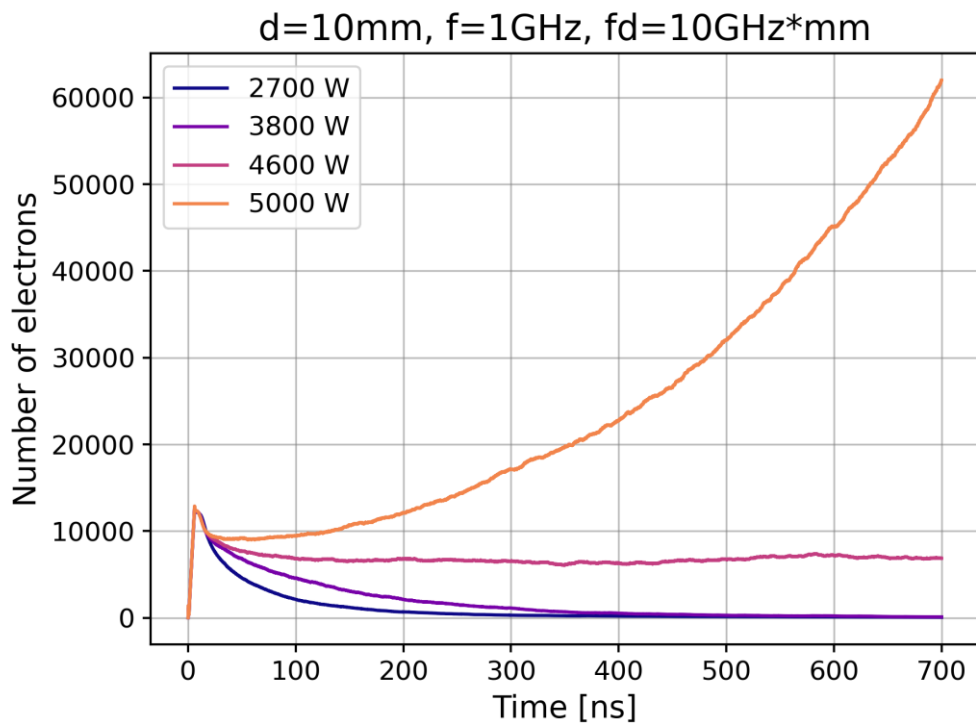


Fig. 2.17 Parallel plates multipaction analysis,  $d=10\text{mm}$ ,  $f=1\text{GHz}$ . Multipaction at 5000W RMS

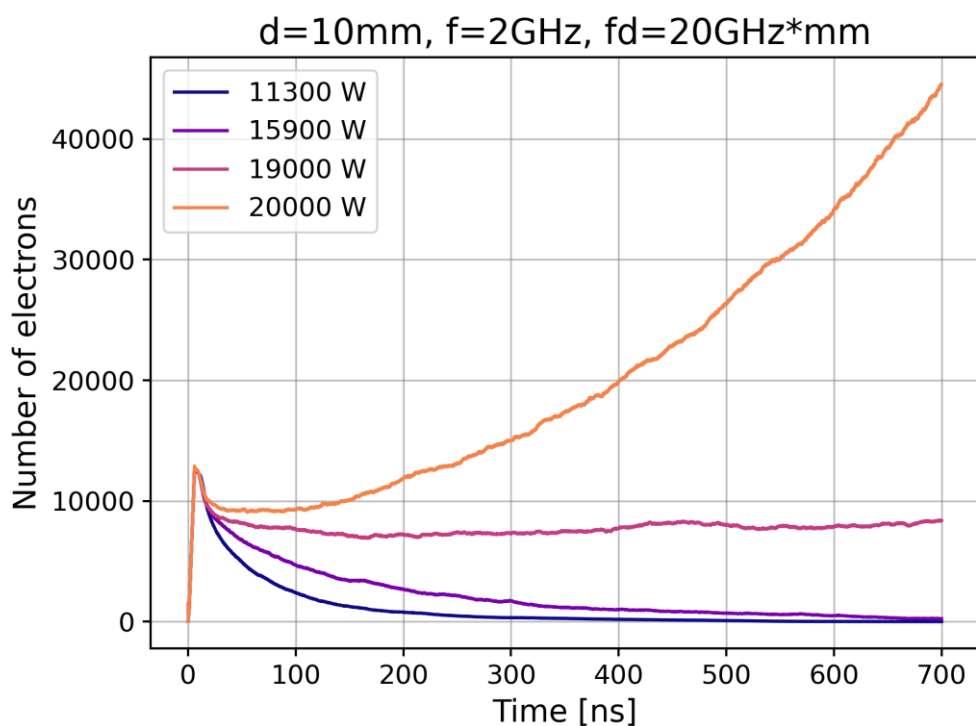


Fig. 2.18 Parallel plates multipaction analysis,  $d=10\text{mm}$ ,  $f=2\text{GHz}$ . Multipaction at 20000W RMS

The goal of the analysis performed on those structures wasn't to find the exact power threshold at which multipaction happens (for example at  $f=2\text{GHz}$  the number of electrons stays almost constants at 19kW RMS; maybe for longer simulations time that curve could start multipacting, and multipaction threshold must then be fixed at 19kW, not 20kW as shown).

The real goal instead here was to show in synthesis the agreement between the ECSS results and the CST PS ones.

A comparison between them is reported in the table below. All the results refer to the same structure, a parallel plate waveguide of aluminum with  $d=10\text{mm}$ ,  $W=200\text{mm}$ , for different frequencies of operation.

Tab. 2.3 Comparison between ECSS multipactor tool and CST PS results.

<b>Frequency</b>	$f \times d$ [GHz]	<b>Multipaction threshold power levels (RMS)</b> [W]	
		<b>ECSS Multipactor tool</b>	<b>CST Particle Studio</b>
0,5 GHz	5 GHz × mm	1430 W	1300 W
0,7 GHz	7 GHz × mm	2616,5 W	2400 W
1 GHz	10 GHz × mm	5446 W	5000 W
2 GHz	20 GHz × mm	22721 W	20000 W

As previously stated, CST PS found that multipaction happens already at levels almost 10% lower than the one proposed by the ECSS multipactor tool.

That's the reason why ECSS directive suggest to always operate at a power level much lower than the threshold detected by the tool (the device should always operate at a power level which correspond under the black horizontal line in Fig. 2.12 in order to operate under a certain safety range.)

Even though results provided by ECSS are not perfect, they already are a first indication of the range in which the multipaction thresholds can be found, so they can be the foundation of a preliminary analysis that could be executed before employing a PIC simulation.

## 3 Riblet short-slot coupler analysis

---

This chapter presents an in-depth analysis of a S-band Riblet short slot coupler employed in the RF power distribution system of the LINAC under construction at Linearbeam (Ruvo).

In particular in section 3.1 the various RF measurements executed on the physical device by means of a VNA (Vector Network Analyzer) will be illustrated.

By characterizing the device using the measures obtained with the VNA and extracting other information by means of geometric measurements executed on the device by using a micrometer and a caliper, an equivalent model of the device itself has been designed in CST Microwave Studio, in which it has been possible the extraction of the simulated S-parameters of the modelled device, in order to compare them with real-world S-parameters of the physical device obtained with the VNA. This analysis is reported in section 3.2.

In this way it has been ensured that (at least at the frequency of interest) the electromagnetic field inside the coupling section of the simulated device is somehow similar to the one present in the physical device, for the same level of input power.

Finally in section 3.3 the multipaction threshold analysis is executed for the device modeled with CST MWS, by converting the file into a CST-PS project and executing an analysis similar to the one described in chapter 2 for the parallel plate waveguide.

### 3.1 VNA calibration and S-parameters measurements

In order to characterize the device under analysis, its S-parameters have been measured by using a VNA, specifically an Anritsu MS4644B.

The input/output ports of the VNA have been connected to the input ports of the Riblet short slot coupler by employing a set of coaxial cables and three waveguide to coax transitions (one of which has been used to provide a matched load). A rectangular to coaxial waveguide transition basically is a portion of a waveguide in which a metallic element connected to the inner conductor of a coaxial cable is inserted from a slot inside the waveguide itself.

The metallic element, if properly positioned and dimensioned, acts as an antenna: if a sinusoidal excitation with frequency greater than the cutoff frequency of the first mode ( $TE_{10}$ ) is applied to the coaxial cable, a certain number of modes (only the  $TE_{10}$  if the frequency is below the  $TE_{20}/TE_{11}$  cutoff) are excited inside the waveguide itself, leading to a propagating electromagnetic field. Conversely, if a propagating mode is present inside the structure the coaxial connector can act as a receiving antenna; an electromagnetic mode propagating inside the waveguide for example can excite a TEM mode inside the coaxial connector, leading to the presence of an RF signal at the other end of the coaxial cable.

In Fig. 3.1 a rectangular waveguide to coax transition is reported. Notice the dimension of the antenna, which is practically a prolongation of the inner connector of the coaxial cable.

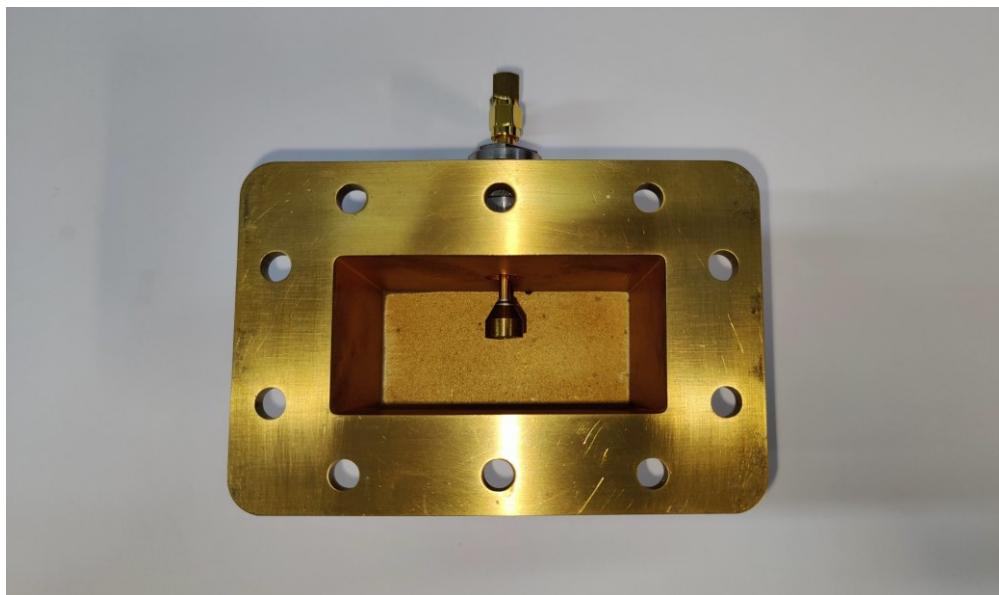


Fig. 3.1 Rectangular waveguide to coaxial transition.

For the calibration of the VNA a SOLT (Short, Open, Load, Thru) calibration has been performed.

In particular a short consist in a transmission line short circuited at its ends, the open conversely is a transmission line with its ends open, the load is usually a resistive element of  $50\Omega$ , and the thru consist in connecting the two input/output ports of the VNA together, by means of a calibrated transmission line if necessary.

In order to account for the actual transfer function (in terms of S-parameters) the SOLT calibration has been executed with the waveguide transitions already attached to the coaxial cables. In Fig. 3.2 the general setup for the SOLT calibration is reported. The coaxial cable of port 1 has been connected to a waveguide transition electromagnetically coupled to a second one.

On the connector of the second waveguide transition in particular, which in this picture is left unconnected, a Short, an Open, a Load and finally a Thru must be attached in sequence, as required by the VNA calibration software

In particular in the Thru procedure the coaxial cable of port 2 of the VNA must be attached to the second waveguide transition using the proper connector. The VNA software in this way can calibrate the reflection coefficients, phase shifts and attenuations due to the coaxial cables and the two waveguide transitions attached to them, and it will not consider those when performing the measurements on the device under test (DUT).

The VNA calibration in practice fixes the reference planes, in this case on the section parallel to the flanges of the waveguide transitions. Therefore, the measures of the S-parameters that one is going to perform after the calibration will not depend on the electrical properties of the transmission line employed for the measurements (constituted in this case by the coaxial cables and the two transitions), but only by the S-parameters of the device under test.

After the calibration, the VNA is ready to perform the measurements. In this case the goal is the measurements of the S-parameters of the device; indeed the VNA can be used for a wide range of measurements, both time domain (reflectometry, as an example) and frequency domain (S-parameters).

Fig. 3.4 report a picture of the device under test, a Riblet short slot coupler, while Fig. 3.5 report the setup used for the measurements of its S-parameters.

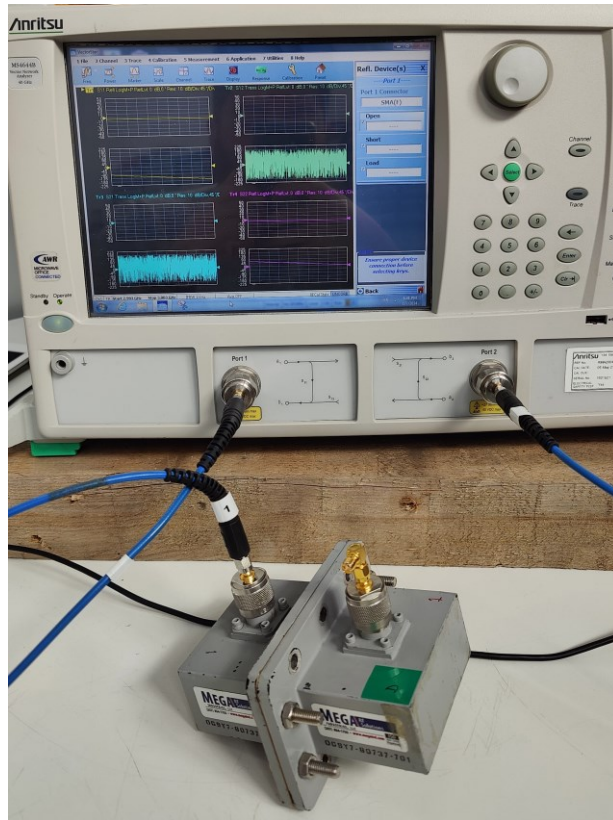


Fig. 3.2 Performing the SOLT calibration (port 2 is still open in this picture).



Fig. 3.3 Performing the Thru step of the SOLT calibration.



Fig. 3.4 The Riblet short slot coupler under analysis.

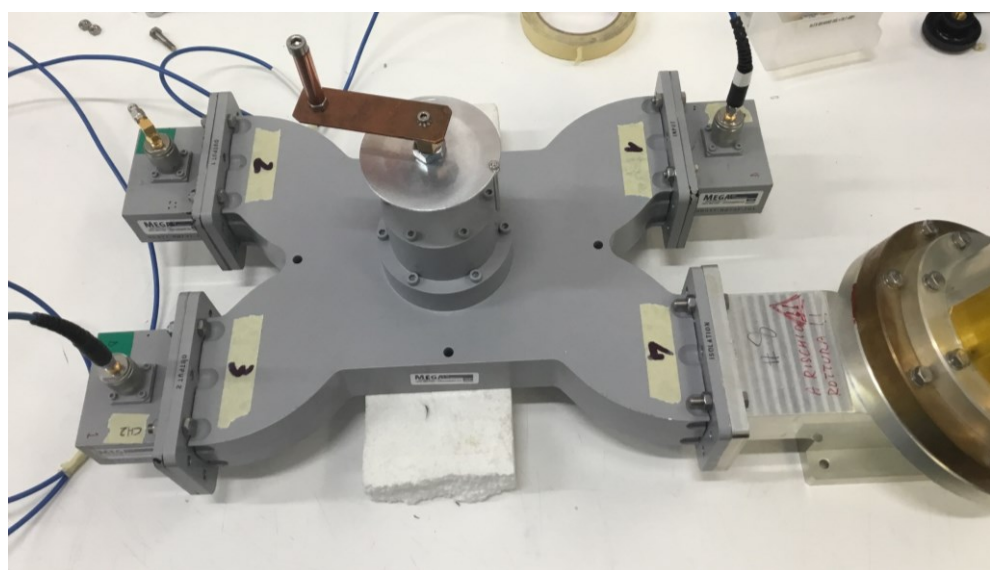


Fig. 3.5 Test bench for the measurements of S-parameters of the DUT

As shown in Fig. 3.2, the VNA at our disposal has only 2 input ports. So in order to perform measurements on a 4-port device, it is necessary to connect the ports of the DUT that needs to be characterized to the two ports of the VNA, while closing the other two free ports on their reference load impedance, in order to minimize reflections.

Indeed, by definition of scattering matrix, a generic  $S_{ij}$  parameter is computed as  $S_{ij} = b_j/a_i$  when all the other ports of the device are closed on their reference impedance.

For example, Fig. 3.5 illustrates the measurement of the  $S_{31}$  parameter; the second port of the VNA is connected to port 3 of the device under test, while its first port to port 1 of the DUT. In this way the reading “ $S_{21}$ ” on the VNA will correspond to the  $S_{31}$  of the Riblet short slot coupler.

By moving the second VNA port to the port 2 and 4 of the DUT (while leaving the first transition to port 1), one can measure respectively  $S_{21}$  and  $S_{41}$ .

It must be noticed that the reconfiguration of the ports has not been done by reconnecting the coaxial cable to a different waveguide transition; indeed both the transitions used for the measurements remained attached to the two coaxial cables of the VNA for the whole time, even when the input/output ports were changed. This is important, since different transitions can have slightly different S-parameters, and by changing the transition attached to the port of the VNA the calibration previously executed could not be valid anymore.

So this approach let us take into account the attenuation and phase shift introduced by the two transition connected to the VNA port, without affecting the measurements.

Notice also in Fig. 3.5 how port 2 and 4 (which are the free ports when measuring the  $S_{31}$ ) have been closed on reference loads; in particular port 4 has been closed on a high-power water-filled load, since we had not at our disposal another waveguide to coax transition. Both the impedances used as loads however have been measured, and they both matched to a value of  $50\Omega$  (the reference impedance chosen for the measurements).

After the calibration and the setup of the whole test bench for the extraction of the  $S_{ij}$  parameters, the measurement operation can take place. In particular in order to characterize the device, the  $S_{11}$  (reflection),  $S_{21}$  (through),  $S_{31}$  (coupled) and  $S_{41}$  (isolation) parameters have been measured.

Since the main goal of this work is to find the multipaction threshold for this device for CW excitation at a single frequency, precisely 2.99792GHz (which is the frequency of operation of the LINAC), the measurements of the S-parameters have been executed at a single frequency (setting up a narrow bandwidth in the configuration of the VNA, from 2.993GHz to 3.003GHz).

Inside the Riblet short slot coupler under analysis is present a capacitive dome with an aluminum cylinder at its center. The cylinder can penetrate for a certain depth inside the body of the coupler, precisely at the center of the coupling section through a screwing mechanism. In this way the effective length of the coupling section is subjected to a variation, and so the power division ratio  $r$ , as illustrated in chapter 1 in the theoretical analysis of this device. The penetration depth of the cylinder inside the coupling section, controlled by a screw system, can be seen in Fig. 3.4 It is used to convert the rotational motion of the screw to a linear motion of the cylinder. Fig. 3.5 is shown a customized version, which let us to control the number of turns imposed on the screw system. By measuring the maximum penetration depth of the cylinder inside the body (which resulted in 18.72 mm) and dividing this for the overall number of turns (12 turns), the progression of the cylinder inside the body for a single turn (or step) of the screw system has been obtained:

$$\Delta = \frac{\text{max. depth}}{\# \text{ turns}} = \frac{18.72 \text{ mm}}{12 \text{ turns}} = 1.56 \text{ mm} \quad (3.1)$$

The number of turns will be used to parametrize the penetration depth of the cylinder, both in the VNA measurements and in the simulations.

In Fig. 3.6 a detail of the inner structure of this device has been reported. The picture has been shot from the inside of one of the four ports. The cylinder is clearly visible.

After the initial calibration and the setup of the testbench, the measurements of the  $S_{11}$ ,  $S_{21}$ ,  $S_{31}$ ,  $S_{41}$  parameters have been performed. In Fig. 3.7 as an example the screen of the VNA software interface is reported; this particular illustration refers to the measurement of the  $S_{21}$  parameter, when the “cylinder\_step” (the name assigned to the parameter that control the cylinder depth) is set to 5 (so the penetration depth of the cylinder inside the structure is  $P_D = 5 \times 1.56 \text{ mm} = 7.8 \text{ mm}$ ).

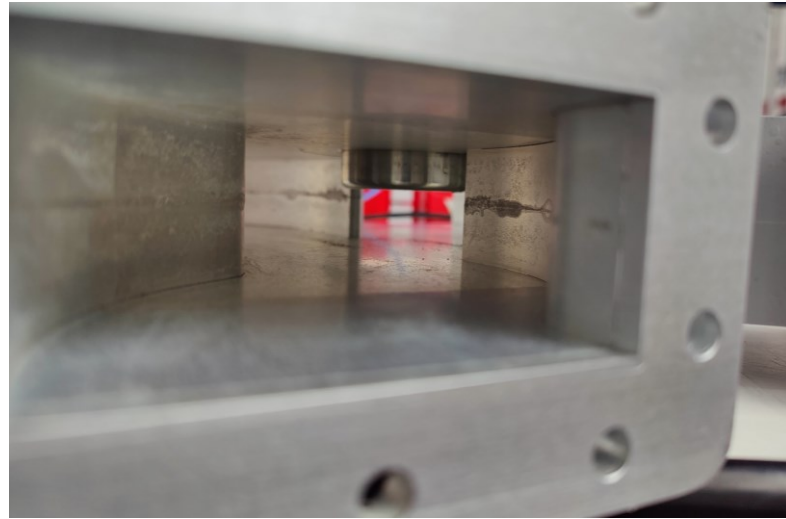


Fig. 3.6 Detail of the cylinder inside the coupling section

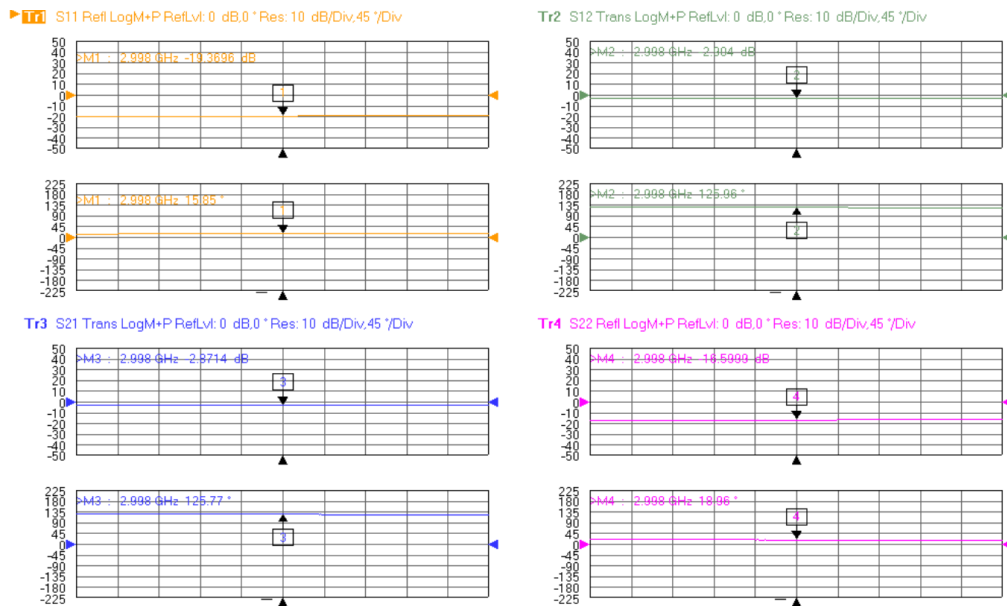


Fig. 3.7 Screen of the VNA's software interface

In Tab. 3.1 the measurements of the four S-parameters (in dB) at the frequency of  $f=2.998\text{GHz}$  (approximation of  $2.99792\text{GHz}$ ) for each discrete step of the “cylinder turns” value have been collected.

Besides the S-parameter values the power division ratio  $r$  as illustrated in chapter 1 has been reported, along with the percentage of the through and coupled powers and the total losses.

Tab. 3.1 VNA measurements on the Riblet short slot coupler.

# Turns	Cylinder Depth P <sub>D</sub> [mm]	S <sub>11</sub> [dB]	S <sub>21</sub> [dB]	S <sub>31</sub> [dB]	S <sub>41</sub> [dB]	% Through	% Coupled	% Total Loss	$r = \frac{ b_3 ^2}{ b_2 ^2}$
0	0	-16.8	-2.8	-3.6	-20.8	52.5	43.7	3.8	0.83
1	1.56	-18.0	-2.9	-3.4	-22.6	51.3	45.7	3.0	0.89
2	3.12	-19.2	-3.0	-3.2	-25.1	50.1	47.9	2.0	0.95
3	4.68	-20.9	-3.2	-3.0	-29.2	47.9	50.1	2.0	1.05
4	6.24	-22.8	-3.4	-2.7	-37.0	45.7	53.7	0.6	1.17
5	7.8	-25.1	-3.7	-2.4	-40.8	42.7	57.5	-0.2	1.35
6	9.36	-26.9	-4.1	-2.2	-29.0	38.9	60.3	0.8	1.55
7	10.92	-27.1	-4.5	-1.9	-24.2	35.5	64.6	-0.1	1.82
8	12.48	-27.2	-5.1	-1.6	-21.0	30.9	69.2	-0.1	2.24
9	14.04	-27.8	-5.8	-1.4	-18.7	26.3	72.4	1.3	2.75
10	15.6	-30.0	-6.6	-1.2	-16.8	21.9	75.9	2.2	3.47
11	17.16	-32.0	-7.6	-1.0	-15.5	17.4	79.4	3.2	4.57
12	18.72	-25.0	-8.8	-0.9	-14.0	13.2	81.3	5.5	6.17

In particular, the S-parameters (in dB) have been obtained by measuring their value with the VNA, alternating the ports as previously described.

The percentages of coupled and through powers (with respect to the input power) have been obtained instead as follows:

$$\begin{aligned} |S_{21}|_{dB} &= 20 \log \frac{|b_2|}{|a_1|} = 10 \log \frac{|b_2|^2}{|a_1|^2} \\ |S_{31}|_{dB} &= 20 \log \frac{|b_3|}{|a_1|} = 10 \log \frac{|b_3|^2}{|a_1|^2} \end{aligned} \quad (3.2)$$

$$\begin{aligned} \%P_{THROUGH} &= \frac{P_2}{P_1} * 100 = \frac{|b_2|^2}{|a_1|^2} * 100 = 10^{\frac{|S_{21}|_{dB}}{10}} * 100 \\ \%P_{COUPLED} &= \frac{P_3}{P_1} * 100 = \frac{|b_3|^2}{|a_1|^2} * 100 = 10^{\frac{|S_{31}|_{dB}}{10}} * 100 \end{aligned} \quad (3.3)$$

If the device is lossless, matched and perfectly isolated (the signal at output of the isolated port should be zero, that means  $S_{41} = -\infty$ ) then the sum of the powers at the output of port 2 and 3 should be equal to the input power at port 1. This is not the case, since the device is real, present some losses and the isolation as shown in Tab. 3.1 is high but not infinite. So the percentage of the total power lost with respect to the input power can be obtained as:

$$\%P_{LOSS} = 100\% - (\%P_{THROUGH} + \%P_{COUPLED}) \quad (3.4)$$

Regarding the total power loss, for #turns = 5, 7, 8 the numeric value becomes negative (even if by only 0.1-0.2%). This is obviously impossible, since the sum of the output powers from port 2 and 3 cannot be larger than the power at the input of port 1, since this is a passive device. So this must be interpreted for sure as the result of the approximation executed when reading the values of the S-parameters on the VNA, and in this case the total power loss can be considered zero. This means that at this particular frequency, for the cylinder that penetrates at almost half-length of its maximum depth, the isolation becomes maximum: this interpretation is corroborated by the value of isolation at #turns=5, -40.8dB, a very high value.

This means that the cylinder depth inside the coupling section not only controls the power division ratio  $r$  between the two output ports, but also the isolation.

Finally, the power division ratio  $r$  has been computed as (referring again to 3.2 for the definition of  $|S_{21}|_{dB}$  and  $|S_{31}|_{dB}$ ):

$$\begin{cases} |b_3|^2 = |a_1|^2 10^{\frac{|S_{31}|_{dB}}{10}} \\ |b_2|^2 = |a_1|^2 10^{\frac{|S_{21}|_{dB}}{10}} \end{cases} \quad (3.5)$$

$$r = \frac{|b_3|^2}{|b_2|^2} = \frac{|a_1|^2 10^{\frac{|S_{31}|_{dB}}{10}}}{|a_1|^2 10^{\frac{|S_{21}|_{dB}}{10}}} = 10^{\frac{|S_{31}|_{dB} - |S_{21}|_{dB}}{10}} \quad (3.6)$$

The power division ratio for every value of #turns has been reported in Tab. 3.1. As an example, and also because it is the value of  $r$  that will be used to design the coupling section, we can take the case #turns=0, which is when the cylinder is completely outside of the coupling section. In this case:

$$r = \frac{|b_3|^2}{|b_2|^2} = 10^{\frac{|S_{31}|_{dB} - |S_{21}|_{dB}}{10}} = 10^{\frac{-3.6 - (-2.8)}{10}} = 10^{-0.08} = 0.83 \quad (3.7)$$

This value of the power division ratio can now be used to design in the next section a Riblet short slot coupler in CST that has similar performance to the physical one.

In this way the electromagnetic field inside the simulated structure should have similar configuration to the one inside the physical device (at least for the frequency under analysis).

The performances of the simulated device vs. the real one will be analyzed at the given frequency by comparing the S-parameters of the two (measured vs. simulated).

### 3.2 Modelling and simulation of the Riblet short slot coupler in CST MWS

The design of the Riblet short slot coupler will follow the theory illustrated in the first chapter, which in turn is based on the work developed in [32].

Some geometrical measurements have been performed on the physical device, basing the CST design on the original one.

In particular the following geometrical parameters are already known: the dimensions of the ports (standard WR284), the height of the coupling section (which correspond to the height of the WR284 standard), and the width of the coupling section  $W_{CS}$ , which has been approximately measured with two wooden sticks inserted inside the coupling section.

It is known also the working frequency of the system (2.99792GHz) and other minor geometrical details of the original design.

In Tab. 3.2 the physical values known from electrical or geometrical measurements has been reported.

Tab. 3.2 Some geometrical and electrical features of the physical device

Parameter	Value	Description
Material	Aluminum	Material of the entire device
$a$	72.136 mm	Width of the input port
$b, H_{CS}$	34.036 mm	Height of both the input port and the coupling section
$W_{CS}$	128 mm	Width of the coupling section
$f$	2.99792GHz	Working frequency of the system
$r$	0.83	Power division ratio (when the cylinder is completely outside of the coupling section)

The width of the coupling section as stated in [32] is such that the  $TE_{10}$  and  $TE_{20}$  modes are in propagative condition, while the  $TE_{30}$  mode is in cut-off. Indeed by computing the cutoff frequencies of those three modes inside the coupling section we have:

$$f_{c_{TEmo}} = \frac{1}{2\pi} \sqrt{\frac{\left(\frac{m*\pi}{W_{CS}}\right)^2 + \left(\frac{0*\pi}{H_{CS}}\right)^2}{\mu\epsilon}} = \frac{c}{2\pi} \frac{m\pi}{W_{CS}} \quad (3.8)$$

$$f_{c_{TE10}} = \frac{c}{2\pi} \frac{1 * \pi}{W_{CS}} \simeq \frac{3 * \frac{10^8 m}{s}}{2 * 128 * 10^{-3} m} = 1.17 GHz \quad (3.9)$$

$$f_{c_{TE20}} = \frac{c}{2\pi} \frac{2\pi}{W_{CS}} \simeq \frac{3 * 10^8}{128 * 10^{-3} m} = 2.34 GHz \quad (3.10)$$

$$f_{c_{TE30}} = \frac{c}{2\pi} \frac{3\pi}{W_{CS}} = \frac{3}{2} * \frac{3 * 10^8}{128 * 10^{-3} m} = 3.51 GHz \quad (3.11)$$

This shows that at the f=2.99792GHz in the coupling section the TE<sub>10</sub> and TE<sub>20</sub> are in propagative condition, while the TE<sub>30</sub> is in cutoff since the excitation frequency is below the cutoff frequency, so this mode cannot propagate inside the coupling section.

This is the principle on which the Riblet short slot coupler operates: the TE<sub>10</sub> and TE<sub>20</sub> are both present in the coupling section, and the coupling between the input and coupled port happens thanks to the interaction between those two modes.

Instead in the regular WR284 waveguide only the TE<sub>10</sub> should propagate.

While those first geometric parameters have been easily obtained, the measure of the length of the coupling section L<sub>cs</sub> presented some difficulties, since we hadn't access to the inner portion of the coupling section. The theory reported in [32] has been extremely useful for this purpose.

Indeed, as already discussed in chapter 1 in the section regarding the Riblet short slot coupler, the power division ratio r is related to the length of the coupling section and to the phase shift between the even and odd mode by the following relation [32]:

$$\delta_{eo} = \frac{\varphi_e - \varphi_o}{2} = -(\beta_e - \beta_o) \left| \frac{L_{CS}}{2} = -\arctan(r) \right. \quad (3.12)$$

Since it is already known the power division ratio  $r$  of the physical device when the cylinder is completely outside of the coupling section (so the power division ratio in this case is uniquely due to the physical length  $L_{CS}$ ), by computing the propagation constants  $\beta_e$  and  $\beta_o$  of the even ( $TE_{10}$ ) and odd ( $TE_{20}$ ) modes the length of the coupling section can be obtained from 3.12.

We can compute the propagation constants, by using 1.33 and 1.34:

$$\begin{aligned} \beta_e = \beta_{TE10} &= \sqrt{\omega^2 \mu \epsilon - \left(\frac{\pi}{W_{CS}}\right)^2} \approx \\ &\approx \sqrt{\left(\frac{2\pi * 2.99792 * 10^9 Hz}{2.99792 * 10^8 \frac{m}{s}}\right)^2 - \left(\frac{\pi}{128 * 10^{-3} m}\right)^2} = 57.8 m^{-1} \end{aligned} \quad (3.13)$$

$$\begin{aligned} \beta_o = \beta_{TE20} &= \sqrt{\omega^2 \mu \epsilon - \left(\frac{2\pi}{W_{CS}}\right)^2} \approx \\ &\approx \sqrt{\left(\frac{2\pi * 2.99792 * 10^9 Hz}{2.99792 * 10^8 \frac{m}{s}}\right)^2 - \left(\frac{2\pi}{128 * 10^{-3} m}\right)^2} = 39.2 m^{-1} \end{aligned} \quad (3.14)$$

As shown in 3.13 and 3.14, to compute the propagation constants in the coupling section its width  $W_{CS}$  must be already fixed. Therefore, to design this device, as first step the width of the coupling section must be dimensioned by imposing the non-propagative condition on the  $TE_{30}$  while assuring the propagation of the  $TE_{20}$ ; then the propagation constants must be determined by 3.13 and 3.14, and finally the length of the coupling section can be fixed by inverting 3.12 and substituting the desired power division ratio:

$$L_{CS} = \frac{2 \arctan(r)}{\beta_e - \beta_o} \Big|_{f=f_0} = \frac{2 \arctan(0.83)}{(57.8 - 39.2) m^{-1}} = 74.5 mm \quad (3.15)$$

By executing various parametric sweep of the geometry of the device, via CST MWS (in order to approximately match the S-parameters of the model to the ones of the physical device) a final value of  $L_{CS}=68.6$  mm has been attributed to the length of the coupling section (a difference of just  $\Delta L_{CS}=5.9$  mm from the theoretically computed value).

Besides from the coupling section, the Riblet short slot coupler is also composed of a transformer section. Indeed, in order to match the modal impedances of the TE<sub>10</sub> and TE<sub>20</sub> modes in the coupling section to the ones of the TE<sub>10</sub> inside the input ports, a matching section is required.

In more evolved designs the matching section can consist of more than one H-plane steps whose modal impedances (and then accordingly length and width) must be opportunely fixed by employing the theory of small reflections and multi-section transformer illustrated in [1] in order to minimize reflections and assuring a maximum power transfer.

An example of a Riblet short slot coupler which employs a three-section transformer as a matching section is shown in Fig. 3.8.

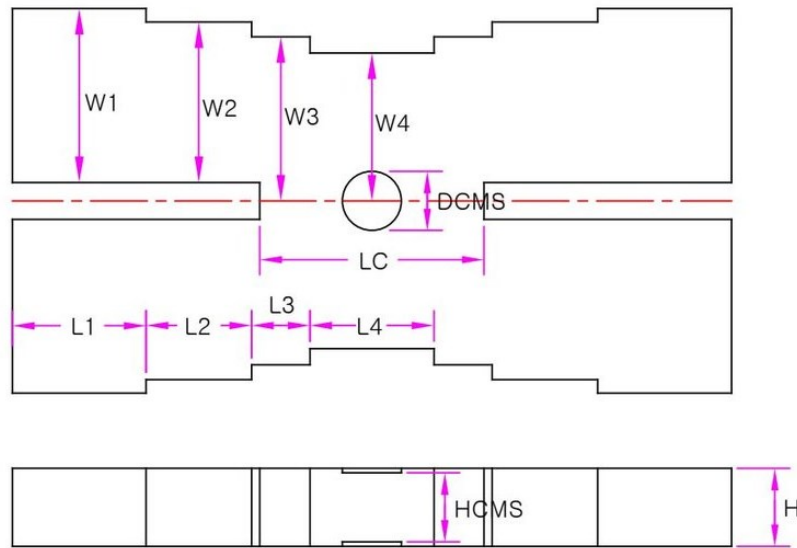


Fig. 3.8 Riblet short slot coupler employing three transformer sections [43]

The more the steps employed in the transformer section, the better the frequency response of the device will be (that means larger bandwidth). Indeed a bigger number of transformer sections leads to a more gradual variation of the modal impedances, leading to a minor amount of reflections and a larger bandwidth. The original coupler that needs to be modelled in CST (Fig. 3.4) has a single transformer section, which however is not visible from the outside of the device. Moreover, the input ports as can be seen in Fig. 3.4 follow a particular shape, of which no reference has been found in literature. It can be presumed it has been obtained by the original manufacturer of the device by optimizing the structure employing parametric sweep of unspecified geometric parameters.

Since the main aim of this work is to study the multipaction effect inside the coupling section, the goal of the electromagnetic analysis with CST is to obtain in simulation a configuration of electromagnetic field similar to the one present inside the physical device when excited with a single frequency.

This means that we are not interested in the frequency response of the device, only in its behavior at the center frequency  $f=2.99792\text{GHz}$ .

So only a single coupling section has been employed in the CST modelling of the device, as in the original design; moreover we have not concerned ourselves with the shape of the input ports after the matching section. Those have been kept with a simple circular geometry, which however achieves the goal of minimizing reflections at the working frequency.

In Fig. 3.9 a 3D view of the device designed in CST MWS is reported.

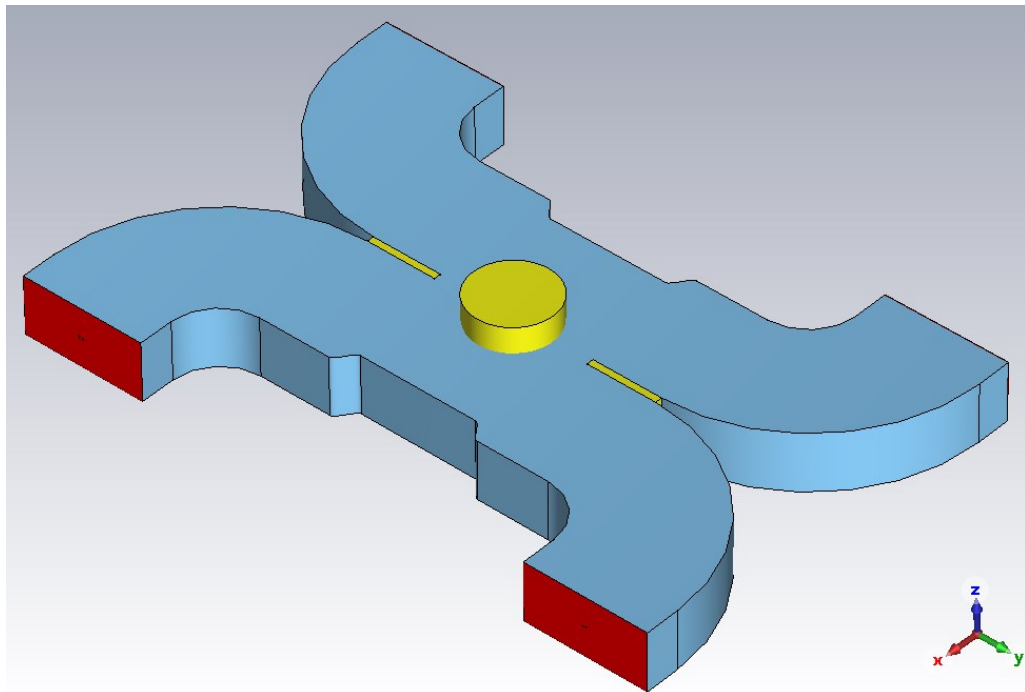


Fig. 3.9 The Riblet short slot coupler designed in CST MWS. Light blue: vacuum. Yellow: aluminum. Red: Input/Output ports

This design has been modelled by employing aluminum as a background material, and constructing the blocks which constitute the device itself with vacuum solids by applying perfect electric condition PEC at the boundary. This approach is sometimes simpler than designing metallic solids in vacuum background, and this does not affect the electromagnetic analysis (it will be shown instead that for the multipaction analysis this requires a more careful approach and minor

adjustments, since in CST PS the background material cannot emit secondary electrons).

With regard to the geometry of the designed device, the following elements can be noticed: the coupling section at the center; the matching sections at both sides of the coupling section; the junctions between the coupling section and the adapter sections, which have been obtained by using the “loft” operation in CST MWS; the metallic cylinder and the two so-called “septum” (which are the only metallic elements in the entire design, except for the background material, and they are distinguished by a yellow color); the circular arms that constitute the rectangular waveguide input/output sections, and the input ports (in red).

In Fig. 3.10 a cross-section view along the z-axis of the same design is shown.

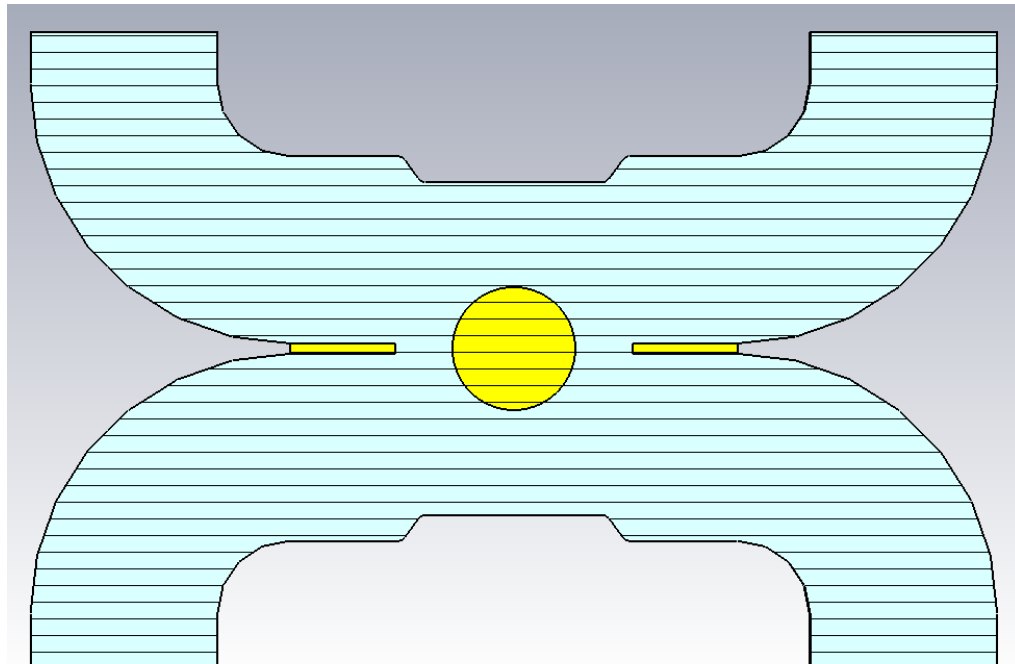


Fig. 3.10 The Riblet short slot coupler designed in CST MWS. Cross-section view along the z axis, for  $z=0$ .

The geometry of the device is very simple, and it exhibits high symmetry. In the following page a table which summarize the most important geometrical parameters used in this project has been reported, employing the same naming convention adopted in the CST design.

Tab. 3.3 Geometrical features of the Riblet short slot coupler modelled in CST

Parameter	Value [mm]	Description
wvg_width_a	72.136	Width of the input port
wvg_height_b	34.036	Height of both the input port and the coupling section
body_Wcs	128	Width of the coupling section
body_Lcs	68.6	Length of the coupling section
adapter_width	148	Width of the adapter section
adapter_length	41.8	Length of the adapter section
adapter_body_distance	10	Distance between the adapter section and the coupling section
septum_width	4	Width of the septum which separates two adjacent ports
cylinder_radius	23.8	Radius of the metallic cylinder
cylinder_depth	$1.56 \times \text{Nstep}$	Penetration depth of the cylinder inside the coupling section

The parameter Nstep provided in the last row parametrizes the number of turns of the screw system that control the penetration depth of the cylinder inside the coupling section. It corresponds to the #Turns value which has been employed in the measures executed in section 3.1. In the simulations this parameter has been called cylinder\_step, and the parametric sweep has been executed by assigning it integer values from 0 (cylinder completely outside) to 12 (cylinder completely inside). Therefore, cylinder\_step= Nstep=#Turns.

With “cylinder completely inside” it is intended the maximum depth that the cylinder can reach in the physical device; indeed, it never reaches the bottom wall of the coupling section, not in the simulation and neither in the physical device. After the whole design has been completed, a simulation employing a frequency domain solver has been performed in CST Microwave Studio.

In the following pages are reported the plots of the main S-parameters of the device in the range 2.8÷3.2GHz (opportunely elaborated for the plot with a custom python script), a table containing the S-parameters at the single frequency  $f=2.99792\text{GHz}$  (with comparison between simulated and measured data), and two images extracted from the monitor of the electric field for two different values of the cylinder\_step parameter.

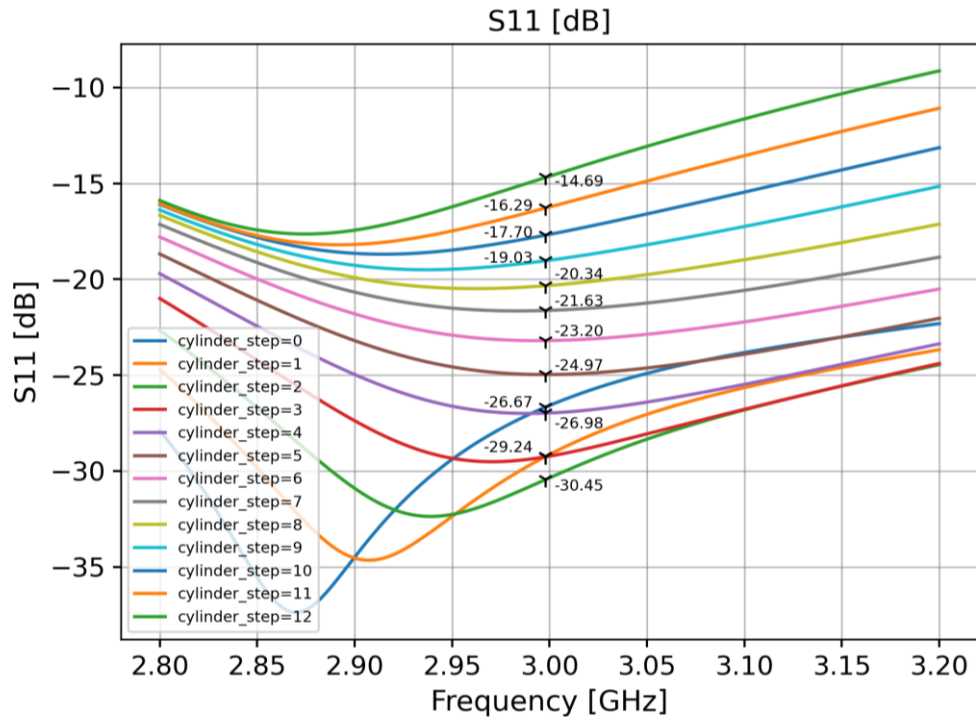


Fig. 3.11 S<sub>11</sub> parameters simulated with CST MWS, for different values of the cylinder\_step parameter.

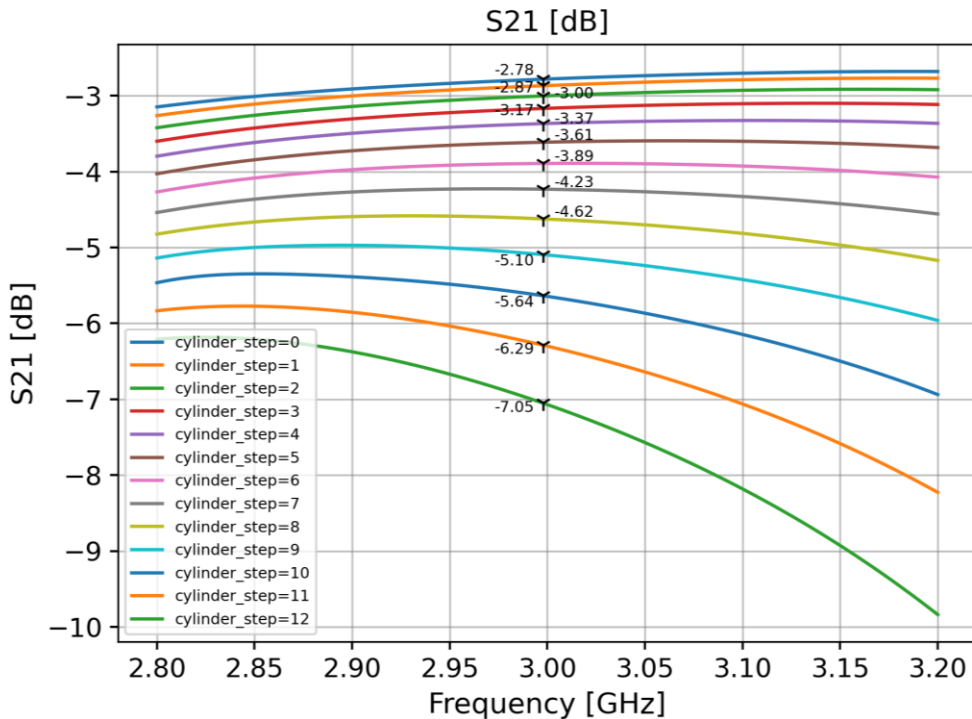


Fig. 3.12 S<sub>21</sub> parameters simulated with CST MWS simulations, for different values of the cylinder\_step parameter

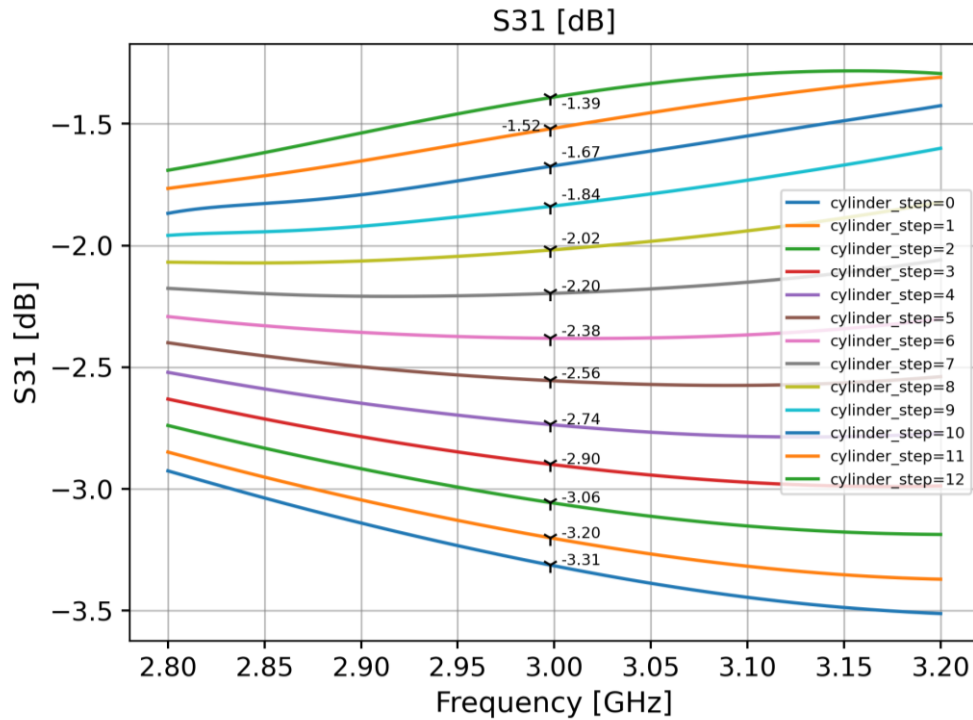


Fig. 3.13  $S_{31}$  parameters simulated with CST MWS simulations, for different values of the `cylinder_step` parameter

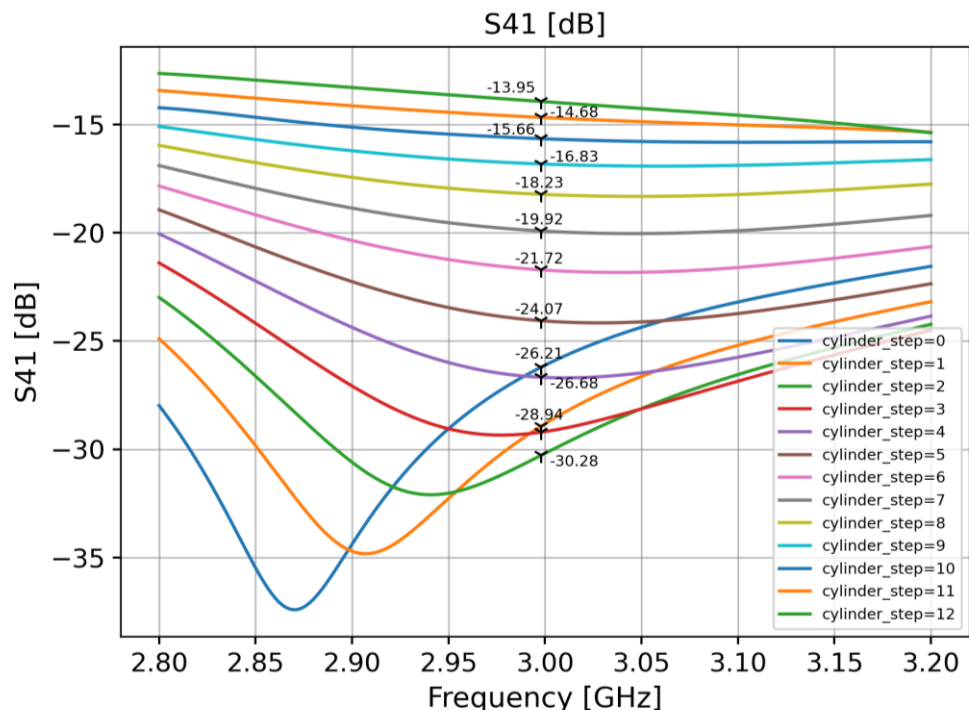


Fig. 3.14  $S_{41}$  parameters simulated with CST MWS simulations, for different values of the `cylinder_step` parameter

Tab. 3.4 Simulated vs measured S-parameters

# Turns	Cylinder Depth P <sub>D</sub> [mm]	S <sub>11</sub> [dB]		S <sub>21</sub> [dB]		S <sub>31</sub> [dB]		S <sub>41</sub> [dB]	
		Measured	CST	Measured	CST	Measured	CST	Measured	CST
0	0	-16.8	-26.67	-2.8	-2.78	-3.6	-3.31	-20.8	-26.21
1	1.56	-18.0	-29.24	-2.9	-2.87	-3.4	-3.20	-22.6	-28.94
2	3.12	-19.2	-30.45	-3.0	-3.00	-3.2	-3.06	-25.1	-30.28
3	4.68	-20.9	-29.26	-3.2	-3.17	-3.0	-2.90	-29.2	-29.21
4	6.24	-22.8	-26.98	-3.4	-3.37	-2.7	-2.74	-37.0	-26.68
5	7.8	-25.1	-24.97	-3.7	-3.61	-2.4	-2.56	-40.8	-24.07
6	9.36	-26.9	-23.20	-4.1	-3.89	-2.2	-2.38	-29.0	-21.72
7	10.92	-27.1	-21.63	-4.5	-4.23	-1.9	-2.20	-24.2	-19.92
8	12.48	-27.2	-20.34	-5.1	-4.62	-1.6	-2.02	-21.0	-18.23
9	14.04	-27.8	-19.03	-5.8	-5.10	-1.4	-1.84	-18.7	-16.83
10	15.6	-30.0	-17.70	-6.6	-5.64	-1.2	-1.67	-16.8	-15.66
11	17.16	-32.0	-16.29	-7.6	-6.29	-1.0	-1.52	-15.5	-14.68
12	18.72	-25.0	-14.69	-8.8	-7.05	-0.9	-1.39	-14.0	-13.95

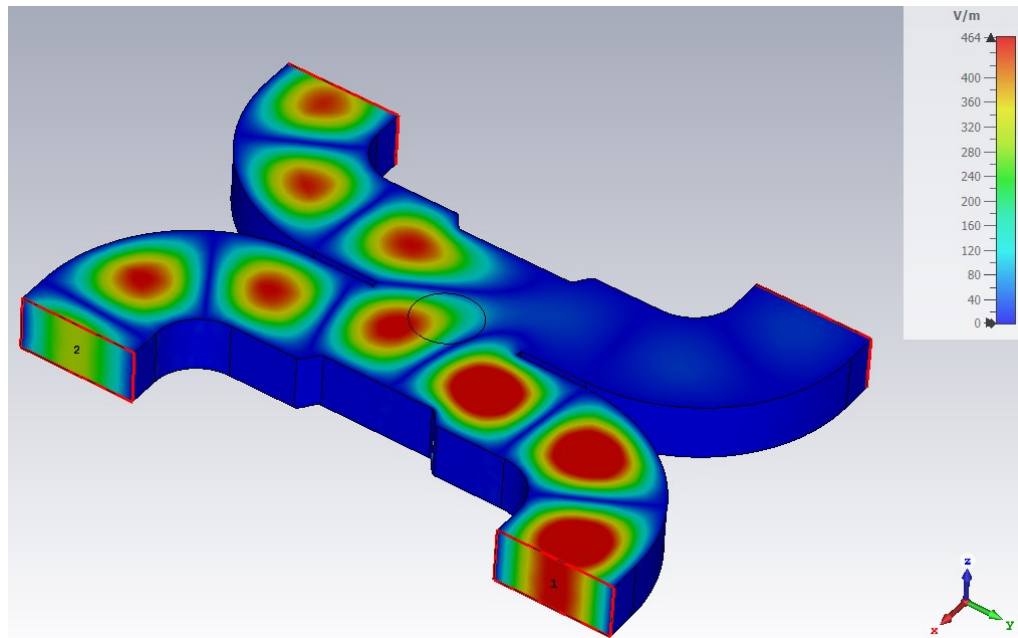


Fig. 3.15 Contour lines of the absolute value of the electric field, for cylinder\_step = 0 (cylinder all out). CST MWS simulation.

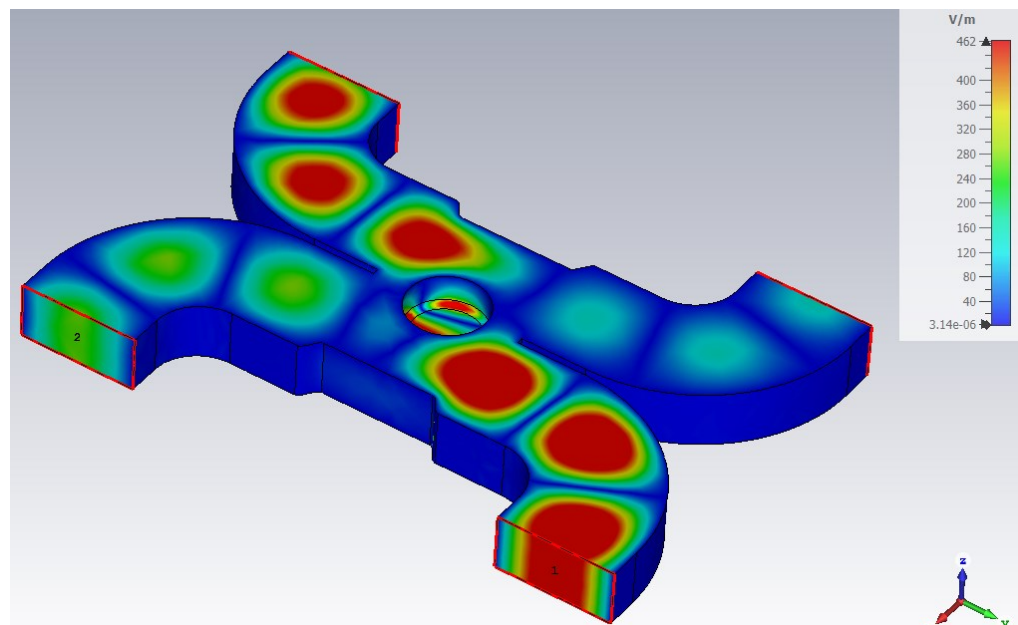


Fig. 3.16 Contour lines of the absolute value of the electric field, for cylinder\_step = 12 (cylinder all in). CST MWS simulation.

The plots in Fig. 3.11÷3.14 report the S-parameter of the device modelled in CST for different values of the cylinder\_step parameter, in a bandwidth 2.8GHz÷3.2GHz. The penetration depth of the cylinder inside the coupling section is given by cylinder\_step×1.56mm.

The values of the simulated S-parameters at the center frequency at which the device operates, namely at  $f=2.99792\text{GHz}$ , are reported in Tab. 3.4 along with the measured ones. By comparing the simulated vs. measured data, it can be shown that the device modelled in CST behaves similarly to the physical one.

For cylinder\_step = 5÷6 the S-parameter of the model and of the physical device (measured) are almost identical (with the exception of the  $S_{41}$ , for which the simulated version has a value of -24dB while the physical one provides -40.8dB). All the S-parameters however present great variation as the cylinder progress inside the coupling section. The measurements provide the best isolation at cylinder\_step=5 (-40.8dB), while the CST modelled one at cylinder\_step=2 (-30.28dB).

For the measurement the reflections are minimized at cylinder\_step=11 ( $S_{11} = -32\text{dB}$ ) while for the modelled one at cylinder\_step=2 ( $S_{11} = -30.45\text{dB}$ ).

The  $S_{21}$  parameters of the simulated vs physical device are pretty much in accordance in the range cylinder\_step = 0÷7, but they start to drift (even if by minor amounts) for higher values of this parameter. The same is true for the  $S_{31}$  parameter.

Obtaining for the modelled device values of the S-parameters that are identical to the physical one for every depth of the cylinder is almost impossible, since in the physical device the original designer could have used minor improvements of which we are not aware of; indeed the inner geometry of the device is not accessible to us and we've modelled the Riblet short slot coupler in CST based solely on external geometrical information at our disposal, at which has been added the analysis illustrated in [32] for the adjustment of the length of the coupling section in order to obtain the desired power division ratio.

In Fig. 3.15 and 3.16 the contour lines of the absolute value of the electric field inside the device for cylinder\_step=0 and cylinder\_step=12 are respectively shown; this analysis has been performed in CST by employing an electric field monitor, and it shows how for cylinder\_step=0 there is an almost equal power division ( $S_{21} = -2.78dB$ ,  $S_{31} = -3.31dB$ ) while for cylinder\_step=12 the power division is highly unbalanced ( $S_{21} = -7.05dB$ ,  $S_{31} = -1.39dB$ ) and most of the power goes into port 3, while very little comes out of port 2.

Red-colored regions correspond to higher values of electric field indeed, while in blue regions electric field is almost null (accordingly to the electric field level-meter displayed in the picture).

The final goal of modelling a device which electromagnetically behaves similarly to the physical one has been achieved. On this structure now a multipaction analysis can be performed, in order to estimate the power levels at which the physical device starts multipacting.

### 3.3 Multipaction analysis in CST Particle Studio of the Riblet short slot coupler modelled in CST MWS

In this final section of the chapter the multipaction analysis of the Riblet short slot coupler modelled in CST MWS are executed via CST PS environment. This operation is quite straightforward, since it requires only to change the type of problem in “Home->Problem Type”, by selecting in this menu “Particle->PIC” in order to enable the Particle-In-Cell analysis. This will automatically convert the design from a CST MWS file to a CST PS one.

The rest of the procedures are identical to the one executed in chapter 2 for the analysis of multipaction threshold in parallel plates waveguide, so here we won’t discuss the entire thing.

The only difference in this case is that the device which needs to be analyzed in this case has been obtained by employing vacuum-solids with an aluminum background. As reported in the CST Help manual [41] it is not possible in CST PS for a background material to have secondary emission properties.

But somehow secondary electrons must be generated at impact in order to model multipaction. This problem has been solved by coating the vacuum-solids with a thin shit of aluminum. In this way the coating can emit secondary electrons when it is hit by primary ones. Moreover, the coating has been designed such as that the exceeding portion of the aluminum goes out in the aluminum background, and not in the vacuum-solid. In this way the boundary conditions of the entire structure are not modified by the thin coating applied in the design.

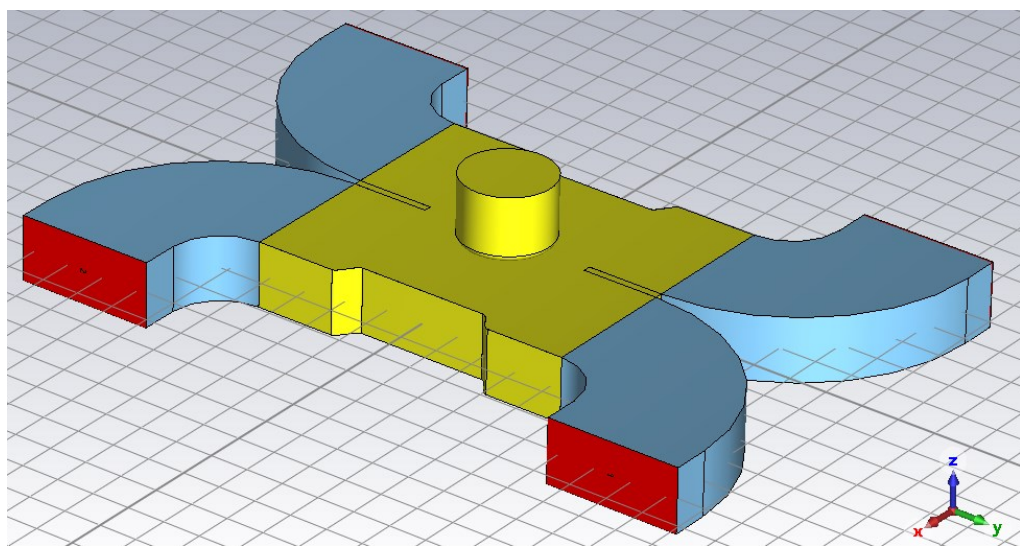


Fig. 3.17 Aluminum coating of the central section of the device.

As shown in Fig. 3.17 the coating has been applied only the central section of the device, composed of the coupling section and the matching section.

This means that the analysis will be restrained to this critical region, in which multipaction is more likely to happen due to the presence of the cylinder.

Indeed, the region between the bottom wall of the device and the upper wall of the cylinder can be thought as a parallel plate waveguide of dimension  $d$ , where  $d$  is the distance between the two surfaces. When the cylinder reaches higher depths inside the coupling section the critical gap  $d$  decreases, and so does the frequency-gap product; this means that lower values of the multipaction threshold should be expected, as shown by the Hatch and Williams charts, in which to lower values of the  $f \times d$  product correspond a lower multipaction threshold.

In Fig. 3.18 a screenshot of the primary electron emission plane is reported on the bottom wall of the device (precisely on the bottom aluminum coating).

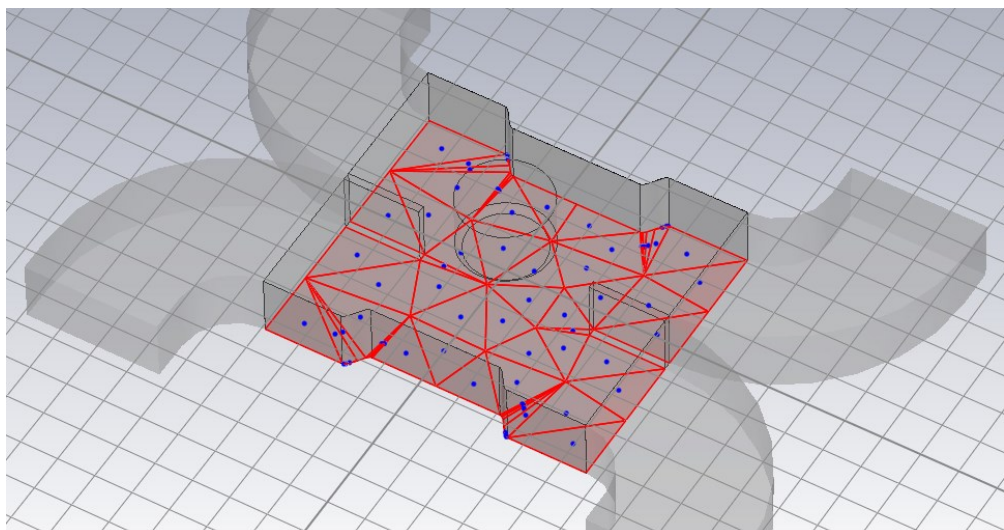


Fig. 3.18 Primary electron emission plane, on the bottom wall of the device.

After the initial setup the multipaction threshold analysis has been performed, with the techniques already discussed in chapter 2. In particular since this time an initial value which provided insight on the order of magnitude of the threshold was not available, very short PIC simulations have been executed with high power levels; the levels that already shown multipaction have been excluded from possible multipaction threshold candidates, and progressively the simulation times have been enlarged and the levels of power at input decreased, until a multipaction threshold becomes evident. The following plots show the number of particles in the device as a function of time for cylinder\_step=0 for different levels of input power.

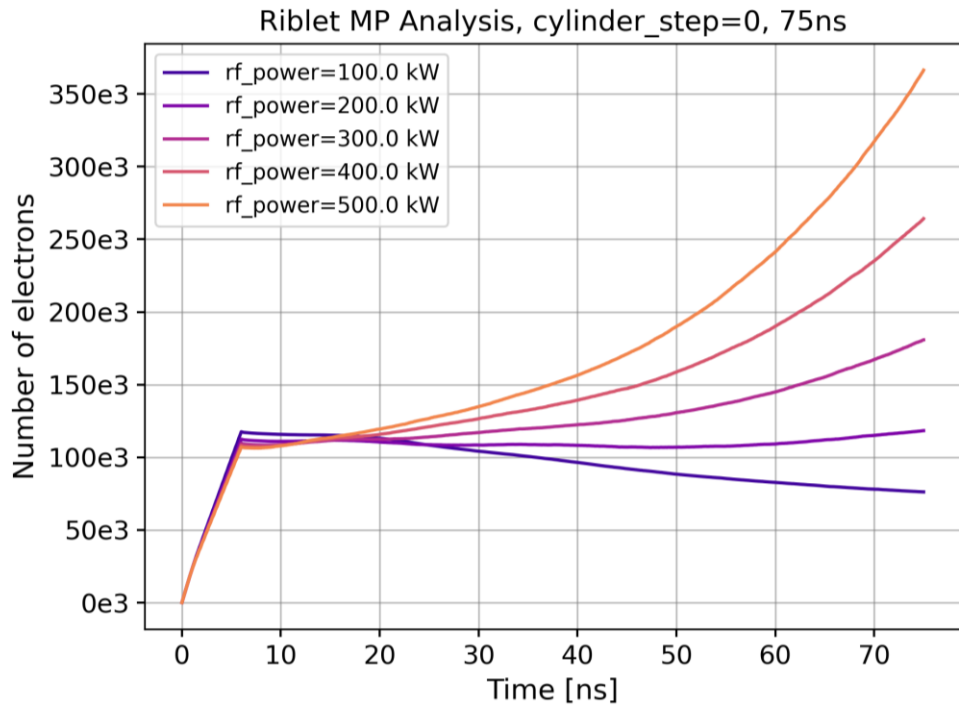


Fig. 3.19 Riblet multipaction analysis for cylinder\_step=0, rf\_power=100÷500kW, runtime=75ns.

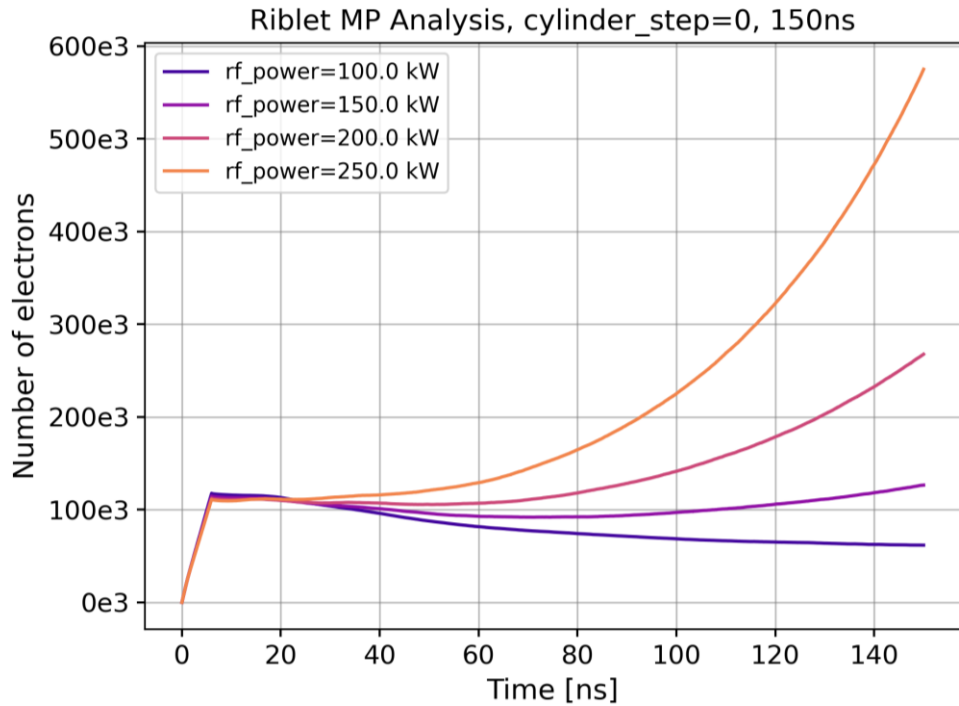


Fig. 3.20 Riblet multipaction analysis for cylinder\_step=0, rf\_power=100÷250kW, runtime=150ns.

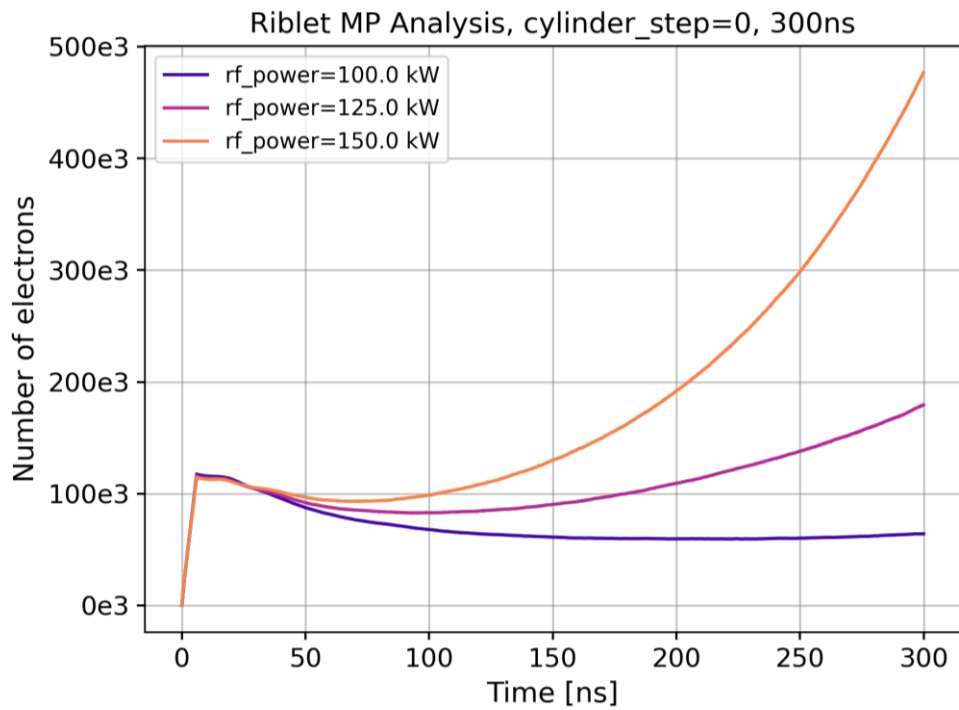


Fig. 3.21 Riblet multipaction analysis for cylinder\_step=0, rf\_power=100÷150kW, runtime=300ns.

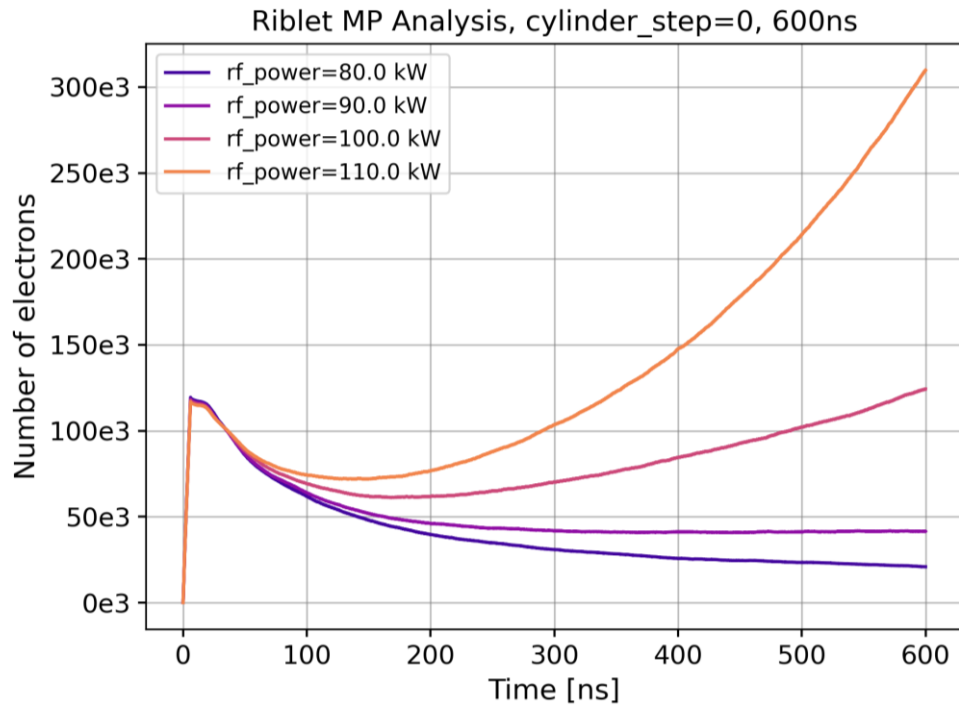


Fig. 3.22 Riblet multipaction analysis for cylinder\_step=0, rf\_power=80÷110kW, runtime=600ns.

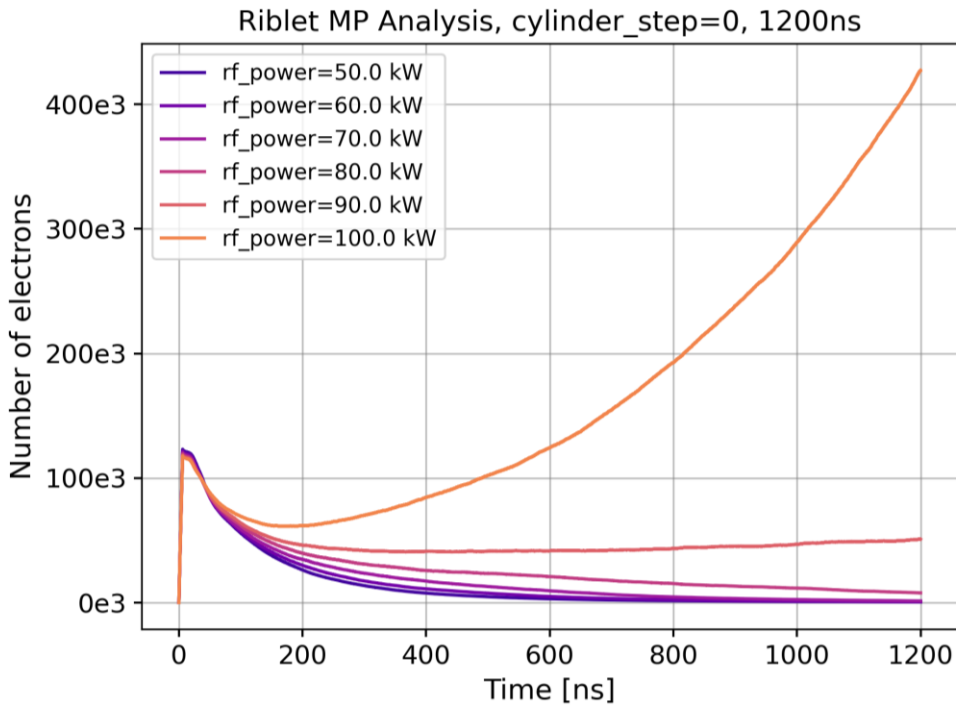


Fig. 3.23 Riblet multipaction analysis for cylinder\_step=0, rf\_power=50÷100kW, runtime=1200ns.

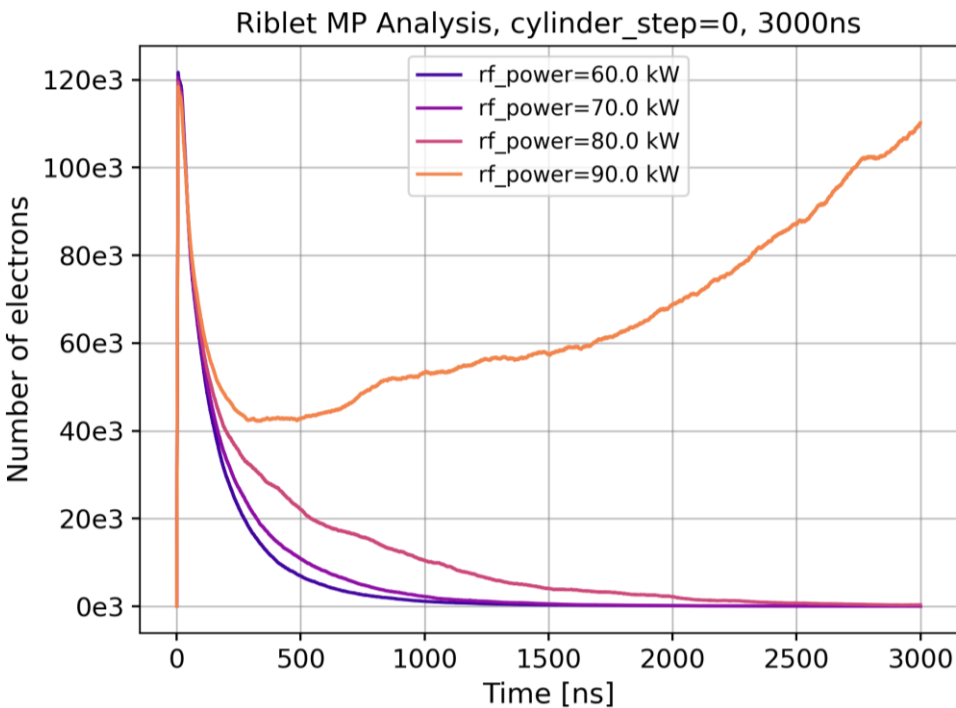


Fig. 3.24 Riblet multipaction analysis for cylinder\_step=0, rf\_power=60÷90kW, runtime=3000ns.

In Fig. 3.19÷3.24 the plots “number of particles vs. time” of different multipaction simulations in the device under study are reported. All the input power levels are expressed as RMS values. In particular, in Fig. 3.19 with a 75ns analysis multipaction is already detected for an input power of 300kW CW RMS; indeed, at this level there is already a growing trend in the electron population, which at 400kW is even more prominent. Fig. 3.20, with a 150ns analysis exhibits the presence of multipaction at 200kW. Fig. 3.21 and 3.22 clearly show the presence of multipaction at 125kW and 100kW, respectively. Fig. 3.23 with a runtime of 1200ns confirm the presence of multipaction at 100kW, while it seems unsure if it is already present at 90kW. Fig. 3.24 finally, with a runtime of 3000ns, shows how the curve of electron population vs. time present a steady grow at 90kW of input power, even if it does not seem to reach levels above the initial electron population (around 120000 electrons).

Since multipaction is confirmed at 100kW CW RMS, and at 90kW CW RMS is present a tangible growth of electrons even if not prominent as in the other cases, it can be said that for CW excitation the multipaction threshold of this device when working under vacuum conditions and when the cylinder is completely outside is at 90kW RMS (180kW of peak power).

By increasing the penetration depth of the cylinder, a lower multipaction threshold can be observed since the critical gap between the bottom wall of the coupling section and the surface of the cylinder decreases. Indeed, this is what happens, as the multipaction analysis for cylinder\_step=12 reported in the following pages shows. In this case however the multipaction threshold of the device when the cylinder is not inserted (cylinder\_step=0) is already known (90kW RMS), so the threshold of the new configuration should be maximum 90kW RMS, and this restricts the range in which the multipaction analysis should be executed.

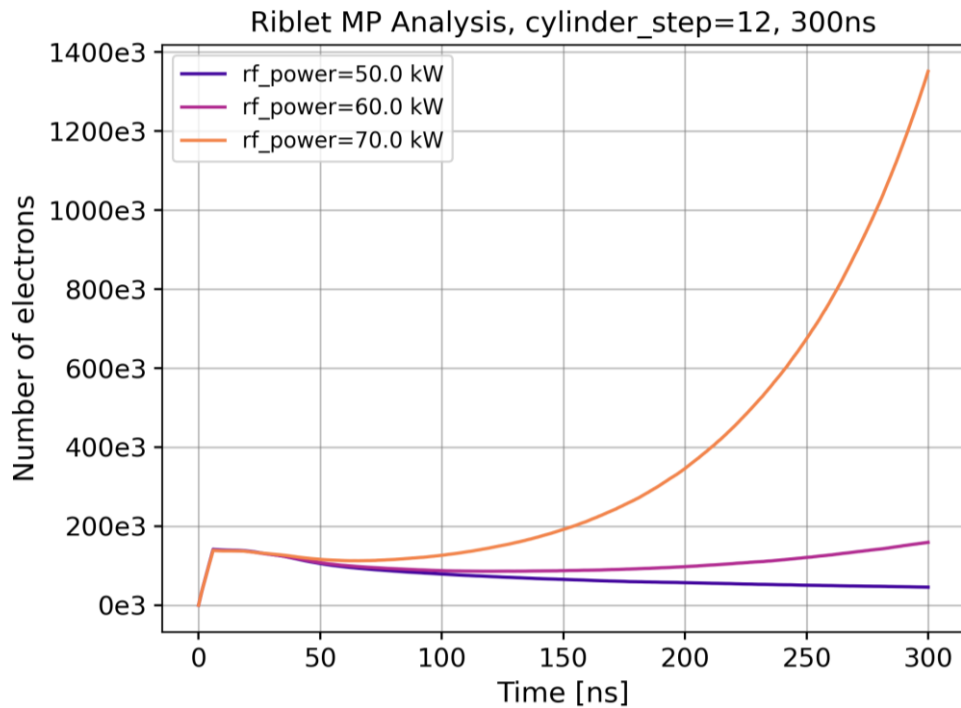


Fig. 3.25 Riblet multipaction analysis for cylinder\_step=12, rf\_power=50÷70kW, runtime=300ns.

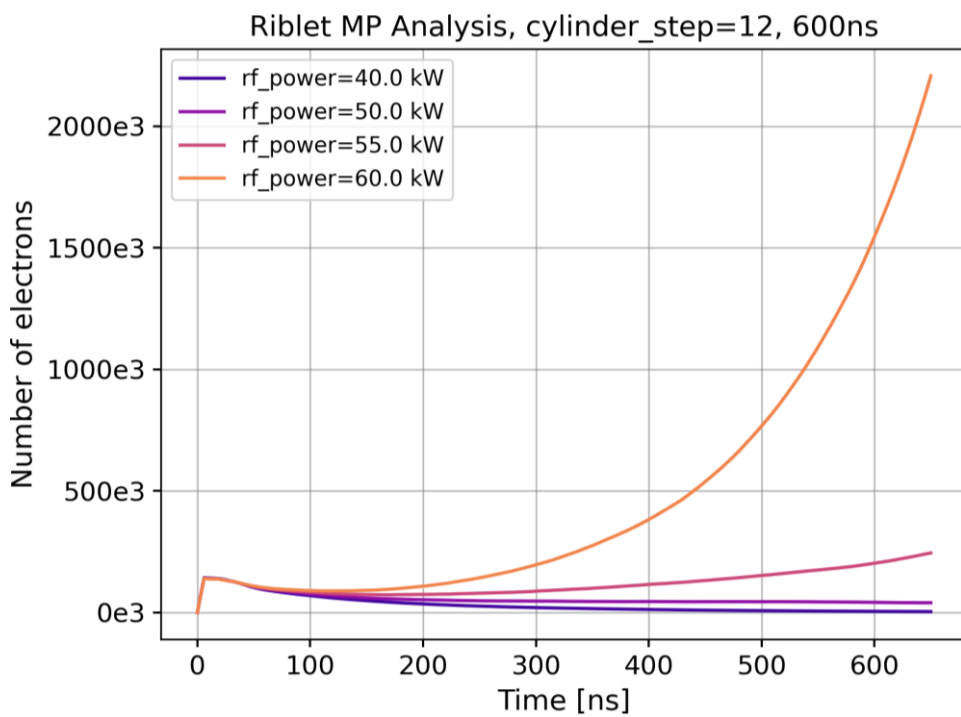


Fig. 3.26 Riblet multipaction analysis for cylinder\_step=12, rf\_power=40÷60kW, runtime=600ns.

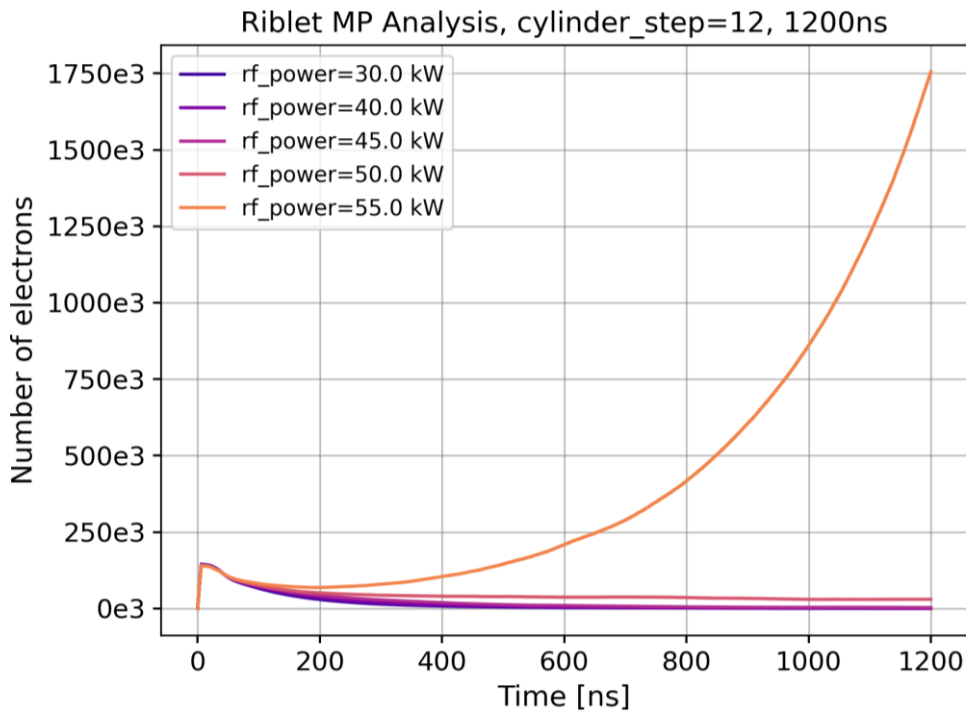


Fig. 3.27 Riblet multipaction analysis for cylinder\_step=12, rf\_power=30–55kW, runtime=1200ns.

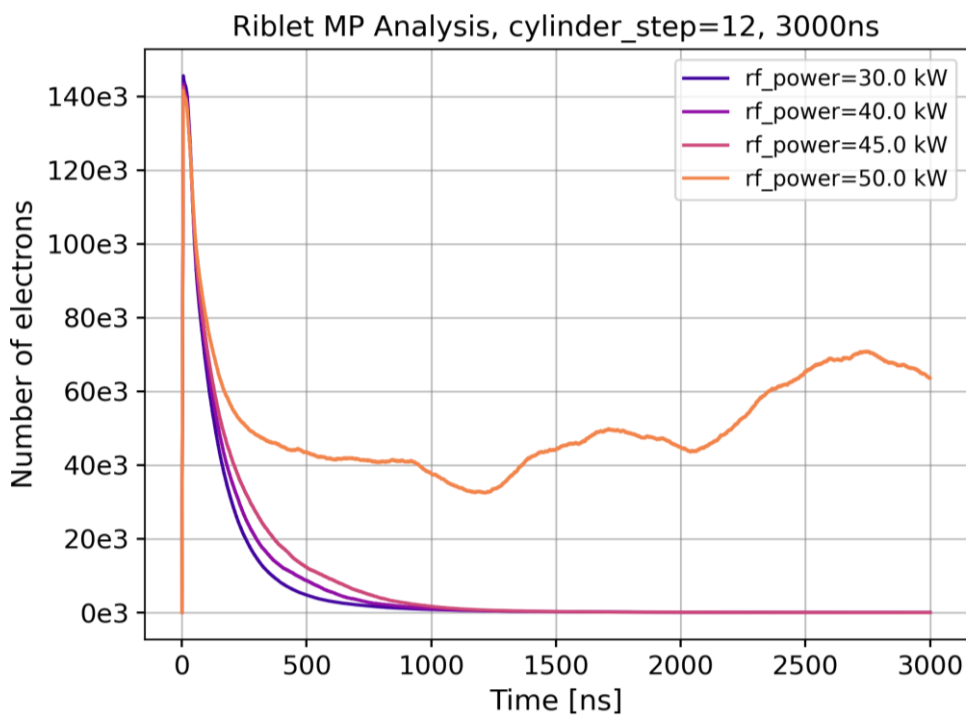


Fig. 3.28 Riblet multipaction analysis for cylinder\_step=12, rf\_power=30–55kW, runtime=3000ns.

The plots from Fig. 3.25÷3.28 can be interpreted as follows. In Fig. 3.25 a sweep of the input rf\_power is performed in the range 50÷70 kW, with a runtime of 300ns. In particular at 70kW multipaction is clearly present, since the electron population experience exponential growth. Fig. 3.26, with a runtime of 600ns, shows an exponential growth (and thus multipaction) for an input power of 60kW. Fig. 3.27, with a runtime of 1200ns, shows an exponential growth (and thus multipaction) for an input power of 55kW. Finally in Fig. 3.28 a runtime of 3000ns has been employed, with an input power in the range 30÷50kW. Even if the curve for rf\_power=50kW does not experience exponential growth, it still does not decay like all the other curves for lower power levels. Instead, it shows a growth after 2000ns. This should be an indication of multipaction, since it could mean that (on average) the amount of electron gained due to secondary emissions starts to balance the amount of the one lost due to absorption, and this could be taken as the definition of multipaction threshold, which in this case can be assumed to be at 50kW RMS. This indication moreover is in accordance with the multipaction confirmed for an input power of 55kW, and the complete decay of electron population for an input power of 45kW, so a multipaction threshold of approximately 50kW RMS is a value in accordance with those two limits.

In conclusion, for CW excitation, when the cylinder is completely out of the coupling section the multipaction threshold approximately can be fixed at 90kW RMS; when the cylinder instead has reached the maximum penetration depth (for cylinder\_step=12, and this is the worst-case scenario) the multipaction threshold becomes nearly half of it, approximately 50kW RMS. This must be somehow accounted for when using this device at power levels beyond 50kW RMS: if one wants to avoid multipaction, and thus possibly arcing, outgassing and corona discharges which could lead to RF breakdown, the penetration depth of the cylinder must be kept much lower than the value corresponding to cylinder\_step=12 (this means, by Tab. 3.1, much lower than 18.72mm inside the coupling section). Possibly the cylinder system should be used only for a fine tuning of the power division ratio, and not for a fully customizable value of it.

Obviously, another solution here is to operate the device at power levels lower than 50kW RMS; in this case the full length of the cylinder can be leveraged.

# Conclusions

---

The results obtained in this thesis indicate the level of input power corresponding to the multipaction threshold occurring in hybrid couplers employed in the LINAC plant. This threshold should not be surpassed when employing couplers in the RF power distribution system of the LINAC in order to avoid damages to the component itself, which could lead to malfunctioning of the entire plant. In particular, the effect of a metallic cylinder inserted in a coupler to perform a tuning of coupling performance is investigated.

When operating with power levels above 50kW CW RMS, i.e. the multipaction threshold found for the device when the cylinder is completely inside the coupling section, the cylinder should only be used for fine tunings of the power division ratio, keeping the screw mechanism just a few turns below the “zero” setting, avoiding to reach the maximum number of turns. Therefore, this device alone allows to obtain a narrow range of the power division ratio; by pushing it to a wider range while operating under high-power conditions, the multipaction (and thus arcing and RF breakdown) becomes highly possible.

To obtain a wider range of power division ratio while keeping power levels above the minimum threshold of this device (but still below 90kW RMS) a particular configuration that employs two Riblet short slot coupler could be suggested. In detail this configuration consists of two short slot couplers, with a phase shifter placed between them and opportunely connected to their ports. The cylinder of the two couplers can be used in this case just for a fine tuning of the system. The variations of the power division ratio can be obtained in this case by modifying the phase shift introduced by the phase shifter, which usually has a higher breakdown threshold than the device analyzed in this study. Indeed, it is possible to realize high-power phase shifters whose working principle is not based on the displacement of metallic elements, which are responsible for lowering the multipaction threshold in the original coupler.

Alternatively, to improve the multipaction threshold of the original device, the inner walls of the coupler could be treated with appropriate material coatings that reduces the secondary emissions. Since multipaction is due to secondary emissions, by reducing them the multipaction threshold should become higher. Another option consists in some variations of the geometry of the device; this approach is often employed in resonant cavities for example. By individuating the multipaction trajectories and the points where multipaction does happen, the geometry of the device can be adapted in order to avoid multipaction in those points, thus improving the multipaction threshold.

Multipaction is a really complex phenomenon; even if widely studied in literature its references are scattered through various research papers, and to the author knowledge there are not many books which treat this topic in all its aspect; but it still is an important physical phenomenon which every RF designer who works with high power devices, not only in waveguide technology but also in PCB, should be aware of. For high power applications, the designer not only must take into account the electromagnetic performances of the device, employing EM simulations with widely known software, but also a multipaction and a corona discharge analysis on the device should be performed, in order to minimize the risks due to this phenomenon.

Future developments of this work could consist in the investigation of multipaction in other devices employed both in particle accelerators, as resonant cavities, which are notoriously subjected to multipaction, but also in devices employed in satellite systems, like RF filters, where this phenomenon constitutes a major problem.

The design of custom algorithms for PIC simulations that address multipaction is another interesting topic, since few software packages are present on the market for the simulation of this effect.

Another possible topic of research could be the link between multipaction and corona discharge, and how pressure levels inside waveguide-based components affect the transition from multipaction (which happens under vacuum) and corona discharges (which happens only when gas molecules are present inside the device).

# Bibliography

---

- [1] D. M. Pozar, *Microwave Engineering*, 4th ed. Hoboken, NJ, USA: Wiley, 2011.
- [2] R. E. Collin, Foundations for Microwave Engineering. IEEE, 2001.
- [3] H. Padamsee, J. Knobloch, and T. Hays, *RF superconductivity for accelerators*, Nashville, TN, USA: John Wiley & Sons, 1998.
- [4] P. González, C. Alcaide, R. Cervera, M. Rodríguez, O. Monerris, J. Petit, A. Rodríguez, A. Vidal, J. Vague, J. V. Morro, P. Soto and V. E. Boria "Multipactor Threshold Estimation Techniques Based on Circuit Models, Electromagnetic Fields, and Particle Simulators," in IEEE Journal of Microwaves, vol. 2, no. 1, pp. 57-77, Jan. 2022, DOI: 10.1109/JMW.2021.3132284.
- [5] J. R. M. Vaughan, "Multipactor," in IEEE Transactions on Electron Devices, vol. 35, no. 7, pp. 1172-1180, July 1988, DOI: 10.1109/16.3387.
- [6] W. J. Gallagher, "The Multipactor Effect," in IEEE Transactions on Nuclear Science, vol. 26, no. 3, pp. 4280-4282, June 1979, DOI: 10.1109/TNS.1979.4330768.
- [7] S. A. Rice and J. P. Verboncoeur, "A Comparison of Multipactor Predictions Using Two Popular Secondary Electron Models," in IEEE Transactions on Plasma Science, vol. 42, no. 6, pp. 1484-1487, June 2014, DOI: 10.1109/TPS.2014.2321118.
- [8] H. C. Kim, J. P. Verboncoeur and Y. Y. Lau, "Invited Paper - Modeling RF Window Breakdown: from Vacuum Multipactor to RF Plasma," in IEEE Transactions on Dielectrics and Electrical Insulation, vol. 14, no. 4, pp. 774-782, Aug. 2007, DOI: 10.1109/TDEI.2007.4286505.
- [9] D. González-Iglesias, Á. Gómez, B. Gimeno, Ó. Fernández, A. Vegas, F. Casas, S. A. Hormigo, C. Vicente, J. Gil, R. Mata, I. Montero, V. E. Boria and D. Raboso, "Analysis of Multipactor RF Breakdown in a Waveguide Containing a Transversely Magnetized Ferrite," in IEEE Transactions on Electron Devices, vol. 63, no. 12, pp. 4939-4947, Dec. 2016, DOI: 10.1109/TED.2016.2614370.

- [10] S. R. Farrell and W. J. Gallagher, "Further Notes on the Multipactor Effect," in IEEE Transactions on Nuclear Science, vol. 32, no. 5, pp. 2900-2902, Oct. 1985, DOI: 10.1109/TNS.1985.4334220.
- [11] A. M. Pérez, C. Tienda, C. Vicente, S. Anza, J. Gil, B. Gimeno, V. E. Boria and David Raboso, "Prediction of Multipactor Breakdown Thresholds in Coaxial Transmission Lines for Traveling, Standing, and Mixed Waves," in IEEE Transactions on Plasma Science, vol. 37, no. 10, pp. 2031-2040, Oct. 2009, DOI: 10.1109/TPS.2009.2028428.
- [12] C. Bourat and J-M. Joly, "On multipactor effect in a 600 MHz RF cavity used in electron linear accelerator," in IEEE Transactions on Electrical Insulation, vol. 24, no. 6, pp. 1045-1048, Dec. 1989, DOI: 10.1109/14.46336.
- [13] R. Boni, V. Chimenti, P. Fernandes, R. Parodi, B. Spataro and F. Tazzioli, "Reduction of Multipacting in an Accelerator Cavity," in IEEE Transactions on Nuclear Science, vol. 32, no. 5, pp. 2815-2817, Oct. 1985, DOI: 10.1109/TNS.1985.4334191.
- [14] S. Michizono, "Secondary Electron Emission from Alumina RF Windows," 2006 International Symposium on Discharges and Electrical Insulation in Vacuum, Matsue, Japan, 2006, pp. 91-96, DOI: 10.1109/DEIV.2006.357239.
- [15] J. R. M. Vaughan, "A new formula for secondary emission yield," in IEEE Transactions on Electron Devices, vol. 36, no. 9, pp. 1963-1967, Sept. 1989, DOI: 10.1109/16.34278.
- [16] M. Furman and M. Pivi, "Probabilistic model for the simulation of secondary electron emission," Physical Review Special Topics – Accelerators and Beams, vol. 5, no. 124404, 2002, DOI: 10.1103/PhysRevSTAB.5.124404
- [17] J. de Lara, F. Pérez, M. Alfonseda, L. Galán, I. Montero, E. Román, and D. Raboso García-Baquero, "Multipactor prediction for on-board space-craft RF equipment with the MEST software tool," in IEEE Transactions on Plasma Science, vol. 34, no. 2, pp. 476-484, April 2006, DOI: 10.1109/TPS.2006.872450.
- [18] A. M. Pérez, V. E. Boria, B. Gimeno, S. Anza, C. Vicente, and J. Gil, "Multipactor analysis in circular waveguides," Journal of Electromagnetic Waves and Applications, vol. 23, no. 11–12, pp. 1575–1583, 2009, DOI: 10.1163/156939309789476356

- [19] G. Burt, R. G. Carter, A. C. Dexter, B. Hall, and J. D. A. Smith, "Benchmarking simulations of multipactor in rectangular waveguides using CST-Particle Studio," Cern.ch. [Online]. [Accessed: 27-Feb-2023]. Available: <https://accelconf.web.cern.ch/srf2009/papers/tuppo046.pdf>
- [20] G. Romanov, "Simulation of multipacting with space charge effect," American Journal of Physics and Applications, vol. 5, no. 6, p. 99, 2017, DOI: 10.11648/j.ajpa.20170506.15
- [21] Z. C. Shaw, L. Silvestre, T. Sugai, B. Esser, J. J. Mankowski, J. C. Dickens, and A. A. Neuber, "On the limits of multipactor in rectangular waveguides," Phys. Plasmas, vol. 27, no. 8, p. 083512, 2020.
- [22] E. G. T. Wulff and G. Iadarola, "Implementation and benchmarking of the Furman-Pivi model for Secondary Electron Emission in the PyECLOUD simulation code," Cern.ch. [Online]. Available: <https://cds.cern.ch/record/2683285/files/CERN-ACC-NOTE-2019-0029.pdf>. [Accessed: 01-Mar-2023].
- [23] P. T. Farnsworth, "Electron multiplier," 1969399, 07-Aug-1934.
- [24] P. T. Farnsworth, "Image dissector," 2087683, 20-Jul-1937.
- [25] S. Hanna, RF linear accelerators for medical and industrial applications. Norwood, MA: Artech House, 2012.
- [26] "Flexible only seamless waveguides," Advanced Microwave Components, Inc. [Online]. Available: <https://www.advancedmicrowave.com/standard-waveguide-components/flexible-only-seamless-waveguides>. [Accessed: 25-Mar-2023].
- [27] J. -H. Choi and Y. -H. Kim, "A High-Power Waveguide Phase Shifter With Periodic RF Chokes for Subgigawatt Nanopulse Transmission," in IEEE Transactions on Plasma Science, vol. 44, no. 10, pp. 2307-2313, Oct. 2016, DOI: 10.1109/TPS.2016.2600032.
- [28] Electronics notes, "RF / microwave circulator / isolator - Electronics Notes," Electronics-Notes.com [Online]. Available: <https://www.electronics-notes.com/articles/radio/rf-microwave-circulator-isolator/what-is-an-rf-circulator-isolator.php>. [Accessed: 25-Mar-2023].
- [29] K. Peach, P. Wilson, and B. Jones, "Accelerator science in medical physics," Br. J. Radiol., vol. 84 Spec No 1, pp. S4-10, 2011, DOI: 10.1259/bjr/16022594.
- [30] "E & H plane bends," Premwave.com. [Online]. Available: <https://www.premwave.com/microwave-components/e-h-plane-bends.php>. [Accessed: 25-Mar-2023].

- [31] "RF Windows - impedance matched & minimize reflection," Altair USA, 16-Sep-2019. [Online]. Available: <https://altairusa.com/rf-windows/>. [Accessed: 25-Mar-2023].
- [32] J. A. Ruiz-Cruz, J. R. Montejo-Garai, and J. M. Rebollar, "Short-slot E- and H-plane waveguide couplers with an arbitrary power division ratio," International Journal of Electronics, vol. 98, no. 1, pp. 11–24, 2011, DOI: 10.1080/00207217.2010.488913.
- [33] H. J. Riblet, "The Short-Slot Hybrid Junction," in Proceedings of the IRE, vol. 40, no. 2, pp. 180-184, Feb. 1952, DOI: 10.1109/JRPROC.1952.274021.
- [34] K. Kuroiwa, A. Gonzalez, M. Koyano, T. Kojima, Y. Fujii, Y. Uzawa and H. Ogawa, "Short-slot hybrid coupler using linear taper in W-band," J. Infrared Millim. Terahertz Waves, vol. 34, no. 12, pp. 815–823, 2013, DOI: 10.1007/s10762-013-0030-3.
- [35] S. B. Cohn and R. Levy, "History of Microwave Passive Components with Particular Attention to Directional Couplers," in IEEE Transactions on Microwave Theory and Techniques, vol. 32, no. 9, pp. 1046-1054, September 1984, DOI: 10.1109/TMTT.1984.1132816.
- [36] B. Hussain, "Short-Slot Hybrid Coupler in Gap Waveguides at 38 GHz," Institute for Systems and Computer Engineering, Technology and Science (INESC TEC), Porto (Portugal), 2011.
- [37] A. J. Hatch and H. B. Williams, "Multipacting modes of high-frequency gaseous breakdown," Phys. Rev., vol. 112, no. 3, pp. 681–685, 1958, DOI: 10.1103/PhysRev.112.681.
- [38] "ECSS multipactor tool," Esa.int. [Online]. Available: <http://multipactor.esa.int/>. [Accessed: 25-Mar-2023].
- [39] "ECSS multipactor tool," Val Space Consortium el Consorcio Espacial Valenciano, 09-Aug-2018. [Online]. Available: <https://www.val-space.com/en/ecss-multipactor-tool/>. [Accessed: 25-Mar-2023].
- [40] "Multipactor Tool version 2.0.0," ESA ESSR. [Online]. Available: <https://essr.esa.int/project/multipactor-tool-version-2-0-0>. [Accessed: 25-Mar-2023].
- [41] CST Online Help 2020
- [42] B. Jeanty-Ruard and J. Forest, ECSS Multipactor Tool V 2.0.0 - User Manual, Version 1, Rev. 5. European Space Agency, 2021.
- [43] P.-Y. Lee, D.-K. Baek, J.-H. (martin) Park, and E.-S. Choi, "Design of 3dB Directional Coupler for Ka-Band Input Multiplexer of Satellite Payload

Applications,” in 2018 International Symposium on Antennas and Propagation, 2019.



# Acknowledgments

---

First and foremost, I wish to express my gratitude to my primary supervisor, Prof. Francesco Prudenzano, along with his collaborators Francesco Anelli and Maria Antonella Loconsole for the support, guidance and feedback provided during the writing of this thesis. I hope the efforts you put in following me throughout this work, developed in a very short time and with a strict schedule, has been somehow repaid.

I would like to thank my external supervisor Giovanni Rutigliani, and all the people I've met at LinearBeam, first of all for the opportunity they gave me to work in a stimulating, professional but at the same time friendly environment, but also especially Giovanni for the support, encouragement and insights provided during the experimental phase of this work.

Besides from the people I have worked with for this thesis, I would like to expressly thank two professors from the faculty staff at my university: Prof. Luciano Mescia, for his course on microwave foundations, without which this thesis would not have been possible, and Prof. Cristoforo Marzocca, for his support, guidance and availability every time I had doubts or concerns during the last years of this journey.

Moving on to my personal life, I would like to express my gratitude to my parents, Tonia and Giuseppe, who allowed me to embark in this long journey even if at the beginning the odds weren't exactly at my favor. Thanks for the support, which has also been present in those last days for the final preparations, and for being persistent throughout all these years.

A person I particularly need to thank is my life long friend Massimiliano, with whom I started this adventure. What started as a way to trick time, by studying calculus at "Prima Fila" after I abandoned university books for a long time, has gradually become something more tangible and real, leading up to this day.

I hope you will reach this very same goal, or whatever it is that can bring you happiness (and money).

I wish to thank my grandma, for all the times that she let me and Massimiliano study at her house, spoiling us with chocolate, hand-made biscuits, pomegranate juice and lot of other things I don't remember.

I'd like to thank my friends Andrea and Eleonora, for being a constant throughout these years; I look forward for the next event of yours!

A mention goes to Marcello, Aldo, Filippo and others, for being always out there when you wanted to take a coffee, a beer, or just go outside to take a walk and a bit of fresh air.

I wish to thank also my brother, for... being my brother; Giusy; my aunts Tina and Ernesta for sparking and fueling my interest into science; my aunt Marialuisa for all the times that she asked "when are you going to graduate?"; my uncles Franco and Mariella for the period I passed at their house in Lariano a long time ago, which let me cleared my mind and provided me some insights on what I wanted and didn't wanted to do in life; and all the other relatives and friends present today or that in some way shared with me parts of this path (I don't think there's enough time to list you all, so consider yourself included in this point).

But most of all, thanks to me for having persisted, endured and believed in this despite all the obstacles, difficulties and roadblocks that I've encountered during this journey.

Bari, April 2023

Francesco Caterina

# Ringraziamenti

---

Prima di tutto, vorrei esprimere la mia gratitudine al mio relatore, Prof. Francesco Prudenzano, assieme ai suoi collaboratori Francesco Anelli ed Antonella Maria Loconsole per il supporto, la guida e i numerosi feedback forniti durante la stesura di questa tesi. Spero che gli sforzi che avete impiegato nel seguirmi in questo lavoro, sviluppato in breve tempo e con tempistiche molto strette, sia stato in qualche modo ripagato.

Vorrei ringraziare il mio relatore esterno Giovanni Rutigliani, e tutte le persone che ho conosciuto a LinearBeam, innanzitutto per l'opportunità che mi hanno dato di lavorare in un ambiente stimolante, professionale ma amichevole allo stesso tempo, ma anche specialmente Giovanni per il supporto, l'incoraggiamento e le idee fornite durante la fase sperimentale di questo lavoro.

A parte le persone con cui ho lavorato per questa tesi, vorrei ringraziare esplicitamente due professori del corpo docenti dell'università: il Prof. Luciano Mescia per il suo corso in Microonde, senza il quale questa tesi non sarebbe stata possibile, ed il Prof. Cristoforo Marzocca per il suo supporto, guida e disponibilità ogni volta che avevo dubbi o preoccupazioni durante gli ultimi anni di questo percorso.

Passando alla mia vita personale, vorrei ringraziare i miei genitori, Giuseppe e Tonia, che mi hanno permesso di imbarcarmi in questo percorso anche se all'inizio le probabilità non erano esattamente a mio favore. Grazie per l'aiuto ed il supporto che sono stati presenti anche in questi ultimi giorni per i preparativi finali, e grazie per esser stati in generale persistenti durante tutti questi anni.

Una persona che ci tengo particolarmente a ringraziare è il mio amico di una vita, Massimiliano, con cui ho iniziato quest'avventura. Quel che è iniziato come un modo per ingannare il tempo, studiando analisi al "Prima Fila" dopo che avevo abbandonato i libri di università dopo tanto tempo è diventato via via qualcosa di tangibile, reale, sino ad arrivare a questo giorno.

Spero che tu raggiungerai lo stesso obiettivo, o qualsiasi cosa sia che possa portarti felicità (e soldi).

Ci tengo a ringraziare anche mia nonna, per tutte le volte che ha lasciato studiare me e Massimiliano a casa sua, viziandoci con cioccolata, biscotti fatti in casa, succo di melograno e un sacco di altre cose che adesso non ricordo.

Voglio ringraziare anche i miei amici Andrea ed Eleonora, per esser stati una costante durante tutti questi anni; attendo con ansia il prossimo evento che vi riguarda!

Un grazie va anche a Marcello, Aldo, Filippo e gli altri per esserci sempre stati quando volevi prendere un caffè, una birra, o semplicemente andare fuori a fare una camminata per prendere un po' d'aria fresca.

Ringrazio anche mio fratello per...esser mio fratello; Giusy, le mie zie Tina ed Ernesta per aver acceso ed alimentato il mio interesse per la scienza; mia zia Marialuisa per tutte le volte che chiedeva “e quando ti laurei?”; i miei zii Franco e Mariella per il periodo in cui mi hanno ospitato a casa loro a Lariano un bel po' di tempo fa, che mi ha permesso di schiarirmi la mente e mi ha fornito alcuni spunti su ciò che volevo e non volevo fare nella vita; e ringrazio tutti gli altri parenti ed amici presenti qui oggi o che in qualche modo hanno condiviso con me parte di questo cammino (non penso ci sia tempo per elencarvi tutti, quindi consideratevi in qualche modo inclusi in questa parte).

Ma soprattutto ringrazio me stesso, per aver persistito, resistito e creduto in tutto questo nonostante gli ostacoli, le difficoltà e gli incidenti di percorso che ho incontrato durante questo viaggio.

Bari, April 2023

Francesco Caterina